INFORMATION TO USERS

This manuscript has been reproduced from the microfilm master. UMI films the text directly from the original or copy submitted. Thus, some thesis and dissertation copies are in typewriter face, while others may be from any type of computer printer.

The quality of this reproduction is dependent upon the quality of the copy submitted. Broken or indistinct print, colored or poor quality illustrations and photographs, print bleedthrough, substandard margins, and improper alignment can adversely affect reproduction.

In the unlikely event that the author did not send UMI a complete manuscript and there are missing pages, these will be noted. Also, if unauthorized copyright material had to be removed, a note will indicate the deletion.

Oversize materials (e.g., maps, drawings, charts) are reproduced by sectioning the original, beginning at the upper left-hand corner and continuing from left to right in equal sections with small overlaps. Each original is also photographed in one exposure and is included in reduced form at the back of the book.

Photographs included in the original manuscript have been reproduced xerographically in this copy. Higher quality 6" x 9" black and white photographic prints are available for any photographs or illustrations appearing in this copy for an additional charge. Contact UMI directly to order.

UMI

A Bell & Howell Information Company
300 North Zeeb Road, Ann Arbor MI 48106-1346 USA
313/761-4700 800/521-0600

Mathematical modeling studies of electrochemical growth of oxide films on metals

by

Mei-Hui Wang

A dissertation submitted to the graduate faculty
in partial fulfillment of the requirements for the degree of
DOCTOR OF PHILOSOPHY

Major: Chemical Engineering

Major Professor: Kurt R. Hebert

Iowa State University

Ames, Iowa

1998

Graduate College
Iowa State University

This is to certify that the Doctoral dissertation of

Mei-Hui Wang

has met the dissertation requirements of Iowa State University

Signature was redacted for privacy.

Major Professor

Signature was redacted for privacy.

For the Major Program

Signature was redacted for privacy.

For the Graduate College

TABLE OF CONTENTS

LIST OF TABLES

LIST OF FIGURES

1 GENERAL INTRODUCTION

1.1 Introduction

Air-formed oxide films are always present on passive metals, such as aluminum, iron, tantalum, zirconium, etc. An air-formed oxide film protects metal from further oxidation in the air as it separates the oxidation reactants, metal and oxygen. The continued growth of oxide films can be produced by anodic oxidation in proper electrolyte. During anodic oxidation, an electrostatic field is set up in the oxide causing the migration of metal and/or oxygen ions through the film, so metal and oxygen can react to form new oxide. In this chapter, the electrochemical growth of oxide films on metals is first introduced according to the growth kinetics model developed by Kirchheim [1].

1.2 Growth Kinetics of Passive Films

Over the last five decades, several models for passive film growth have been proposed to explain experimental results of film growth, such as the logarithmic time law for the thickness of the film growing under potentiostatic condition,

$$\xi = C + D\ln t, \tag{1.1}$$

where ξ is the film thickness and C and D are constants. However, many early models are not completely satisfactory from a physical point of view, nor are they in complete agreement with experimental data. In 1987, Kirchheim [1] extended the earlier work of Vetter and Gorn [2] to develop a new model of growth of passive films and only this new model is in overall agreement with experimental findings for different pH values. Hence, Kirchheim's model will

be the focus of this section. A sketch of the film growth model is first presented in Figure 1.1 to assist the introduction of the model as follows.

The passive film is a pore-free oxide film, in which the ions migrate due to high electric fields of a few $MVcm^{-1}$. The transport of ions in ionic crystals can occur by the jumping of ions into adjacent lattice vacancies [3]. The transport of ions in one direction may be considered as the transport of vacancies in the opposite direction.

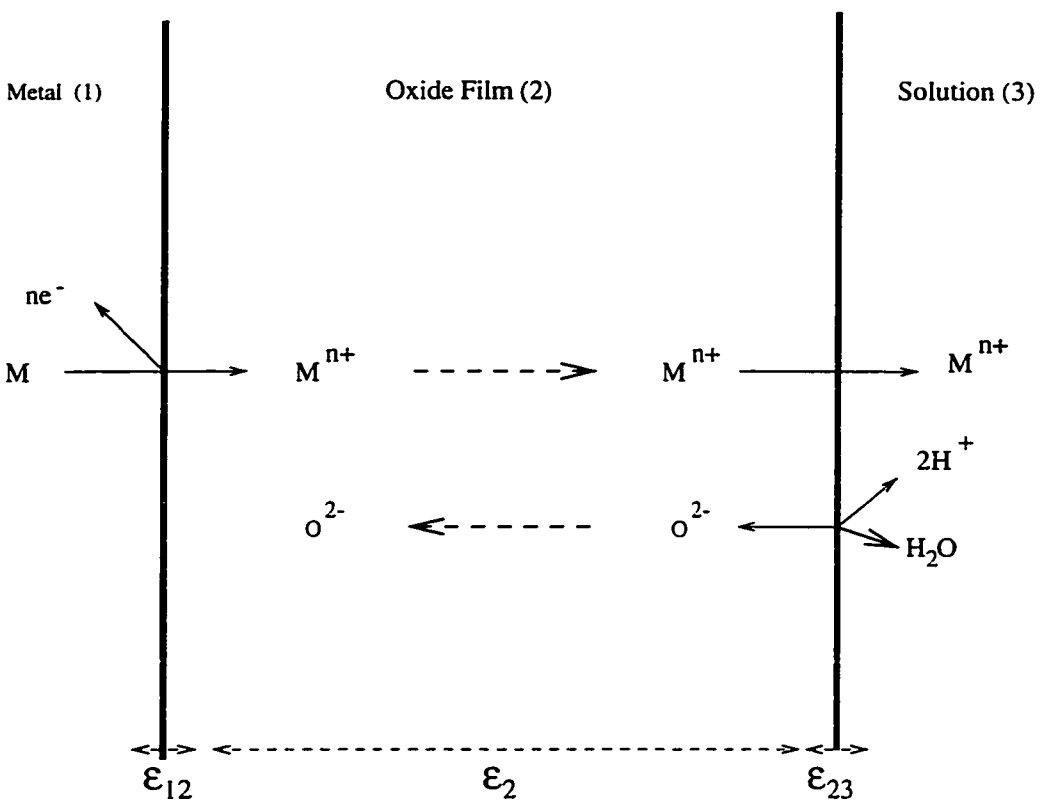

Figure 1.1 Sketch of the film growth model.

The probability of an ion jump will vary proportionally with the density of the vacancies and exponentially with the change in the Gibbs free energy of activation, ΔF (energy to overcome the potential barrier). In the presence of an electric field, E, the energy barrier for the ion to make a jump along the same direction as the field becomes $\Delta F - \frac{\alpha q E s}{kT}$. s is the jump distance, and α, a parameter between 0 and 1, describes the location of the peak of the adjacent activation hump within the jump distance. q is the charge of the ion. On the other

hand, the ion needs to overcome $\Delta F + \frac{(1-\alpha)qEs}{kT}$ barrier energy in order to jump against the field. On the basis of this theory, the relationship between current and field is given by

$$i = i_o[\exp(\frac{\alpha B\varepsilon}{\xi}) - \exp(\frac{-(1-\alpha)B\varepsilon}{\xi})], \tag{1.2}$$

where

$$B = \frac{zFs}{RT}. \tag{1.3}$$

ε is the potential drop across the film. i_o is proportional to the mobility of ions in the absence of an electric field. When the electric field is sufficiently large, one of the exponential terms in Equation 1.2 can be neglected. This type of electrical conduction is normally called high-field conduction.

According to Vetter and Gorn [2], the reactions taking place at the oxide-electrolyte interface are,

$$H_2O(aq) \rightleftharpoons O^{2-}(ox) + 2H^+(aq), \tag{1.4}$$

and

$$M^{n+}(ox) \rightarrow M^{n+}(aq). \tag{1.5}$$

They represent the film formation/dissolution reaction and the corrosion reaction respectively. The rate determining steps of Reactions 1.4 and 1.5 are the transfers of ions through the oxide-electrolyte interface. Let the potential drop across the interface be ε_{23} and the equilibrium potential of Reaction 1.4 be ε°_{23}. Then the current densities, accounting for Reactions 1.4 and 1.5, are determined by the overpotential at the oxide-electrolyte interface as

$$i_l = i_{lo}[\exp(\frac{\alpha_l^+ F}{RT}\eta_O^{23}) - \exp(-\frac{\alpha_l^- F}{RT}\eta_O^{23})], \tag{1.6}$$

and

$$i_c = i_{co}\exp(\frac{\alpha_c F}{RT}\eta_O^{23}), \tag{1.7}$$

where

$$\eta_O^{23} = \varepsilon_{23} - \varepsilon^\circ_{23}. \tag{1.8}$$

α_c, α_l^+ and α_l^- are charge transfer coefficients. In case of solutions with few metal ions, the reverse of Reaction 1.5 is neglected so that Equation 1.7 contains only one exponential term.

i_l corresponds to film formation ($i_l > 0$) or dissolution ($i_l < 0$). The total current density is given by the summation of i_l and i_c;

$$i = i_c + i_l. \tag{1.9}$$

On the other hand, at the metal-film interface, the oxidation of the metal takes place and the metal ion enters the film. Figure 1.1 gives a sketch of this model.

As shown by the dashed arrows in Figure 1.1, ion conduction in the passive film could be carried out by either the migration of O^{-2} or that of M^{+n}. The oxide film could therefore grow at either the metal-film interface or the film-solution interface. ε_2 represents the potential drop across the passive film.

In case of small current densities, the potential drop across the metal-oxide interface, ε_{12}, is assumed to be independent of i. The potential drop from the metal to the electrolyte adjacent to the passive film can then be written as:

$$\begin{aligned} \varepsilon &= \varepsilon_{12} + \varepsilon_2 + \varepsilon_{23}^{\circ} + \eta_O^{23} \\ &= \text{const.} + \varepsilon_2 + \eta_O^{23}. \end{aligned} \tag{1.10}$$

Under galvanostatic conditions, the electric field in the passive film, ε_2/ξ, and η_O^{23} are constants and the film grows at a constant rate. Under potentiostatic condition, the summation $(\varepsilon_2 + \eta_O^{23})$ is kept constant and $\eta_O^{23} \rightarrow 0$ as the stationary state is approached. Kirchheim's model is able to explain Equation 1.1 under potentiostatic condition, the linear increase of the potential vs. time under galvanostatic control, and several other experimental findings.

1.3 Dissertation Organization

Two mathematical modeling studies regarding electrochemical growth of oxide films on metals are presented separately in Part I and II of this dissertation. In Part I, film growth on the cathodically charged aluminum electrode was studied by simulating potentiostatic current decays due to film growth with an electrical model. The purpose of this study is to investigate the structural changes of the oxide film caused by cathodic charging. In Part II, the ionic conduction in amorphous anodic oxide films is of interest. Models for ionic conduction

based on independent hopping of point defects fail to give comparable fluxes of both metal and oxygen ions during the growth of amorphous anodic oxide films. This is contrary to experimental results. Hence, a new defect cluster model was developed to quantitatively predict the simultaneous migration of metal and oxygen ions in an amorphous oxide.

Since the work in Part I and that in Part II were motivated by different reasons, each work needs its own literature review to support the pertinent background information. Readers can follow the content in one part without consulting the content in the other part or *vice versa*.

PART I

AN ELECTRICAL MODEL FOR THE CATHODICALLY CHARGED ALUMINUM ELECTRODE

2 PASSIVITY AND PIT INITIATION OF ALUMINUM IN AQUEOUS ELECTROLYTES

2.1 Introduction

Aluminum carries an air-formed surface oxide film of some 3-5 nm due to low temperature oxidation by oxygen from the air [4]. After immersion in various aqueous electrolytes, the composition, structure, and thickness of the oxide film may change. Anodic oxidation of aluminum in proper electrolytes can produce an essentially nonporous barrier-type oxide layer, which protects the metal against corrosion. The surface oxide layer serves as a mass transfer barrier to corrosion reactions. Hence, the metal is said to be passivated against corrosion by a protective oxide film.

Pitting is a type of local dissolution resulting in cavities on metal surface. Pitting corrosion of passive metals or alloys is related to the presence of certain aggressive ions in the medium, such as chloride ions. Except the pitting area, the other parts of the metal surface are still covered by oxide layers and remain passive. The dissolution rate in the pit area can be as much as 10^6 times higher than that on the passive metal [5].

Electrochemical depassivation is the most common type of pitting, which takes place under potentiostatic or galvanostatic polarization in solutions containing aggressive ions. This type of pitting is often characterized by a potential called the pitting potential, below which the metal remains passive and above which pitting takes place. As described below, the pitting potential is a function of the composition of the electrolyte, the temperature, and the composition of the alloy, etc.

Recently, the applications of anodic alumina in electronics are rapidly growing due to their excellent electronic properties and good reproducibility in production [6]. Aluminum foil

capacitors represent one of the important applications because of their compactness and low cost. A large capacitance of aluminum foil capacitors is offered by extremely thin oxide layers on electrodes and high surface areas of electrodes. The high surface areas of electrodes have been commercially achieved by electrochemical tunnel etching of aluminum foils.

Alternating voltage techniques have been applied in the manufacture of aluminum foil capacitors [7]. AC etching technology has been found to produce a large population of pits on aluminum [8]. The sizes of etch pits decrease as the AC frequency and the pit density increases as the AC frequency [9]. In order to investigate the pit initiation mechanism, Lin and Hebert [10] use one cycle of cathodic-anodic polarization to study pit initiation, and concluded that prior cathodic polarization can increase pit densities on aluminum during the initial 10 ms of anodic polarization by a factor of 100. The electrical conduction properties of the surface film on aluminum during cathodic polarization were also studied in order to furnish information on the process of pit initiation [11]. In addition to pit initiation, pit growth is a research focus as well. Alwitt *et al.* [12] found etch tunnels and pits by etching aluminum in 60°C chloride solution with a constant anodic current. Since the tunnel etching of aluminum foil has been used primarily in the production of aluminum foil capacitors, the parameters related to tunnel growth, such temperature, current density and etchant composition, have been therefore of interest [12] [13].

This work was initiated to investigate the effect of prior cathodic charging on the oxide film on aluminum and hoped to link any possible change in the oxide film to pitting susceptibility. The review presented in the chapter offers the background information, in addition to the film growth kinetics described in Chapter 1, for the development of an electrical model for the cathodically charged aluminum electrode.

2.2 Oxide Films on Aluminum

Oxidation conditions determine the physical structure and properties of oxide films formed on aluminum. For instance, an air-formed oxide film is largely amorphous $\gamma - Al_2O_3$. Oxide films formed by prolonged thermal oxidation can be as thick as 0.2 μm. Below 500 °C, $\eta - Al_2O_3$

forms [14].

Oxide films on aluminum may be thickened by anodic polarization in various electrolytes. If the electrolyte dissolves the oxide only slightly, as do borate or boric acid solutions, tartrate or carbonate solutions, etc., the oxide layer formed is dense dielectric barrier type [15]. Its thickness, up to about 1 μm, is terminated by dielectric breakdown, often associated with visible sparking. On the other hand, if the anodic film is formed in an electrolyte such as sulphuric or oxalic acid solutions, which chemically dissolves aluminum oxide, the film has a double-layer structure. The inner layer, which is initially formed, is dense, amorphous, and approximately 1 to 10 nm thick. The outer layer, produced by later oxidation, is uniformly porous, and will grow at almost constant voltage to a thickness of many microns. The pores of the outer layer are parallel to each other and their geometrical parameters are dependent on the anodization variables, such as electrolyte compositions, the current or potential of anodization, etc. [16].

Lin and Hebert studied the changes of the oxide film on aluminum during cathodic polarization by using *in situ* quartz crystal microbalance (QCM) and *ex situ* infrared reflectance spectroscopy(IRS) [17]. After passage of 7.2 mC/cm^2 of cathodic charge at a potential of -2.0 V ($vs.Ag/AgCl/4MKCl$), the film transformed from oxide into hydroxide or oxyhydroxide and started to grow at an approximately constant rate with time. They suggested that the hydration of native oxide film results in a significant loss of the resistance to ion transport so that film growth initiates. Based on the deuterium exchange experiments by Lin [18], the films produced by cathodic charging are likely porous.

Generally speaking, study of growth of anodic oxide films has been motivated by their industrial applications, e.g. electrolytic capacitors and electrically insulating finishes [16]. Again, the growth kinetics of oxide films have been discussed in Chapter 1. The research on oxide films produced by cathodic charging was motivated because of the application of AC technology in the production of aluminum foil capacitors.

2.3 Pit Initiation Mechanisms

Many theories of pitting have been proposed on the basis of various experimental results. There exist similarities between some of them since some later theories consist of the ideas form earlier theories. Hence, a strict differentiation of each theory on pitting initiation is not easy. On the other hand, some theories are conflicting. Such confusion occurs perhaps because mechanisms proposed to explain certain experimental observations often intend to explain all types of pitting under various experimental situations. The main mechanisms proposed for pitting on passive metals have been reviewed by a few authors, such as Strehblow [19], Szklarska-Smialowska [15], Böhni [20] and Galvele [5].

2.3.1 Adsorption Mechanism

Hoar and Jacob [21] postulated that the adsorption of halide anions at the surface of the oxide layer leads to a surface complex of a lattice cation and adsorbed halide ions, due to the high complex energy. The surface complex was assumed readily separable from the lattice, so the transfer of the metal ions into the electrolyte is enhanced. As a consequence, the oxide layer could be thinner due to its dissolution. Pits were thought to nucleate at defects in the oxide layer where dissolution is more aggressive. This model could explain the fact that the induction time for pit initiation increases with film thickness. The pitting potential could be the potential sufficiently negative to prevent the adsorption of aggressive anions. The inhibiting action of various anions may be rationalized by the concept of competitive adsorption. However, some experimental observations cannot be understood based on this mechanism [22]. For instance, nitrate ions adsorbed preferentially inhibit pitting of aluminum in solutions containing chloride ions, but produce by themselves pitting of aluminum at a different potentials.

2.3.2 Penetration Mechanism

Under the influence of an electrostatic field, the migration of anions through the passive layer is possible. Hence, Hoar, *et al.* [23] postulated that penetrating anions "contaminate" the oxide film into a much better ionic conductor where higher currents start to circulate and

pitting could start. In their theory, the pitting potential was explained as the potential above which anion entry into the passivating oxide film is field-stimulated. The induction time of pit initiation is determined by the migration time of aggressive ions through the passive film to the metal-film interface.

Some authors have found the incorporation of chloride into the passive film by surface analytical methods, but some could not find aggressive ions in the passive film [19]. Also, films grown in aggressive ions *below* the pitting potential are recently found contaminated [24]. Nevertheless, the penetration of a passivation barrier by polyatomic aggressive anions, such as NO_3^- and ClO_4^-, is not considered to be conceivable [5].

2.3.3 Film Flaws and Film Breaking Mechanisms

Wood *et al.* [25] suggested that pitting starts at flaws in the oxide film. These authors experimentally proved that internal flaws do exist in passive films on aluminum. Just after the immersion of the metal in the aggressive solution, pits immediately propagate at flaws of the otherwise inert oxide film. Maier and Galvele [5] observed the slip band structure on aluminum strained in 1.0 M $NaCl$ solution or in 1.0 M $NaNO_3$ solution. If the straining process occurs below the pitting potential, no evidence of corrosion could be found on the slip steps. Above the pitting potential, on the other hand, pitting could be easily found. This indicates that mechanical breakdown of the passive film is insufficient for pit initiation. On the other hand, Okamoto *et al.* [26] postulated that in the passive film there is a dynamic balance between film rupture and self repair based on noise analysis of passive metal at constant potential.

Film breaking mechanisms involve mechanical breakdown of small parts of the passive film exposing the bare metal directly to aggressive ions. The adsorbed aggressive ions on the metal surface prevent repassivation so that metal dissolution is accelerated. Sato [27] suggested that a significant change of electrostriction pressure in anodic films, caused by the adsorption of aggressive ions, leads to the mechanical breakdown. He showed that the film pressure due to electrostriction can be calculated from the following equation:

$$P - P_o = \frac{\epsilon(\epsilon - 1)E^2}{8\pi} - \frac{\gamma}{L}, \tag{2.1}$$

where P is the electrostriction pressure in the film, P_o is the atmospheric pressure, ϵ is the dielectric constant of the film, E is the electric field, γ is the surface tension of the film, and L is the film thickness. According to this equation, film pressure can be generated by an electric field and depends on both the surface tension of the film and the film thickness. When P exceeds a critical value, the film breaks down. The surface tension helps to stabilize the oxide layer and this effect decreases with increasing film thickness. Therefore, mechanical deformation or breakdown of the oxide film could occur if the film thickness is above a critical value. Sato proposed that adsorption of chloride ions greatly reduces the surface tension of the oxide film. A simplified equation was derived to relate the pitting potential to the surface concentration of chloride ions on the oxide film. Although this theory seems to qualitatively agree with the experimental results, its proof is rather difficult.

2.3.4 Ion Migration and Vacancy Condensation Mechanisms

According to the assumptions of Chao *et al.* [28] the diffusion of anion vacancies (or anions) in the film results in oxide growth. On the other hand, the diffusion of cation vacancies (or cations) results in metal dissolution only. As a consequence of metal dissolution, metal vacancies start to be generated at the metal-film interface and tend to submerge into the bulk metal. If the submergence occurs at a low rate, the metal vacancies may accumulate, forming voids. When the voids grows to a certain critical size, the passive film suffers local collapse.

Based their point defect model, which regards a passive film as a crystalline material containing numerous point defects, the diffusion rate of ion or vacancy is proportional to the concentration of vacancy. Apparently anion vacancies could be occupied by halide anions from solutions. Further assuming local equilibrium of the Schottky-pair reaction, a decrease of anion vacancies, caused by the incorporation of halide ions into the film, leads to a concomitant increase of cation vacancies. Lin *et al.* [29] therefore derived a mathematical expression for the pitting potential in terms of chloride concentration, which can be simplified as:

$$\varepsilon_p = A - B\log c_{Cl^-}. \tag{2.2}$$

A and B are constants. This equation corresponds to the commonly observed relationship

between critical pitting potential and chloride concentration in pitting experiments. Unfortunately, some parameters in the model are unknown so verification of this mechanism is not yet possible. Besides, since local film collapse leads to pitting, it must be assumed that point defects are nonuniformly distributed through the passive film. This model may not be applicable to those cases in which the anions in solution form strong soluble cation complexes, rather than incorporating into the outer layer of the film.

The condensation of vacancies has been suggested for the formation of surface pits. Wiersma and Hebert [30] proposed vacancy condensation for pit formation on aluminum by studying the early stages of pit growth. For foils pretreated by immersion in 1 N HCl at 25°C for 5 min, the pit volumes at early times are much larger than the equivalent volumes calculated from faradaic charges of metal dissolution. To account for this phenomena, they suggested that the pretreatment incorporates water in the passive film and the currentless oxidation reaction between aluminum and water takes place uniformly at metal-film interface.

$$Al + 2H_2O \rightarrow AlOOH + \frac{3}{2}H_2. \tag{2.3}$$

Since $AlOOH$ is a solid film material, aluminum atoms in the metal are oxidized into the film and leave behind vacancies in the metal. The vacancies could diffuse through the metal to growing pits. Therefore, the early currentless pit growth may be due to the condensation of the vacancies produced by Reaction 2.3.

2.4 Effects of Cathodic Polarization on Pit Initiation

The effects of prior cathodic charging on pit initiation on aluminum has been investigated by Lin and Hebert [10] [18]. In addition, the transformation of the surface oxide film due to cathodic charging was studied by using *ex situ* IRS [11]. The film mass change during cathodic charging was measured using *in situ* QCM [11] [17].

The rate of pit initiation and growth was enhanced by prior cathodic charging at a potential of -2.0 V vs. $Ag/AgCl/4M\ KCl$ reference electrode. This conclusion was obtained by using a scanning electron microscope (SEM) to determine pit size distribution and pit number and by

using an atomic force microscope (AFM) to measure pit depth and width. The pitting current transients at -0.4 V after a prior cathodic charge $Q_c > 0.13\ mC/cm^2$ consists of three parts in about 100 ms: an initial rapid decay, then a gradual increase, and finally a steady state. For cathodic charge less than 0.13 mC/cm^2, the pitting current did not rise within 100 ms. Since pit volumes during the period of pitting current transient were also determined, it has been found that the rising current was accompanied by increasing metal dissolution.

According to the QCM results, no mass change was observed during initial 2 sec of cathodic charging at -0.2 V. After passage of 7.2 mC/cm^2 of cathodic charge, the surface film on aluminum started to grow at a constant rate. Based on the IRS results, it has been suggested that the air-formed oxide film contained an appreciable amount of hydroxide or water. The critical cathodic charge at which the IRS spectra of surface oxide/hydroxide films started to change was between 4.7 and 10.7 mC/cm^2, consistent with the critical charge, 7.2 mC/cm^2, for surface film to grow. The film produced during cathodic charging was an aluminum oxyhydroxide or hydroxide containing absorbed water. According to QCM stripping measurements, the water content was suggested to be one H_2O molecule per aluminum ion. Film growth indicates that aluminum oxidation took place during the cathodic period, even though the potential, -2.0 V, was below the open circuit potential, -1.0 V.

In order to study further the possible connection between the aluminum oxidation before pitting and the pitting current transient, a set of "interruption" experiments were performed by Lin. Namely, after the cathodic charging, the potential was held at -0.9 V for a period of time before being stepped to -0.4 V. -0.9 V is between the open circuit potential (-1.0 V) and the pitting potential (-0.75 V), so the currents in the interruption periods were anodic and decayed with time. By using QCM, mass increase was observed during initial 3 sec of the interruption period. When the interruption time was more than 20 ms, the time needed for the pitting current at -0.4 V to reach a steady state started to increase. In other words, the cathodic acceleration of metal dissolution was significantly attenuated by the interruption at -0.9 V.

In a word, the growth or transformation of the surface film may have resulted in the

change of the pitting current transient. Specifically, the electrical resistance of the surface film is very likely one of the key factors determining the rate of pit initiation. Three possible mechanisms relating the electrical resistance of the surface film to the pitting induction time are as follows: First, if the adsorption of chloride ion on the metal-film interface results in depassivation of aluminum, the migration of chloride ions through the film could be slowed down by the electrically resistive film. Secondly, pitting could be initiated by film collapse caused by vacancy condensation at the metal-film interface. The electrical resistance of the surface film determined the rate of metal dissolution, which is proportional to the vacancy generation rate. Third, the presence of flaws serving as pit sites would also enhance the film's electrical conductance. In order to determine the electrical resistance of the surface film after the cathodic charging and after the interruption, anodic current decays at the potentials of -0.9 V and -0.4 V were modeled later in this work. The understanding of the electrical properties of the surface film on aluminum may contribute to the development of the pitting mechanism for aluminum in the future.

3 EXPERIMENTS AND EXPERIMENTAL RESULTS

3.1 Introduction

The experimental methods described in this section have been designed for the investigation of the pitting mechanism of cathodically charged aluminum. As described in Chapter 2, the pitting behavior at -0.4 V ($vs.Ag/AgCl/4MKCl$) depended on the quantity of the *prior* cathodic charge at -2.0 V. The interruption time at -0.9 V after cathodic charging was also influential to the pitting behavior at -0.4 V. The effects of prior cathodic charging at -2.0 V and the interruption time at -0.9 V on the surface oxide film of aluminum may have resulted in a change of pitting behavior. Hence, in order to understand the likely changes of surface oxide film caused by the two processes, the anodic current decays at -0.9 V after cathodic charging and those at -0.4 V after the interruption are to be modeled later in this work. The experiments performed here were used to obtain more useful information for the modeling work, in addition to the information which has been given by Lin and Hebert [11] [17] [18].

3.2 Experiments

3.2.1 Preparation of Aluminum Films

The aluminum films were deposited on both sides of quartz crystal disks by sputtering, which was performed by Christopher Jahnes at IBM T. J. Watson Research Center. The films were 0.2 μm thick and have a "keyhole" pattern, as shown in Figure 3.1. The 1 *in* diam. quartz crystals, manufactured by Valpey-Fisher, are either AT-cut or BT-cut, and both their sides are planar and overtone-polished.

The purpose of using quartz crystals was to measure the mass change of the aluminum film

during electrochemical experiments through the electrochemical quartz crystal microbalance system [11]. Unfortunately, the quartz crystals deposited by aluminum films could not resonate in the QCM system at a stable frequency, possibly due to the stress effects arising from the materials on the surface of the quartz resonator. Therefore, the aluminum films deposited by IBM could be used only for regular electrochemical experiments, in which no measurement of film mass change was performed.

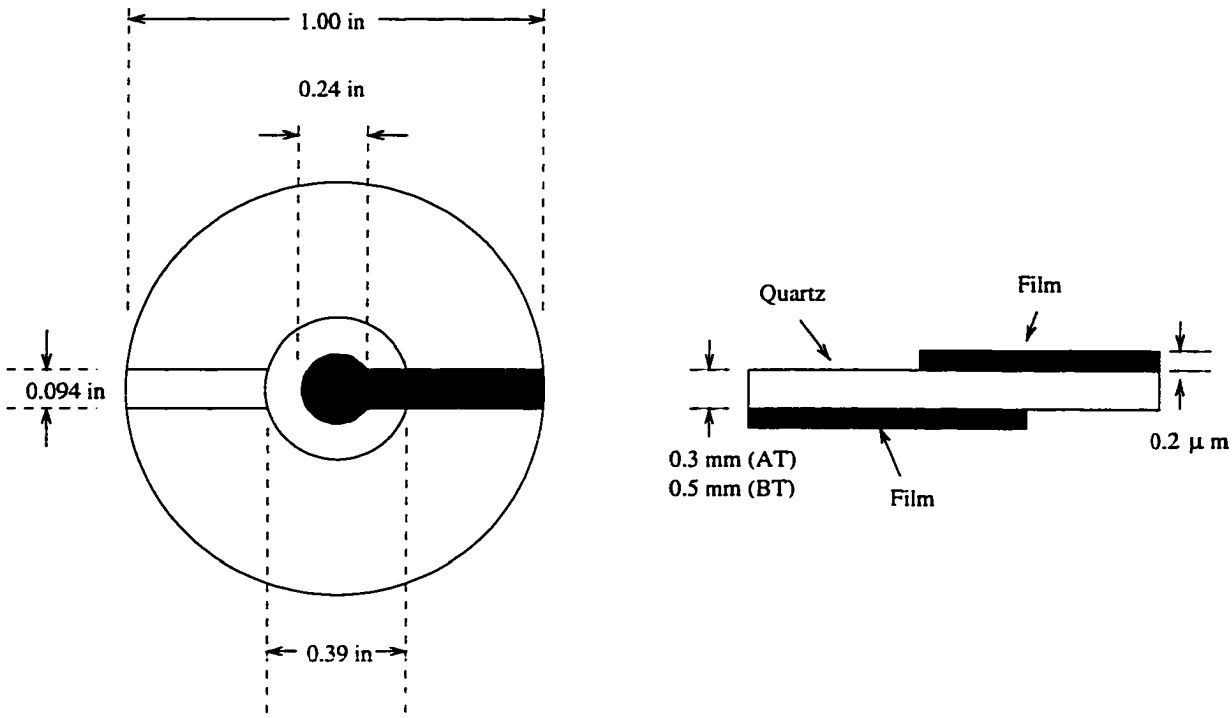

Figure 3.1 Quartz crystal resonator with aluminum films in a keyhole pattern.

3.2.2 Experimental Apparatus

The design and dimensions of the electrochemical cell are shown in Figure 3.2. The cell is made of a 100 *ml* beaker and a 1 *cm* i.d. glass tube. A quartz crystal is mounted at the bottom of the cell by using an O-ring joint, two O-rings and a clamp. The working electrode is the

aluminum film on the upper surface of the mounted quartz crystal. The counterelectrode is a platinum wire, which is positioned as far from the upper mouth of the glass tube as possible [31]. The reference electrode ($Ag/AgCl/4MKCl$) was placed at a fixed position between the upper mouth of the glass tube and the counterelectrode. To ensure a more reproducible ohmic resistance in the electrolyte for each experiment, the distance between the mouth of the glass tube and the reference electrode was at least 3 cm, as was the distance between the reference electrode and the counterelectrode.

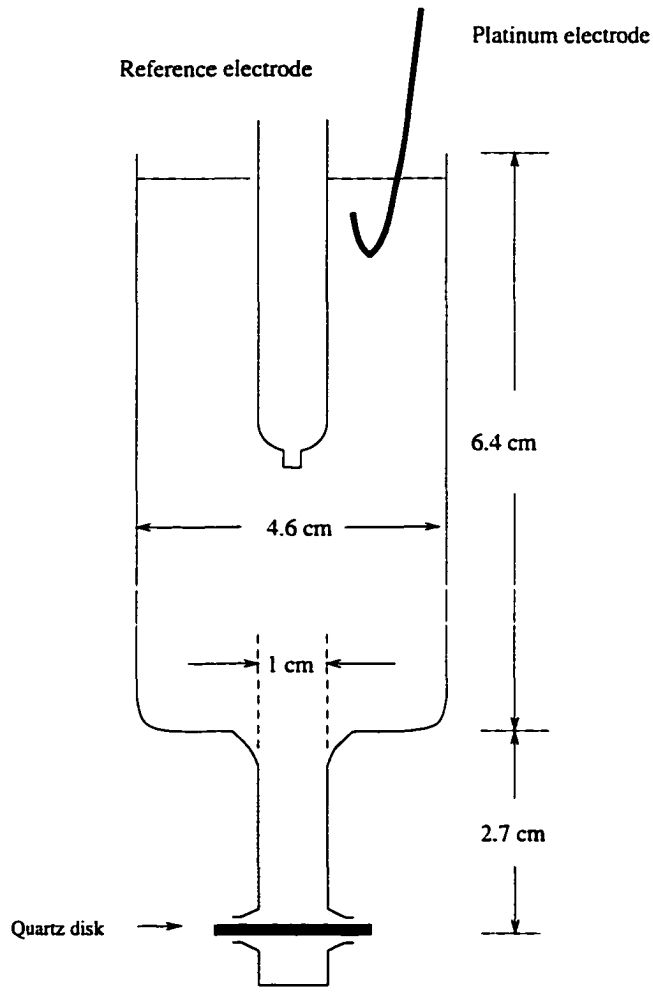

Figure 3.2 Sketch of the electrochemical cell.

The electronic part of the experimental apparatus consists of a PAR Model 273 Potentiostat/Galvanostat, a Keithley Model 194A high speed digital voltmeter, and an IBM compatible computer. Figure 3.3 shows the connections between the electronic equipment and the electrochemical cell. The PAR 273 supplied the applied potential to the cell, and meanwhile measured the current and stored the current data. The digital voltmeter was used to measure and record only fast current transients in a short period of time, because its sampling rate can be as fast as 10 μs per sample for up to 32000 samples. By using a GPIB PC-II board (National Instruments Co.), potentiostatic control and data acquisition were achieved by executing the computer programs written in QuickBasic (Microsoft) by Dr. Chin-Feng Lin. For the measurements of the small currents ($< 10\ \mu A$) in the interruption experiments (Section 3.3.3), separate experiments were performed by using a 1286 Electrochemical Interface (Schlumberger Technologies). A Fisher Recordall series 5000 pen recorder recorded the analog signals for the currents from the 1286 Electrochemical Interface.

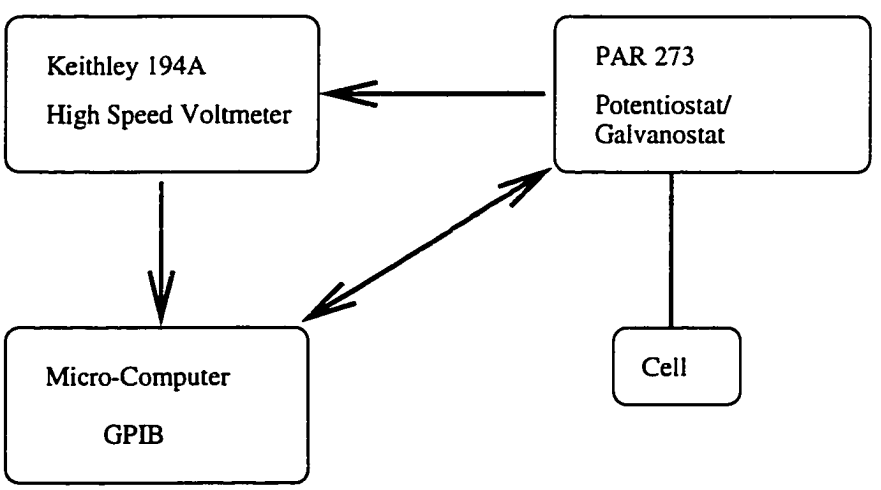

Figure 3.3 Schematic diagram of the experimental apparatus.

3.2.3 Experimental Procedure

First of all, the aluminum films on the quartz crystal mounted, in the cell, were pretreated by ca. 20 *ml* 5 wt% H_3PO_4 for 20 min prior to any electrochemical experiment. After the pretreatment, the 5 wt% H_3PO_4 solution was thrown away, and the inside of the cell, including the aluminum film, was rinsed thoroughly by plenty of deionized water to ensure no residue of phosphoric ions.

After rinsing the cell, the counter and reference electrodes were placed in the cell as shown in Figure 3.2. About 80 *ml* 0.1 M H_2SO_4 solution was then poured into the cell. Before applying potential control to the cell, the digital voltmeter was set up to measure only the initial 40-120 ms anodic current transient at -0.9 V or -0.4 V with a resolution of 10 μs. In addition, the current data for the whole experimental period were recorded.

Various types of potential waveforms were applied to the cell and the potential values were changed as necessary for each experiment. The details regarding the applied potentials will be given in the following section. In general, one of the computer programs first loaded the potential waveform information into the PAR 273. As the cell and the voltmeter had been set up, the same computer program triggered the execution of the potentiostatic experiment. Meanwhile, the digital voltmeter monitored the current passing the cell. As soon as a sudden current change, caused by a potential step, appeared, the voltmeter automatically started to record current data every 10 μs. The number of current data stored in the voltmeter for each experiment ranged from 4000 to 12000, corresponding to the periods of 40 ms to 120 ms. After the potentiostatic cycle was finished, the current data stored in the PAR 273 and in the voltmeter were transferred to the computer to be stored in data files.

3.3 Experimental Results

3.3.1 The Effect of Pretreatment

In order to have consistency between the experimental results of this work and those obtained by Lin and Hebert, the aluminum films used in the experiments of this work should have

the same quality as those used in Reference [18]. In other words, if the experiments in Reference [18] are repeated on the films prepared for this work, similar results are expected. It should be noted here that the films used in Reference [18] were deposited by thermal evaporation, instead by sputtering.

The pretreatment method described in Reference [17] was initially followed for pretreating the aluminum films deposited by sputtering. According to Reference [18], when aluminum films were immersed in 0.1 M HCl, the films were slowly dissolved and the open circuit potentials decreased with time. After 5 min immersion, the open circuit potentials were more negative than -0.9 V. However, the aluminum film samples made by IBM after 5 min immersion in 0.1 M HCl had very anodic open circuit potentials, about -0.6 V, which dropped very little after a longer immersion, eg. 30 min.

Nevertheless, a potential step used in Reference [18], in which the potential was held at -2.0 V for the first 5 sec and then was stepped to -0.9 V for a few sec, was applied to the cell. The cathodic currents at -2.0 V were as expected, but the anodic current at -0.9 V was too small to be measured. The almost zero current at -0.9 V was not consistent with the current data at -0.9 V obtained in Reference [18].

Both -0.6 V open circuit potentials and extremely small currents at -0.9 V indicated that the surface oxide layers on the aluminum films deposited by sputtering were too thick. Therefore, 5 wt% H_3PO_4, which can dissolve oxide layers quickly, replaced 0.1 M HCl as the pretreatment solution. The aluminum films pretreated by 5 wt% H_3PO_4 for 20 min have open circuit potentials of -1.0 V. The anodic current at -0.9 V decayed also as expected. Consequently, the aluminum films deposited by sputtering were all pretreated by 5 wt% H_3PO_4 for 20 min before the potentiostatic experiments.

3.3.2 Oxide Film with No Prior Cathodic Charging

The purpose of this experiment is to examine the anodic ion conduction behavior of the oxide film after pretreatment by 5 wt% H_3PO_4. After the pretreatment, the aluminum film in 0.1 M H_2SO_4 was subjected to a series of potentiostatic periods of a few milliseconds. In each

period, a constant "anodic" potential, ranging from -0.9 V to 0.6 V was applied to the cell. "Anodic" here means more positive than the open circuit potential, which was about -1.0 V. Since sulfate ions are not aggressive to aluminum, the applied potential can be fairly anodic without pitting. The currents were recorded by the digital voltmeter with a sampling rate of 10 μs. Figure 3.4 gives some of the current data at various anodic potentials. The current in each potentiostatic period decayed and/or fluctuated initially and reached a roughly stable value.

3.3.3 Interruption Experiments

In the interruption experiments, the applied potential started at -2.0 V for 5 sec and then was stepped up to -0.9 V. The -0.9 V period, ranging from 0.02 sec to 20 sec, is the interruption period, after which the applied potential was further stepped up to -0.4 V for 1 sec. The solution was again 0.1 M H_2SO_4. A typical cathodic current transient at -2.0 V is shown in Figure 3.5. The initial 10 ms anodic current data at -0.4 V after various interruption times are presented with the modeling results in Figure 5.7. The currents reached steady values in a few milliseconds. One can see that the steady current at -0.4 V decreases as the interruption time increases. This phenomenon may reflect that the electrical properties of the oxide layer were changing during the interruption period.

The anodic ion conduction behavior of the oxide layer after a 20 sec interruption was studied by changing the second anodic potential following -0.9 V. The anodic current data during the 20 sec interruption at -0.9 V are shown in Figure 5.6. The current density at the end of the interruption period was 5.7 $\mu A/cm^2$. The range of the second anodic potential here was from -0.7 V to 0.6 V. Some of the current results are shown in Figure 3.6. Again, the current reached a steady value after a short time.

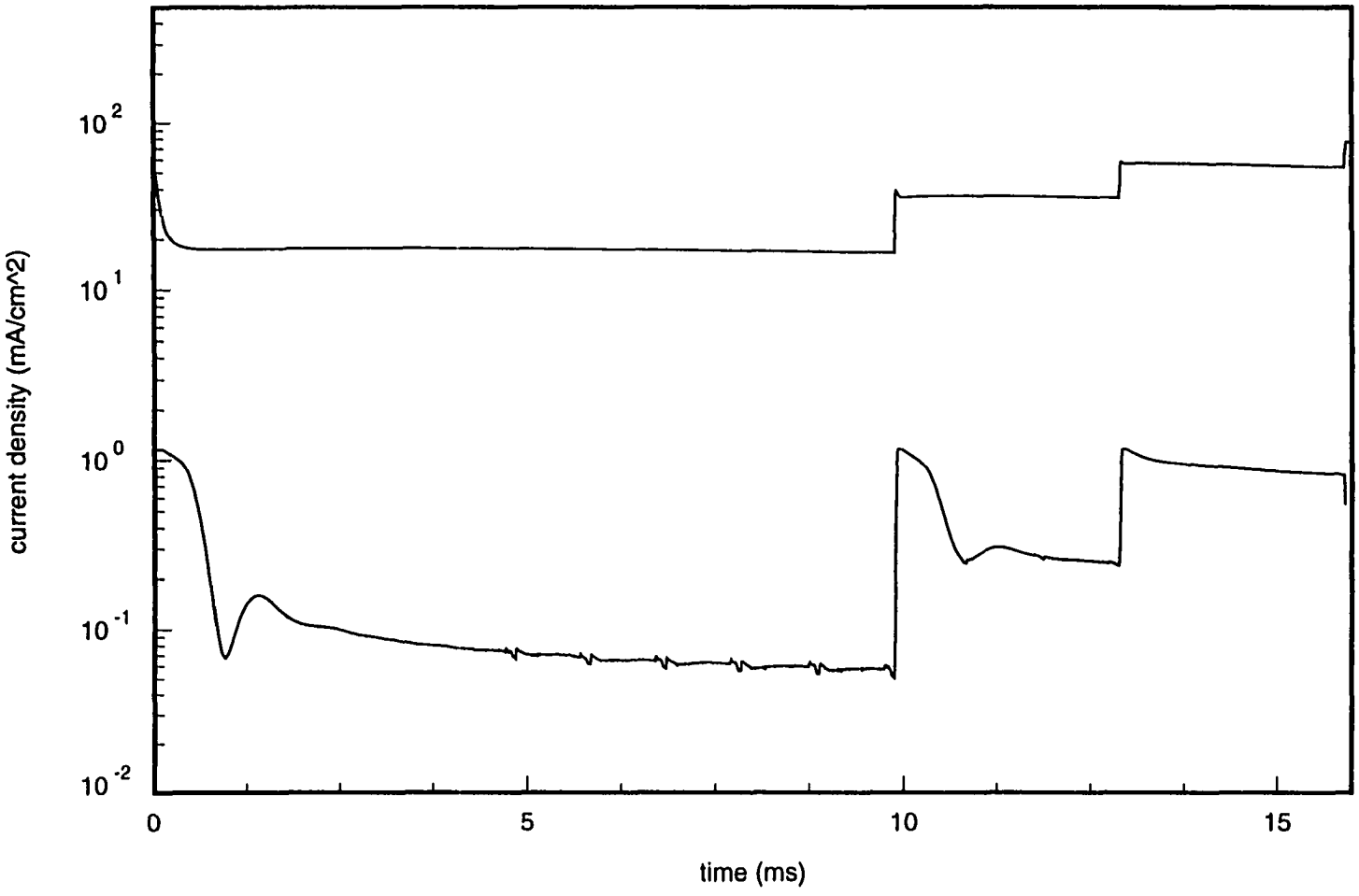

Figure 3.4 Anodic current data of the aluminum electrodes in 0.1 M H_2SO_4 with no prior cathodic charge. The potentiostatic controls for the lower curve were: 1-10 ms, -0.9 V; 10-13 ms, -0.8 V; 13-16 ms, -0.7 V. The potentiostatic controls for the upper curve were: 1-10 ms, -0.3 V; 10-13 ms, 0 V; 13-16 ms, 0.3 V.

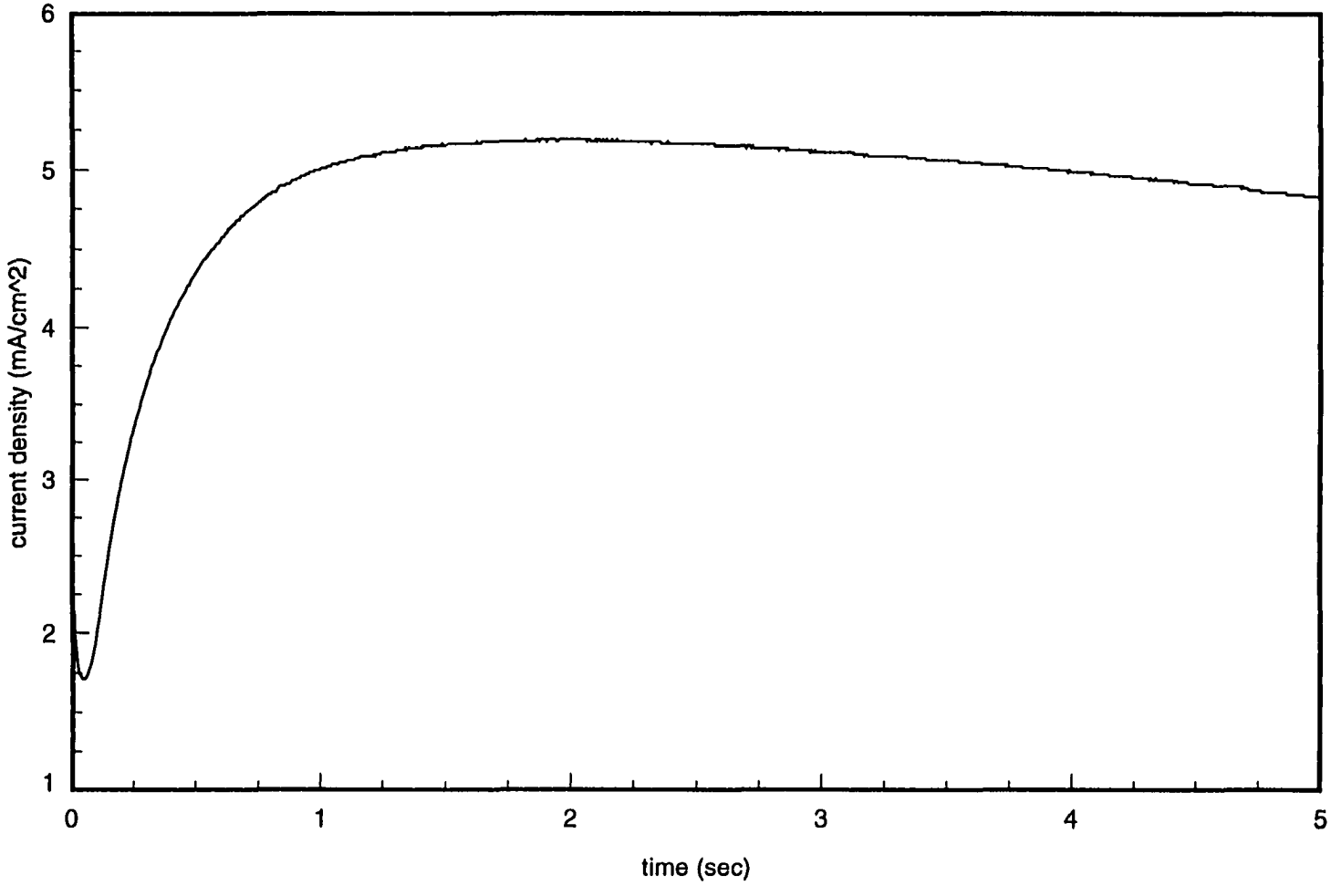

Figure 3.5 Cathodic current transient of the aluminum electrode during cathodic charging at -2.0 V. The solution was 0.1 M H_2SO_4.

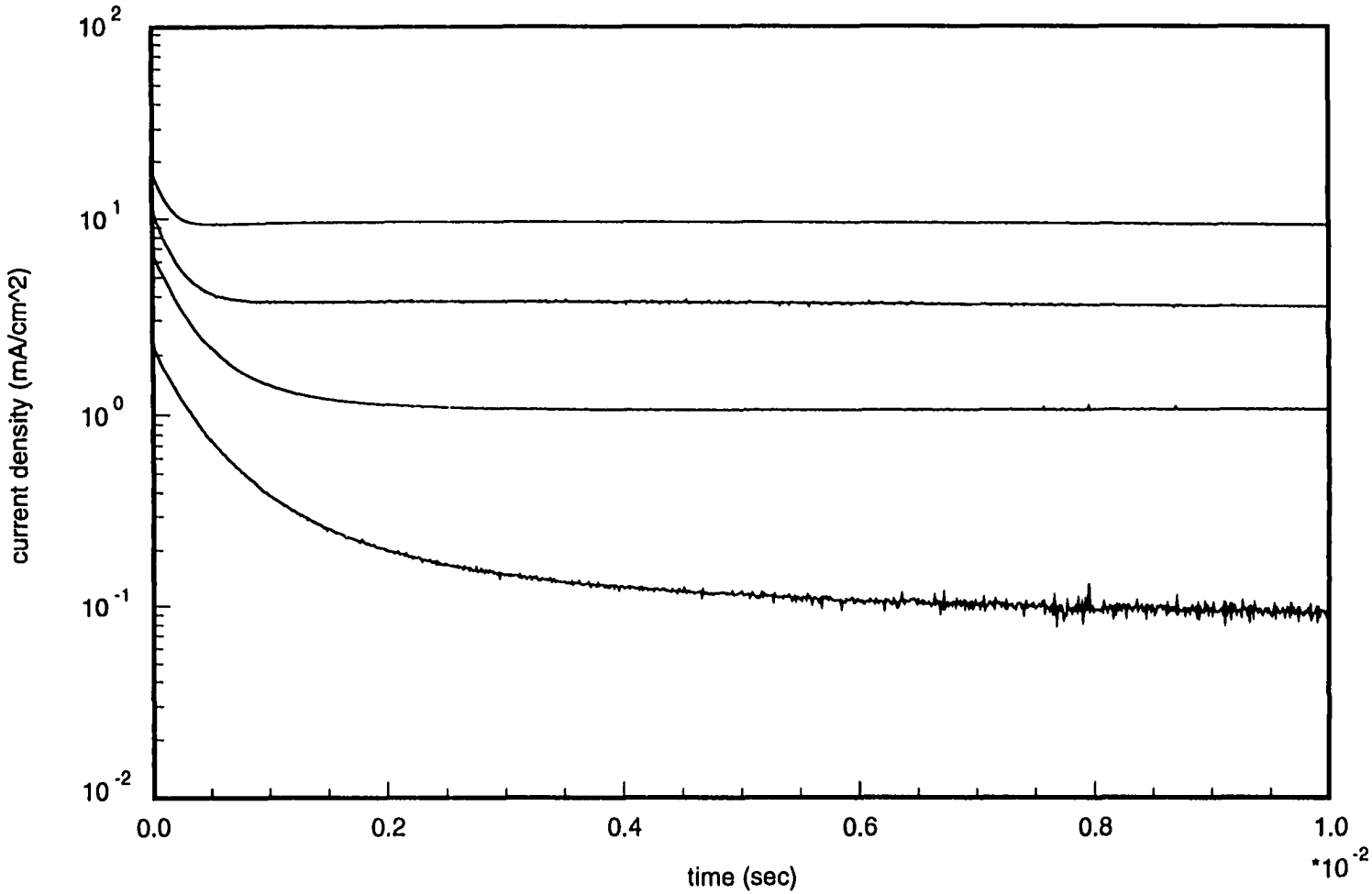

Figure 3.6 Anodic current data of the aluminum electrodes at various potentials after 20 sec interruption at -0.9 V. The solution was 0.1 M H_2SO_4. The potentials for the curves from the top to the bottom were 0.3 V, -0.1 V, -0.4 V, and -0.7 V respectively.

4 AN ELECTRICAL MODEL FOR THE ALUMINUM ELECTRODE CATHODICALLY CHARGED IN ACIDIC SOLUTIONS

4.1 Introduction

As described in Chapter 2, the rate of pitting initiation is very likely affected by the electrical resistance of the surface film. Therefore, an electrical model of the surface film is to be developed in this chapter for the understanding of its electrical properties. The basis of the electrical model is the thermodynamic model of Hebert and Lin [32] [18], which will be briefly presented first. Also, the structure of the surface film needs to be described before the electrical model is introduced. The electrical model consists of its mathematical equations with some parameters related to the electrical resistance of the surface film. These parameters are determined by fitting current modeling results to experimental current transients as described in Chapter 5.

4.2 Thermodynamic Model

The thermodynamic model for the aluminum electrode in acidic solutions was developed by Hebert and Lin [32] [18]. This model includes both cathodic and anodic electrochemical processes. The change of the film composition, caused by electrochemical processes, can be predicted by this model as well. In contrast, Kirchheim's model, as described in Chapter 1, is mainly a kinetic model and can only be applied to oxide film growth. This section briefly presents this thermodynamic model and introduces the model equations, which are useful for the derivation of the electrical model later in this chapter.

The electrochemical and chemical reactions considered in the thermodynamic model is

presented in Figure 4.1. The reactions at metal-film interface are aluminum oxidation and hydrogen evolution;

$$Al_{[12]} \rightarrow Al^{+3}_{[21]} + 3e^{-}, \tag{4.1}$$

$$H^{+}_{[21]} + e^{-} \rightarrow \frac{1}{2} H_{2[21]}. \tag{4.2}$$

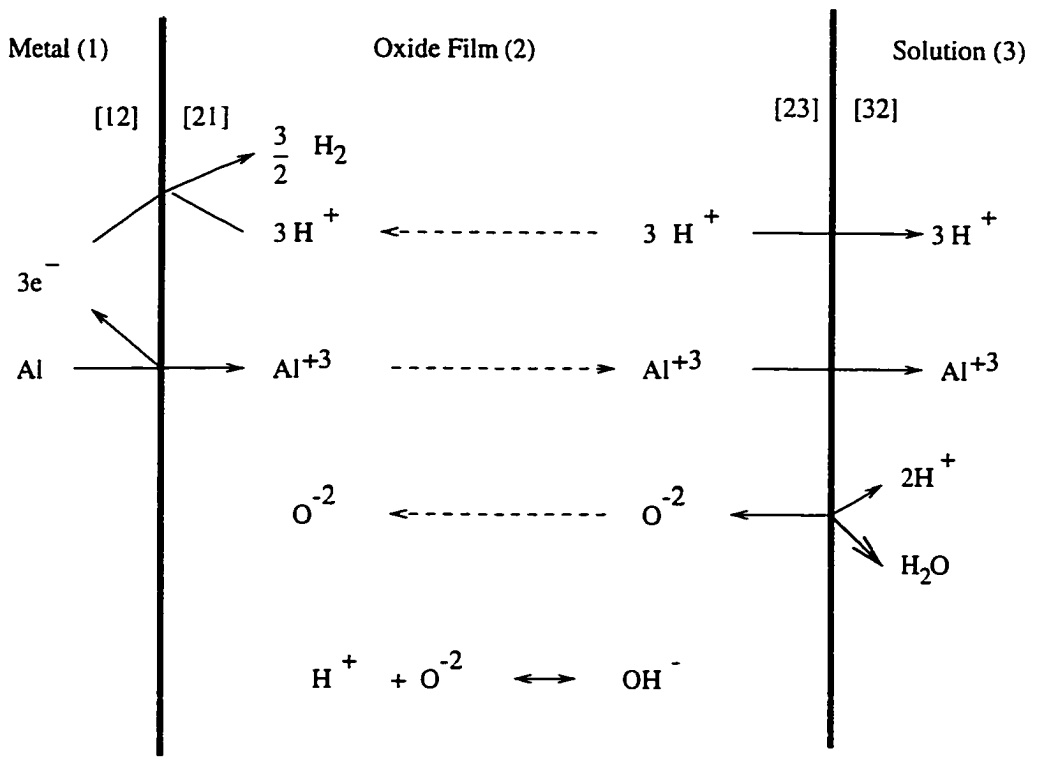

Figure 4.1 Schematic presentation of electrochemical and chemical reactions in the metal/film/solution system of the aluminum electrode in acidic solutions.

The numbers in square brackets denote the locations of the chemical species, as shown in Figure 4.1. For instance, "[12]" means inside Phase 1 and adjacent to Phase 2. "[21]" means inside Phase 2 and adjacent to Phase 1. Both reactions are considered to be irreversible. At the film-solution interface, aluminum ions, hydrogen ions, and oxide ions are transferred across the interface;

$$Al^{+3}_{[23]} \rightleftharpoons Al^{+3}_{[32]}, \tag{4.3}$$

$$H^{+}_{[23]} \rightleftharpoons H^{+}_{[32]}, \tag{4.4}$$

$$O^{-2}_{[23]} + 2H^{+}_{[32]} \rightleftharpoons H_2O_{[32]}. \tag{4.5}$$

The film is considered to be composed of aluminum oxide and aluminum hydroxide, in which hydrogen ions, oxide ions and hydroxide ions are at equilibrium, namely

$$O^{-2} + H^{+} \rightleftharpoons OH^{-}, \tag{4.6}$$

or equivalently,

$$Al_2O_3 + V^{\equiv\equiv\equiv}_{Al} + 3H^{+} \rightleftharpoons Al(OH)_3, \tag{4.7}$$

$$Al_2O_3 + H_3V_{Al} \rightleftharpoons Al(OH)_3. \tag{4.8}$$

$V^{\equiv\equiv\equiv}_{Al}$ is the vacancy created by the removal of an aluminum ion from its lattice site. H_3V_{Al} is created by the occupation of the vacancy $V^{\equiv\equiv\equiv}_{Al}$ by three hydrogen ions as

$$H_3V_{Al} \rightleftharpoons V^{\equiv\equiv\equiv}_{Al} + 3H^{+}. \tag{4.9}$$

Let electrochemical potential be relative to the hydrogen electrode in equilibrium with the solution (Phase 3 in Figure 4.1). The potential difference between the metal phase and the reference electrode is written as

$$V_H = \eta^{12}_H + \eta^{2}_H + \eta^{23}_H + \eta^{3}_H, \tag{4.10}$$

where

$$F\eta^{12}_H = \frac{1}{2}\mu^{[21]}_{H_2} - \mu^{[12]}_{e^-} - \mu^{[21]}_{H^+}, \tag{4.11}$$

$$F\eta^{2}_H = \mu^{[21]}_{H^+} - \mu^{[23]}_{H^+}, \tag{4.12}$$

$$F\eta^{23}_H = \mu^{[23]}_{H^+} - \mu^{[32]}_{H^+}, \tag{4.13}$$

$$F\eta^{3}_H = \mu^{[32]}_{H^+} - \mu_{H^+} \text{ (at ref. electrode)}. \tag{4.14}$$

The subscript "H" denotes that hydrogen ions are transfered between phases or transported within phases. Similarly, if the transfer and the transport of aluminum ions are considered, the overpotential η^{12}_{Al} for Reaction 4.1 is written as

$$3F\eta^{12}_{Al} = \mu^{[12]}_{Al} - 3\mu^{[12]}_{e^-} - \mu^{[21]}_{Al^{+3}}. \tag{4.15}$$

Using Equation 4.11, the relation between η_H^{12} and η_{Al}^{12} is

$$3F\eta_H^{12} = 3F\eta_{Al}^{12} + (\mu_{Al_2O_3}^{[21]} - \mu_{Al(OH)_3}^{[21]}) + \frac{3}{2}\mu_{H_2}^{[21]} - \mu_{Al}^{[12]}. \tag{4.16}$$

As shown in Kirchheim's model, the overpotential η_O^{23} drives the reactions at the film-solution interface. According to Equation 1.8, η_O^{23} can be expressed as

$$2F\eta_O^{23} = \mu_{H_2O}^{[32]} - 2\mu_{H^+}^{[32]} - \mu_{O^{-2}}^{[23]}. \tag{4.17}$$

η_O^{23} can be related to η_H^{23} as

$$3F\eta_H^{23} = 3F\eta_O^{23} - \frac{1}{2}\mu_{Al_2O_3}^{[23]} + \mu_{Al(OH)_3}^{[23]} - \frac{3}{2}\mu_{H_2O}^{[32]}. \tag{4.18}$$

By substituting Equations 4.16 and 4.18 into Equation 4.10, one can obtain the following equation for V_H in terms of η_{Al}^{12} and η_O^{23}.

$$\begin{aligned} V_H &= \eta_{Al}^{12} + \eta_H^2 + \eta_O^{23} + \eta_H^3 + \frac{1}{3F}(\mu_{Al_2O_3}^{[21]} - \mu_{Al(OH)_3}^{[21]} - \frac{1}{2}\mu_{Al_2O_3}^{[23]} \\ &\quad +\mu_{Al(OH)_3}^{[23]} - \frac{3}{2}\mu_{H_2O}^{[32]} + \frac{3}{2}\mu_{H_2}^{[21]} - \mu_{Al}^{[12]}). \end{aligned} \tag{4.19}$$

Let $U_{Al/Al_2O_3} = \frac{1}{6F}(3\mu_{H_2}^{[21]} - 2\mu_{Al}^{[12]} - 3\mu_{H_2O} + \mu_{Al_2O_3}^{[21]})$. Then the above equation can be rearranged into

$$\begin{aligned} V_H &= \eta_{Al}^{12} + \eta_H^2 + \eta_O^{23} + \eta_H^3 + U_{Al_2O_3} \\ &\quad +\frac{1}{3F}[(\frac{1}{2}\mu_{Al_2O_3}^{[21]} - \mu_{Al(OH)_3}^{[21]}) - (\frac{1}{2}\mu_{Al_2O_3}^{[23]} - \mu_{Al(OH)_3}^{[23]})]. \end{aligned} \tag{4.20}$$

For simplicity, the composition of the surface oxide/hydroxide film is considered to be homogeneous. Also $\mu_{H_2}^{[21]} = 0$ and $\mu_{Al}^{[12]} = 0$ are assumed. If the surface film is a thermodynamically ideal mixture, then the chemical potential of aluminum oxide can be approximately related to its mole fraction $x_{Al_2O_3}$ in the film as,

$$\mu_{Al_2O_3} = \mu_{Al_2O_3}^{\circ} + RT \ln x_{Al_2O_3}, \tag{4.21}$$

Equation 4.20 can be simplified to

$$V_H = \eta_{Al}^{12} + \eta_H^2 + \eta_O^{23} + \eta_H^3 + U_{Al/Al_2O_3}^{\circ} + \frac{RT}{6F} \ln x_{Al_2O_3}. \tag{4.22}$$

$U^{\circ}_{Al/Al_2O_3}(= \frac{1}{6F}[\mu^{\circ}_{Al_2O_3} - 3\mu^{\circ}_{H_2O}])$ is -1.5 V if the standard chemical potentials of Al_2O_3 and H_2O are taken as -1582.3 $kJ\ mol^{-1}$ and -237.129 $kJ\ mol^{-1}$ respectively [33]. Otherwise, the chemical potentials of Al_2O_3 and $Al(OH)_3$ in Reference [45] are -380.5 $kcal/mol$ and -271.9 $kcal/mol$ and then U°_{Al/Al_2O_3} is -1.57 V. In the case of no concentration gradient in the film and the solution, η^2_H and η^3_H are solely the ohmic potential drops in Phases 2 and 3 respectively.

4.3 Structural Model

According to the IRS results described in Chapter 2, in case of cathodic charge more than 7.2 mC/cm^2, the physical structure of cathodically charged surface film on aluminum is assumed to consist of an inner barrier layer and an outer porous layer. The inner layer is mainly the native air-formed oxide layer. However, some micropores can form on this native oxide film due to non-uniform dissolution during early cathodic polarization. Figure 4.2 presents the physical structure model of a highly cathodically charged surface film on aluminum. Phases 1, 2, 2', and 3 denote the phases metal, inner layer, porous layer, and solution respectively. Again, the outer porous layer started to grow only after a cathodic charge more than 7.2 mC/cm^2. Therefore, for the cases of low or no prior cathodic charge, Phase 2' is not present. However, the micropores may form at the film-solution interface even in case of low cathodic charges. Although the drawing depicts straight pores, the geometry was not required in the model.

4.4 Electrical Model

According to the structural model, the thermodynamic model, and the film growth model, the electrical model is to be formulated in this section. Naturally, the assumptions and simplifications applied in the model are introduced here as well. The mathematical equations are derived with the aid of an equivalent electrical network, shown in Figure 4.3. R_3 is the ohmic resistance of the solution in the cell. Z_p is the porous layer impedance. R_2 represents the high-field electrical resistance of the inner barrier layer. R_f represents the kinetic resistance of film growth at pore bottoms, which is neglected if cathodic current is involved. C_2 is the capacitance of the barrier layer. The relative contributions of the interfaces and the bulk of

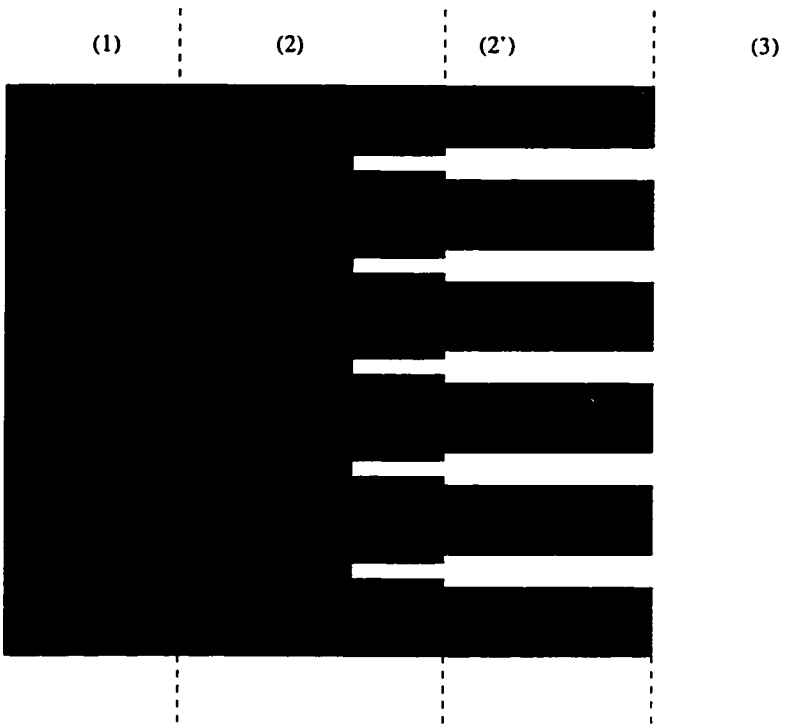

Figure 4.2 Sketch of the surface film structure for the model.

the barrier layer to C_2 cannot be separated easily. Bessone *et al.* [38] proposed an inductance parallel with R_f to account for the charge transfer processes at the film-solution interface. However, for the minimization of the number of unknown parameters to be fitted later in the calculation, the element of C_2 will not be further differentiated.

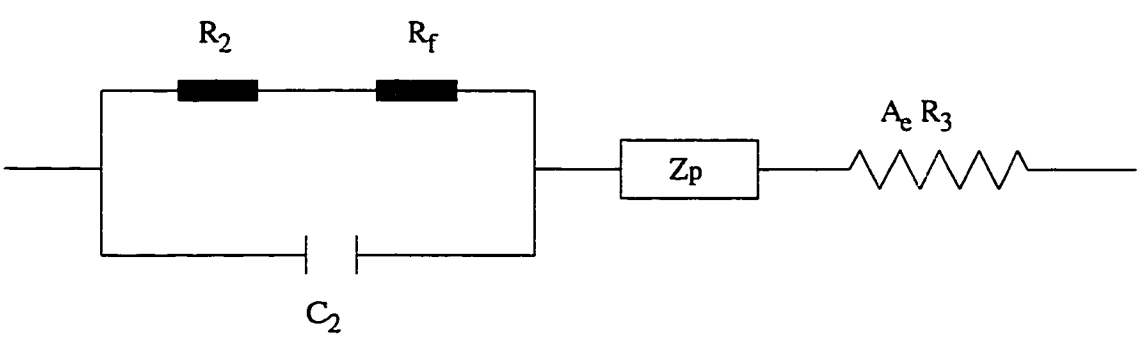

Figure 4.3 Equivalent electrical network for the electrical model.

As mentioned before, the modeling results are compared with the current transients vs. time at a potential of -0.9 V immediately after cathodic charging at a potential of -2.0 V. Therefore, one needs to develop an intuitive feeling that a potential step is involved in the initial conditions of the modeling equations. A step change of potential triggers the charging processes in the the metal/film/solution system.

4.4.1 Porous Layer Impedance

The porous layer of the surface film may be treated as a porous electrode. Because of numerous industrial applications of porous electrodes, researchers have been seeking methods for designing more efficient porous electrodes. Particularly, a large number of authors have established the mathematical equations to describe the charge transport processes along with the kinetic reactions inside two phase porous electrodes [34] [35]. The solutions of the mathematical equations give the time and spatial dependences of current and potential. Therefore, the electrode impedance can be obtained. However, the calculation of the impedance values requires the knowledge of the geometrical parameters of the porous electrode, the electrical conductivities of both phases, and the kinetic parameters of the electrochemical processes. Unfortunately, the knowledge regarding these parameters of the porous layer here is not complete. Besides, the metal/film/solution system of the aluminum electrode is mathematically more complicated than the two phase system of the porous electrode, since the latter system is only equivalent to the porous-layer part of the former system.

One can easily understand the charging process in the porous layer by examining the current flow in a single pore in the porous layer, as shown in Figure 4.4. The pore is assumed to be an axisymmetric cylinder with a diameter much less than the length, L. Since the pore cross section is so small, the current and potential distributions in the pore are considered to be one-dimensional functions (x-dimension). Also, the electrical resistance of the solid phase is regarded as infinite while compared with that of the aqueous phase, so the current flows through the porous layer only by the aqueous pathway. By taking a stationary volume element

through which the current is flowing, one can write a charge balance equation as,

$$(i_p|_x - i_p|_{(x+\Delta x)})\pi r^2 = C_p(2\pi r_p)\Delta x \frac{\partial(\phi_p - \phi_s)}{\partial t}. \tag{4.23}$$

i_p is the current density inside the pore. In the absence of concentration gradient, ϕ_p is the electrostatic potential inside the pore. C_p is the capacitance of the pore wall. r_p is the pore radius. ϕ_s is the potential of the pore wall. By dividing this entire equation by Δx and taking the limit as $x \to 0$, one gets

$$-\frac{\partial i_p}{\partial x} = \frac{2C_p}{r_p}\frac{\partial(\phi_p - \phi_s)}{\partial t}. \tag{4.24}$$

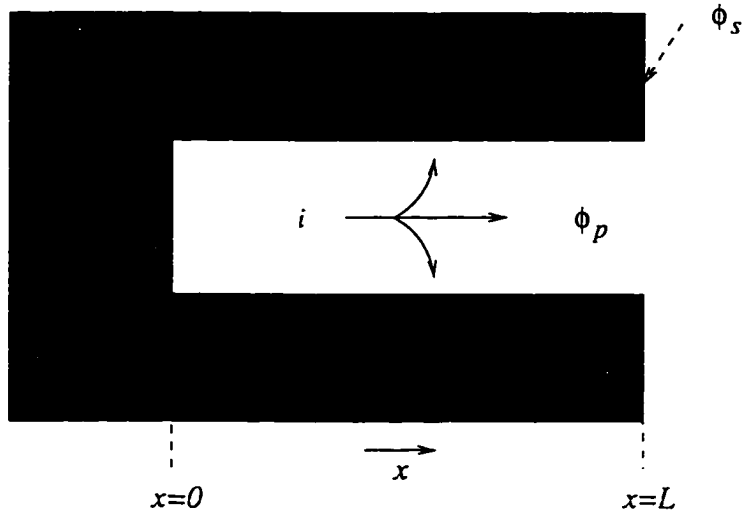

Figure 4.4 Current flow in a pore of the porous layer.

Since the charge flow in the solid phase is very sluggish while compared with that in the aqueous phase, ϕ_s can be regarded as a constant with respect to time while compared with ϕ_p. $\phi_p(x)$ and $i_p(x)$ are related by Ohm's law. Therefore, Equation 4.24 is rewritten as

$$\frac{\partial \phi_p}{\partial t} = \frac{\kappa_p r_p}{2C_p}\frac{\partial^2 \phi_p}{\partial x^2}, \tag{4.25}$$

The preceding method of charge balancing can be applied macroscopically to the porous layer and leads to the following equation,

$$\frac{\partial \phi_p}{\partial t} = \alpha \frac{\partial^2 \phi_p}{\partial x^2}, \tag{4.26}$$

where

$$\alpha = \frac{\kappa}{C_p a}. \tag{4.27}$$

a is the interfacial area per unit volume of the porous layer. κ is the apparent electrical conductivity of the porous layer. Let p be the porosity, then $\kappa = \kappa_p p$. Since $a = 2p/r_p$, Equations 4.26 and 4.25 are in fact equivalent.

The boundary conditions for equation 4.26 are as follows;

$$\phi_p(L,t) = 0, \tag{4.28}$$

$$i(t) = -\kappa \frac{\partial \phi_p}{\partial x}|_{(x=0)}. \tag{4.29}$$

The initial condition is

$$\phi_p(x,0) = i(0^-)\frac{L}{\kappa}(1 - \frac{x}{L}), \tag{4.30}$$

where $i(0^-)$ is the current density at the time immediately *before* the potential step. The charging of the micropores is assumed negligible while compared with that of the porous layer.

4.4.2 Kinetic Resistances

The overpotential at the film-solution interface, η_O^{23}, can be determined by using Equations 1.6 and 1.7. The parameters in both equations were obtained by Lin and Hebert [18] according to the work of Våland and Heusler [44]. The value of i_{co}, $3.6\times10^{-6}A/cm^2$, is the stationary current density at constant potential and film thickness. The values of the other parameters were derived from the experimental data as $i_{lo} = 2.6\times10^{-6}A/cm^2$, $\alpha_c = 1.11$, $\alpha_l^+ = 1.76$, and $\alpha_l^- = 0.24$. However, Equations 1.6 and 1.7 are not applicable when the current density is cathodic and hydrogen evolution reaction is involved. Consequently, the assumption of $\eta_O^{23} = 0$ is used when cathodic current is involved.

Since both anions and cations could contribute to the anodic current [39], film could grow at either the metal-film interface or the film-solution interface. For the metal/film/solution system, film growth results in pore filling and and therefore the thickness of the barrier layer increases. Since the density of aluminum oxide, about 3 g/cm^2, is very likely higher than that of the pore solution, pore filling may be accompanied by the mass increase of the film,

which was observed during anodic current transient by using QCM [18]. Hence, the pore filling process is included in the model and its relevant equations are given in Section 4.4.4.

The kinetic resistance of aluminum oxidation at the metal-film interface is assumed to be negligible so that $\eta_{Al}^{12} = 0$. This assumption is likely to be valid as the overpotential across the metal-film interface is taken as a constant in Kirchheim's model [1].

On the other hand, the kinetic resistance of hydrogen evolution at the metal-film interface during cathodic charging may be significant. Since the aluminum oxidation reaction also takes place during cathodic charging, $\eta_{Al}^{12} = 0$ has been assumed. As a consequence, according to Equation 4.16, the overpotential for hydrogen evolution, η_H^{12}, is about -1.5 V, which may be considered cathodic enough to account for the kinetic resistance of hydrogen evolution.

4.4.3 Barrier Layer Resistance and Capacitance

The galvanostatic method of Kirchheim [1] was applied to aluminum with only air-formed oxide film in 0.05 M H_2SO_4 by Lin and Hebert [11] to investigate the anodic ion conduction rate law for the surface film. The anodic ion conduction in the barrier layer obeys the high field conduction equation,

$$i = i_o^a \exp(\frac{B_a \phi_2}{\xi}), \tag{4.31}$$

with $i_o^a = 9.8 \times 10^{-12} A/cm^2$ and $B_a = 4.86 \times 10^{-6} cm/V$. ϕ_2 is the potential drop across the barrier layer and ξ is the film thickness. The value of B_a is close to some literature values reported by a few authors, such as $3.8 \times 10^{-6} cm/V$ by Young [41], $4.8 \times 10^{-6} cm/V$ by Bernard and Cook [42], and $3 \times 10^{-6} cm/V$ by Charlesby [43]. However, the values of i_o^a obtained by them are $8 \times 10^{-13} A/cm^2$ [41], $10^{-22} A/cm^2$ [42], and $10^{-18} A/cm^2$ [43], which are inconsistent with each other. It should be noted that the oxide films used by these authors are anodic oxide films in neutral solutions with a thickness more than 500 Å, in contrast to the 30 Å air-formed oxide film in acidic solutions used by Lin and Hebert. Therefore, $9.8 \times 10^{-12} A/cm^2$ for i_o^a is acceptable even though it is fairly different from any literature value.

On the other hand, during cathodic charging at -2.0 V, the cathodic current mainly results from hydrogen ion migration through the barrier layer and reduction at the metal/film inter-

face. According to the cathodic polarization experiment performed by Lin and Hebert [11], the empirical Tafel slope for the hydrogen evolution reaction on the aluminum electrode in 0.1 M HCl is 0.096 V. This Tafel slope accounts for both the kinetic resistance at the metal/film interface and the electrical resistance in the surface film, since the overpotential in the empirical Tafel equation is in fact $(\eta_H^{12} + \eta_H^2)$. Meanwhile, the empirical exchange current density from the cathodic polarization curve is $5.73\times10^{-19} A/cm^2$. With η_H^{12} approximately equal to -1.5 V, an empirical cathodic ion conduction rate law may therefore be written as

$$i = -i_o^c \exp(-\frac{\eta_H^2}{b^-}), \tag{4.32}$$

with i_o^c on the order of 10^{-4} A/cm^2 and $b^- = 0.096/\ln 10$. η_H^2 is equivalent to ϕ_2 due to the absence of the porous layer.

As a consequence, for the modeling calculation, the relation between the current density and the potential drop across the barrier layer is written as

$$i = i_o^a[\exp(\frac{B_a\phi_2}{\xi}) - \exp(-\frac{B_a\phi_2}{\xi})] + i_o^c[\exp(\frac{\phi_2}{b^+}) - \exp(-\frac{\phi_2}{b^-})]. \tag{4.33}$$

In a general way, the first term on the right side of the equation is meant for the anodic current density ($i > 0$), and the second term is meant for the cathodic current density ($i < 0$). According to this equation, as the electric field vanishes, so does the current density. In fact, i_o^c is expected to be decreasing when $i > 0$, because hydrogen ions are being depleted from the inner layer. However, i_o^c is assumed to be a constant for simplicity. In order to dominate the first term for the case of $\phi_2 > 0$, one needs to enforce the condition of $\frac{\xi}{B_a} << b^+$ because of $i_o^c >> i_o^a$. Figure 4.5 presents a plot of i vs. ϕ_2 according to Equation 4.33. The parameters applied in the equation for the plotting are for the case of $Q_c = 60.2$ mC/cm^2 in Figure 5.1.

The formation of micropores on the surface of the inner layer reduces its overall electrical resistance. Therefore, ξ in Equation 4.33 is *not* the physical thickness but the electrically effective thickness. As the micropores are filled by film formation during $i > 0$, the overall electrical resistance of the inner layer is restored and ξ increases.

The geometric capacitance of the barrier type oxide film can be determined by the thickness,

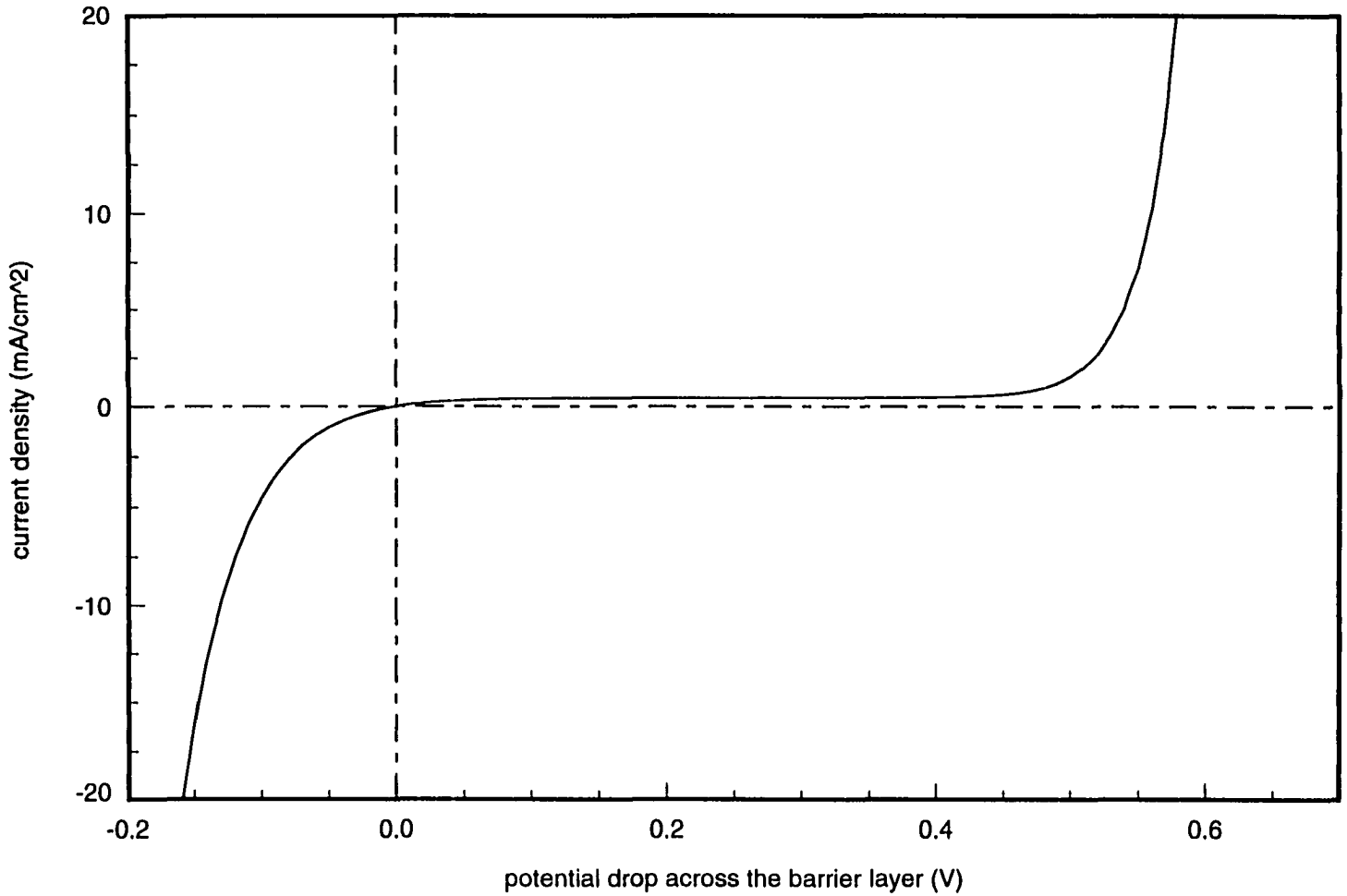

Figure 4.5 The polarization curve of i vs. ϕ_2 according to Equation 3.34 with $\xi = 13$ Å, $i_o^c = 4.5\times10^{-4}$ A/cm^2 and $b^+ = 26.75$ V.

ξ, and the dielectric constant, ϵ, of the film as

$$C = \frac{\epsilon\epsilon_o}{\xi}, \tag{4.34}$$

where ϵ_o is the permittivity of the vacuum. The literature values of ϵ are between 8 and 15 [37].

4.4.4 Pore Filling

According to the assumptions made so far and Equation 4.22, the potential difference across the metal/film/solution system can be expressed as

$$V_H - V_r = \phi_2 + \eta_O + \phi_p + i(A_e R_3), \tag{4.35}$$

where A_e is the electrode surface area and V_r is the rest potential of aluminum oxidation reaction at the metal/film interface, namely

$$V_r = -1.5 \text{ V} + \frac{RT}{6F} \ln x_{Al_2O_3}. \tag{4.36}$$

η_O is the overpotential for the film formation/dissolution reaction at pore bottoms. Based on the electrical network, the total current density, i, is related to ϕ_2 and η_O as

$$\begin{aligned} i &= C_2 \frac{\partial(\phi_2 + \eta_O)}{\partial t} + \{i_o^a[\exp(\frac{B_a\phi_2}{\xi}) - \exp(-\frac{B_a\phi_2}{\xi})] + \\ &\quad i_o^c[\exp(\frac{\phi_2}{b^+}) - \exp(-\frac{\phi_2}{b^-})]\}, \end{aligned} \tag{4.37}$$

and

$$\begin{aligned} i &= C_2 \frac{\partial(\phi_2 + \eta_O)}{\partial t} + p\{i_{lo}[\exp(\frac{\alpha_l^+ F}{RT}\eta_O) + \exp(-\frac{\alpha_l^- F}{RT}\eta_O)] + \\ &\quad i_{co}\exp(\frac{\alpha_c F}{RT}\eta_O)\}. \end{aligned} \tag{4.38}$$

In other words, the total current is the sum of the charging current of C_2 and the current passing through R_2 and R_f. p is used in Equation 4.38 as the current density in the pore solution is i/p. The initial conditions of ϕ_2 and η_O are $\phi_2(t = 0^-)$ and $\eta_O(t = 0^-)$ and are dependent on the current density immediately *before* the potential step, $i(0^-)$. With the

assumption of no film growth at the metal-film interface, the growth rate of the inner layer is determined by i_l as

$$\frac{d\xi}{dt} = \frac{i_l V_{ox}}{3F}, \tag{4.39}$$

where V_{ox} is the molar volume of aluminum oxide, which is 20 cm^3/mol for $AlOOH$ [18]. The initial condition of i is obtained from the experimental data and $A_e R_3$ is therefore calculated from the experimental change in current at the potential step as

$$A_e R_3 = \frac{\Delta V_H}{i(0) - i(0^-)}, \tag{4.40}$$

where ΔV_H is the potential step. However, when the applied potential is stepped from -2.0 V to -0.9 V, the micropores in the surface portion of the inner layer are to be filled up first. For this case, $i(0^-)$ is cathodic, so $\eta_O^{23} = 0$ is assumed. Hence, the inner layer growth under the condition of anodic current is described by the following equation:

$$\frac{d\xi}{dt} = [i - C_2 \frac{d\phi_2}{dt}] \frac{V_{ox}}{3F p_i}. \tag{4.41}$$

p_i is the porosity of the surface porous portion of the inner layer.

So far, all the differential equations required for the calculation in Chapter 5 have been introduced. Although two discrete porosity factors, p and p_i, are used in the model for pore filling of the inner layer and the porous layer, the porosity of the surface film on aluminum is likely to decrease continuously with distance from the film-solution interface. Thus, the separation of micropores from the porous layer might oversimplify the variation of the porosity within the film. Hence, in case of cathodic charge more than 7.2 mC/cm^2 for which the porous layer is present, the transition from p_i to p in the calculation in Chapter 5 depends on the fitting between the modeling results and the experimental data. Basically, p_i is used for the modeling of the current decay at early time and p is used for that at long time. On the other hand, in case of cathodic charge less than 7.2 mC/cm^2 for which no porous layer is present, only p_i is used for the modeling calculation.

5 MATHEMATICAL METHODS AND RESULTS

5.1 Mathematical Methods

The differential equations to be solved are all ordinary differential equations (ODE) except Equation 4.26, which is a partial differential equation (PDE). Consequently, the orthogonal collocation method is applied to convert the PDE into a group of ODE's. The reader is referred to Reference [46] for more details regarding this method. In brief, the number of the ODE's generated from the PDE is equal to the number of the collocation points. The collocation points are taken as the roots of orthogonal polynomials, which are given in Table 4-3 of Reference [46]. The dependent variables in each ODE are the solution values at the collocation points.

The conversion of the PDE problem including Equation 4.26 into ODE's and Equation 4.29 into an algebraic equation is achieved by the application of the following formulas;

$$\frac{d\mathbf{y}}{dx} = \mathbf{A}\mathbf{y} \text{ and } \frac{d^2\mathbf{y}}{dx^2} = \mathbf{B}\mathbf{y}. \tag{5.1}$$

$\mathbf{y}$ is the $N\times 1$ matrix of the dependent variables. $\mathbf{A}$ and $\mathbf{B}$ are $N\times N$ constant matrices determined by polynomial roots (collocation points). The range of x is from 0 to 1. Therefore, one needs to rewrite Equations 4.26 and 4.29 in a dimensionless form, namely

$$\frac{\partial \phi_p}{\partial \tilde{t}} = \frac{\partial^2 \phi_p}{\partial \tilde{x}^2}, \tag{5.2}$$

$$i = -\frac{\kappa}{L}\frac{\partial \phi_p}{\partial \tilde{x}}, \tag{5.3}$$

where

$$\tilde{x} = \frac{x}{L} \text{ and } \tilde{t} = \frac{\alpha}{L^2}t. \tag{5.4}$$

Then the ODE's from Equation 5.2 are

$$\frac{d\phi_{p,j}}{d\tilde{t}} = \sum_{k=1}^{N} B_{jk}\phi_{p,k}, \tag{5.5}$$

where $1 \leq j \leq N-1$. N is the number of the collocation points. The collocation point for $j = N$ is $x = L$. According to the boundary condition Equation 4.28,

$$\frac{d\phi_{p,N}}{d\tilde{t}} = 0. \tag{5.6}$$

The other boundary condition, Equation 5.3, is converted into

$$-\frac{\kappa}{L}\sum_{k=1}^{N} A_{1k}\phi_{p,k} = i. \tag{5.7}$$

By using Equations 4.35 and 5.7, one gets

$$\phi_{p,1} = [V_H - V_r - \phi_2 - \eta_O + \frac{A_e R_3 \kappa}{L}\sum_{k=2}^{N} A_{1,k}\phi_{p,k}]/[1 - \frac{A_e R_3 \kappa}{L}A_{1,1}]. \tag{5.8}$$

The above equation must be substituted into Equation 5.5 for the enforcement of the boundary condition at $\tilde{x} = 0$ [46].

The initial conditions of $\phi_{p,j}$'s for $2 \leq j \leq N$ are

$$\phi_{p,j}(0^-) = i(0^-)\frac{L}{\kappa}(1 - \tilde{x}_j), \tag{5.9}$$

where $\tilde{x}_j$'s are the collocation points. $\phi_{p,1}(0)$ should be calculated from Equation 5.8 so the boundary condition Equation 4.29 at $t = 0$ can be satisfied. As a consequence, at $t = 0$, the potential slope with respect to x at x_1 is $-i(0)/\kappa$ but that at x_2 is $-i(0^-)/\kappa$. As more collocation points are used, the calculation results are closer to the exact solutions. Therefore, the potential profile near $\tilde{x} = 0$ at small $\tilde{t}$ can be properly approximated by the collocation method if the difference between $\tilde{x}_1$ and $\tilde{x}_2$ is small enough. In other words, the number of collocation points cannot be too small or the calculation error will be unacceptable.

The choices of the mathematical equations from the electrical model for the modeling calculations depend on the experimental conditions under which the experimental data were obtained. Nevertheless, the mathematical problems encountered were all initial value problems. They are solved numerically by a Gear method. "IVPAG" Fortran subroutine supported by IMSL Math/Library was used to perform the numerical calculation. Appendix B gives one of the computer programs written for this work.

5.2 Characteristics of Mathematical Solutions

The calculated current transient induced by a potential step applied to the metal/film-/solution system is approximately composed of three parts with different time constants. The charging of C_2 in the electrical network corresponds to the initial exponential current decay with a time constant of roughly 0.2 ms. As soon as C_2 is about fully charged, the charging of the porous layer dominates in contributing to current decay. The time constant of the porous layer charging process is about a few milliseconds. The growth of the barrier layer through pore filling is responsible for the current decay after both capacitive charging processes are finished.

The unknown parameters in the equations, determined through fitting of experimental data and calculation results, are the electrically effective thickness of the inner layer, ξ, the capacitance of the inner layer, C_2, the porosities, p_i and p, and two lumped parameters, L/κ in Equation 5.3 and α/L^2 in Equation 5.2. In the absence of the porous layer, only ξ, C_2, and p_i are to be determined through fitting.

As soon as the potential is stepped, the potential profile in the porous layer starts to change. This potential redistribution results from the charge distribution which generates the current. Most of the current flows to charge C_2 at early times. As the effective electrical resistance of the inner layer for small current is very large while compared with the solution ohmic resistance, the time constant of charging C_2 is approximately equal to $A_e R_3 C_2$ [17].

The estimation of the time constant of charging the porous layer is more complicated. Let L/κ be R_p and L^2/α be τ_p. Then the transient potential distribution, as a function of $\tilde{x}$ and $\tilde{t}$, is dependent on $A_e R_3/R_p$, τ_p, and $i(t)$. It may be noted that $\tau_p = R_p(aC_pL)$, where (aC_pL) is the capacitance density per unit area of the porous layer. If the inner layer is eliminated, the time constant of the potential transient can be determined according to the solutions for the transient heat conduction problems given in Reference [36]. Generally, the transient time increases as τ_p and $Bi(=A_e R_3/R_p)$. Particularly, in case of constant τ_p and R_p, a higher solution ohmic resistance results in a slower transient. However, due to the presence of the inner barrier layer, the transient time must be dependent on ξ and C_2 as well. In spite of this

complication, the initial guess of τ_p value for the current transient calculation is made based on the solutions in Reference [36].

Compared with both capacitive charging processes, pore filling causes the current to decay at a much lower rate. The potentiostatic growth of the inner barrier layer should obey the rate law given by Equation 1.1 when almost all of the potential drop occurs in the barrier layer. After a long time under potentiostatic control, the current decays to a value close to the corrosion current.

5.3 Comparison between Experimental and Modeling Results

5.3.1 Anodic Current Transients at -0.9 V after Prior Cathodic Charging

The pitting behavior of aluminum at -0.4 V is dependent on the amount of prior cathodic charge at -2.0 V. In order to investigate the cause of this dependence, Lin and Hebert measured the anodic current transients at -0.9 V after various periods of cathodic charge at -2.0 V. The current decays within 100 ms were mathematically considered as a summation of 3 or 4 exponential decays vs. time. Figure 5.1 gives the initial current decays within 10 ms. The current density i is plotted on a log scale in order to show the time constants of the exponential functions. The bottom three curves were the cases with prior cathodic charges less than 7.2 mC/cm^2, so no porous layer, Phase 2' in Figure 4.2, is present on the top of the inner layer. The top curve in the figure is the case with the porous layer due to its high prior cathodic charge.

For the calculations in the model, $\eta_O = 0$ was assumed since $i(0^-)$ is cathodic. Therefore, Equation 4.41 is used for the pore filling process. For the case of 60.2 mC/cm^2 cathodic charge, L was obtained from QCM results [17] and κ was calculated from the cathodic current transient and the corresponding porous layer thickness. The calculation details are given in Appendix A, in which $V_r + \phi_2(0^-) = -1.485$ V. Since $\phi_2(0^-) < 0$, V_r was therefore assumed to be -1.46 V in the calculations, which is close to -1.5 V according to Equation 4.36. The value of i_o^c in Equation 4.37 was obtained from $i(0^-)$ by applying $\phi_2(0^-)$ into Equation 4.32 with $b^+ = 10^3 \times \xi / B_a$. Since $\phi_2(t)$ changed from the negative value at $t = 0$ to a positive value

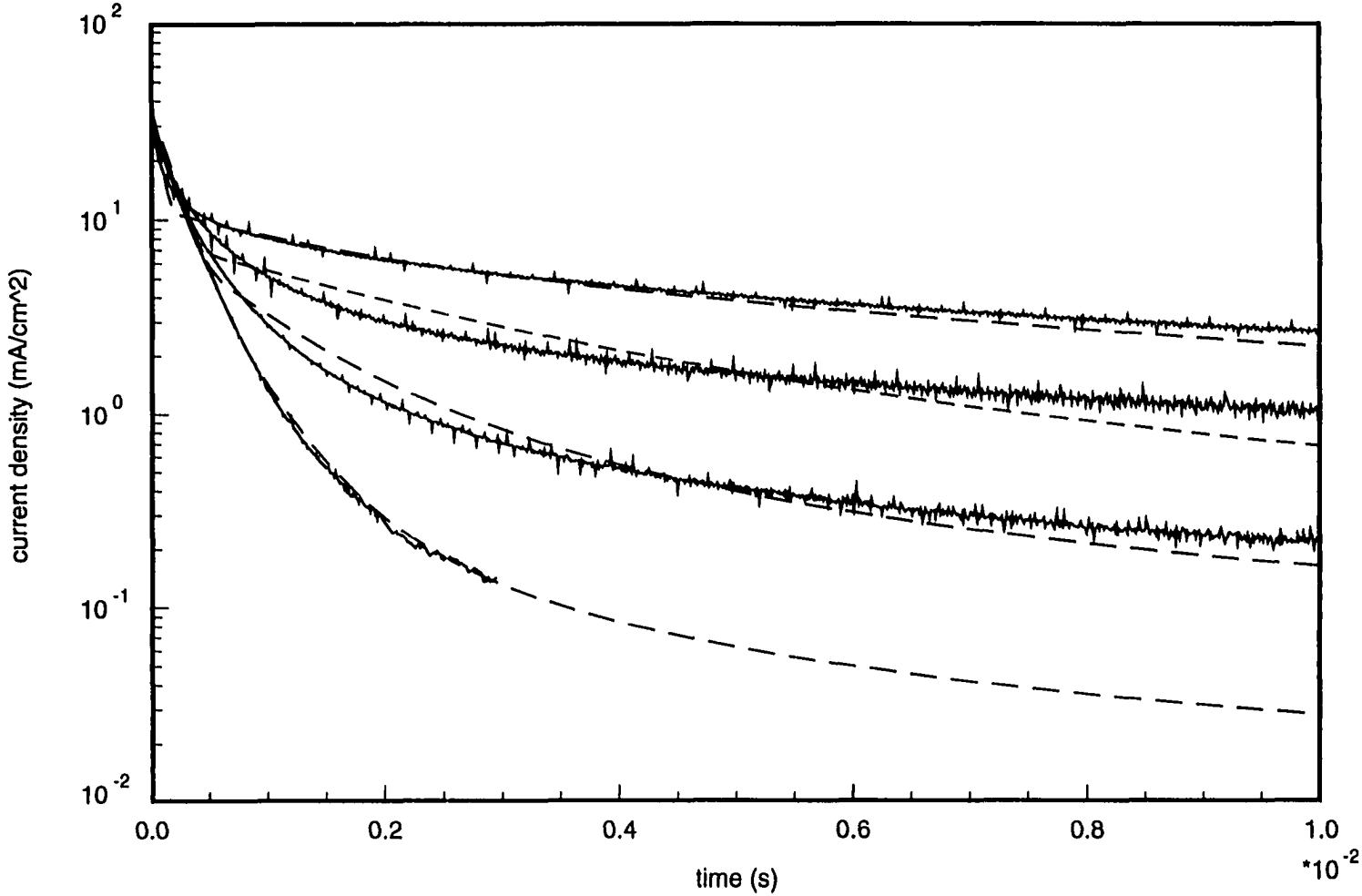

Figure 5.1 The anodic current transients at -0.9 V; the dashed curves are the calculation results and the solid curves are the experimental data. The solution was 0.1 N HCl. The cathodic charges for the solid curves from the top to the bottom are 60.2 mC/cm^2, 2.59 mC/cm^2, 0.65 mC/cm^2, and 0.002 mC/cm^2 respectively.

within an extremely short time (normally less than 30 μs) and during that time almost all current was capacitive current, the uncertainty of the cathodic current conduction rate law has a negligible effect on the calculation results. C_2 was estimated from the initial slopes in Figure 5.1 at $t = 0$ and $A_e R_3$. The initial linear portion of each curve in the figure represents the charging process of C_2. The initial values of ξ were estimated by using the current densities at the end of the C_2 charging process ($t = t_1$) according the following equation,

$$V_H - V_r = \frac{\xi(0)}{B_a} \ln \frac{i(t_1)}{i_{ao}} + i(0^-)R_p + i(t_1)A_e R_3. \tag{5.10}$$

Table 5.1 gives the parameters used in the calculations for the dashed curves in Figure 5.1. Q_c represents the cathodic charges at -2.0 V. For the case of $Q_c = 60.2\ mC/cm^2$, the potential distributions in the porous layer at various times are presented in Figure 5.2. According to the figure, the time constant of the porous-layer charging is about 2.5 ms. For comparison, based on $\tau_p = 2$ ms and $Bi = 10.66/25.17$, the time constant determined by the solutions in Reference [36] is 5.4 ms. The shorter time constant may result from the charging of C_2 which accelerates the charge redistribution in the porous layer.

Table 5.1 The parameters for the modeling results in Figure 5.1 and 5.4.

Q_c (mC/cm^2)	$i(0^-)$ (mA/cm^2)	$A_e R_3$ (Ω-cm^2)	C_2 ($\mu F/cm^2$)	$\xi(0)$ (Å)	L (Å)	$\kappa \times 10^8$ (Ω^{-1}-cm^{-1})	τ_p (ms)	p_i
0.002	-2.0	31.3	9.0	19.5				0.001
0.65	-1.75	28.2	9.0	16.6				0.006
2.59	-3.5	29.3	9.0	15.1				0.02
60.2	-4.7	25.2	5.0	13.0	26.5	2.5	5.0	0.05
24.0	-5.0	44.0	5.5	16.0	10.0	2.0	5.0	0.12

For a further test of the electrical model, the anodic potential stepped to from -2.0 V was varied (−0.9 V, −0.7 V, −0.3 V, and −0.1 V), and the calculated anodic current at 4 ms was plotted vs. the corrected anodic potential, as shown in Figure 5.3. The corrected anodic potential is obtained by subtracting η_O and $iA_e R_3$ from the applied potential. The dashed line in the figure was obtained from Figure 9 in Reference [11], which was the linear regression of the experimental current data. According to Figure 5.3, the plot generated by the electrical model agrees with the experimental plot very well. Both give the potential at $i = 0$ close to

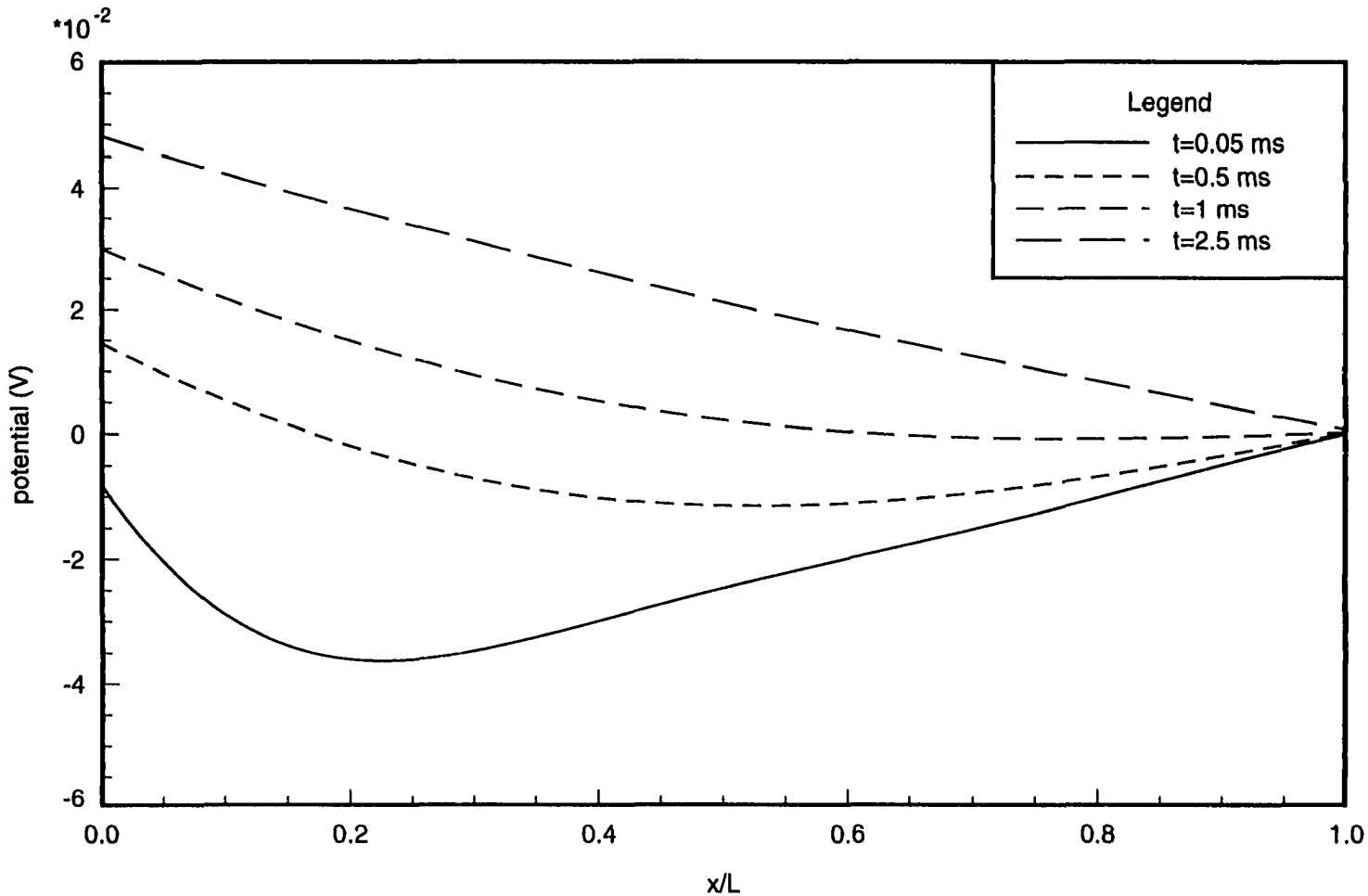

Figure 5.2 The calculated potential distributions in the porous layer at various times for the case of $Q_c = 60.2\ mC/cm^2$.

-1.3 V, instead of V_r. This phenomenon is caused by the presence of the inner barrier layer.

The interruption experiments described in Chapter 3 also provide current transient data at -0.9 V, which is shown in Figure 5.4 along with the modeling results. The related parameters are also included in Table 5.1. The porous layer resistance is estimated to be 5 Ω since $L = 10$ Å was obtained from QCM results given by Reference [11]. The experimental curve in Figure 5.4 is not the same as the top curve in Figure 5.1 because the solutions used in the experiments and $A_e R_3$'s are different. In case of cathodic charge more than about 20 mC/cm^2, the increase of the cathodic charge at -2.0 V only has a fairly minor effect on the anodic current transient [18]. Therefore, the difference between the two cathodic charges does not contribute to the difference between the two experimental results..

The long-time current decay at -0.9 V was modeled from 20 ms to 20 s without the consideration of any capacitive charging. In other words, the porous layer was considered as an ohmic resistor and the C_2 charging is neglected for $t > 20$ ms. The calculated current decayed only because of film growth. $\eta_O(t)$ could be included in the calculation since $i(t) > 0$ for $t > 20$ ms. The addition of $\eta_O(t)$ required the adjustment of V_r by $\eta_O(t = 20$ ms), namely $V_r = -1.58$ V. The calculation results at 20 ms shown in Figure 5.4 served as the initial conditions for the calculation of the long-time current decay. ξ is 19 Å at t=20 ms, which could be the thickness of the inner layer. At this time, the porosity for the calculation of the inner-layer growth was changed form p_i(=0.12) to p(=0.2) and Equation 4.39 substituted for Equation 4.41 for the pore filling process. Figure 5.5 and 5.6 show the current decays at -0.9 V within 1 s and 20 s. The change of $\eta_O(t)$ from $t = 20$ ms to $t = 20$ s is significant due to the dramatic change of $i(t)$. In contrast, $\eta_O(t)$ corresponding to $i(t)$ at $t < 20$ ms is about constant. Therefore, the assumption of $\eta_O(t) = 0$ at $t < 20$ ms is in fact equivalent to the assumption of $\eta_O(t)$ =const. with $V_r = -1.46 - \eta_O$. On the other hand, since pore filling changes L, R_p could be changing during the interruption. Fortunately, the electrical resistance of the inner layer for small anodic currents at $t < 20$ ms is so dominant that the accuracy of R_p is not critical.

On the basis of the modeling results shown in Table 5.1, the cathodic charging at -2.0 V results in the decrease of the electrically effective thickness, ξ, and the increase of porosity,

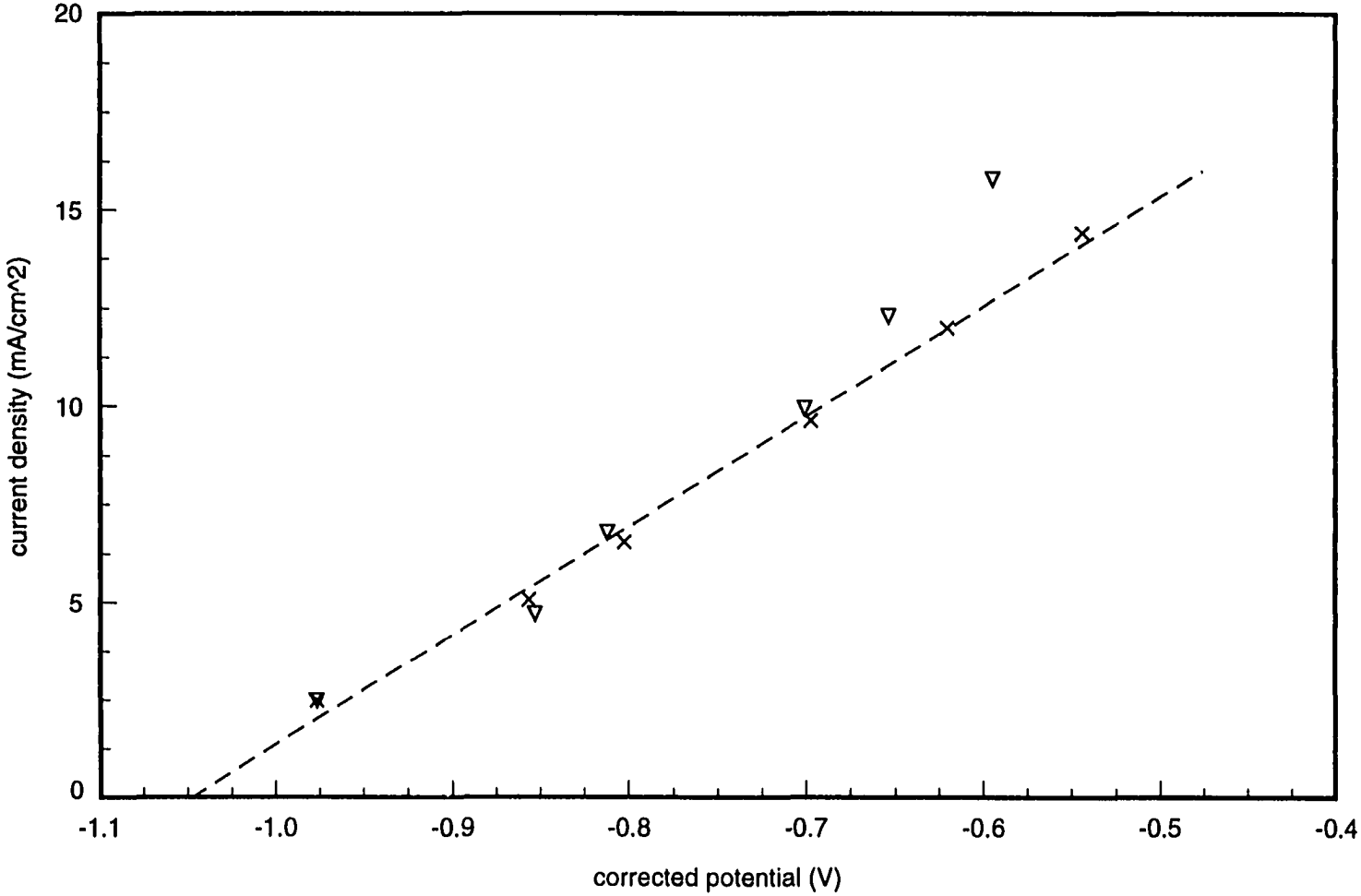

Figure 5.3 The calculated anodic current at 4 ms vs. the corrected potential (vs. $Ag/AgCl/4M\ KCl$). The corrected potentials were obtained by subtracting η_O and iA_eR_3 from the applied anodic potentials. The crosses are the calculated results and the solid line is their linear regression. The triangles are the experimental data in Figure 9 in Reference [8].

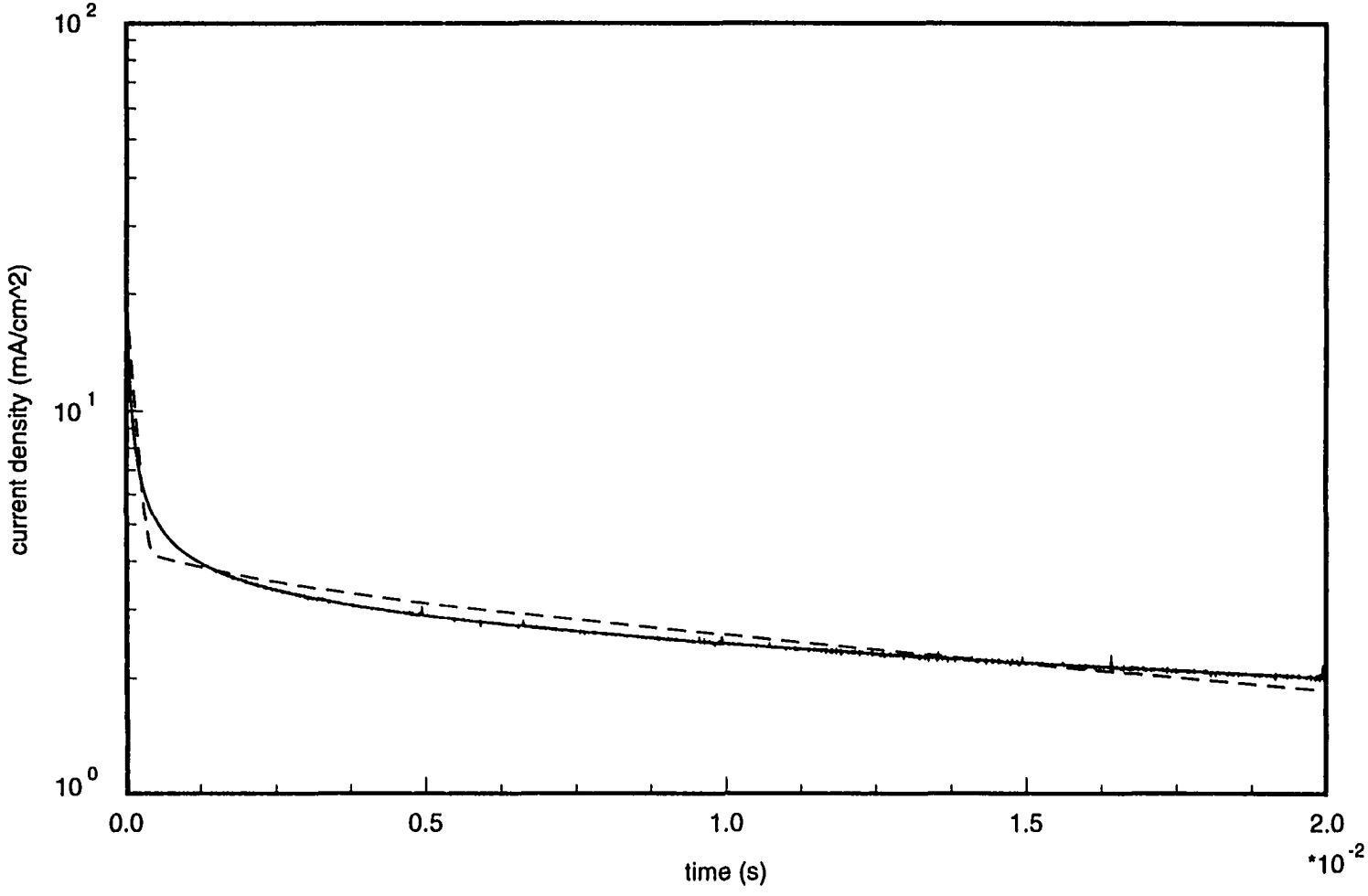

Figure 5.4 The anodic current transient at -0.9 V. The solid curve is the experimental data and the dashed curve is the calculation result. The solution was 0.1 M H_2SO4. The cathodic charge of -2.0 V was 24 mC/cm^2.

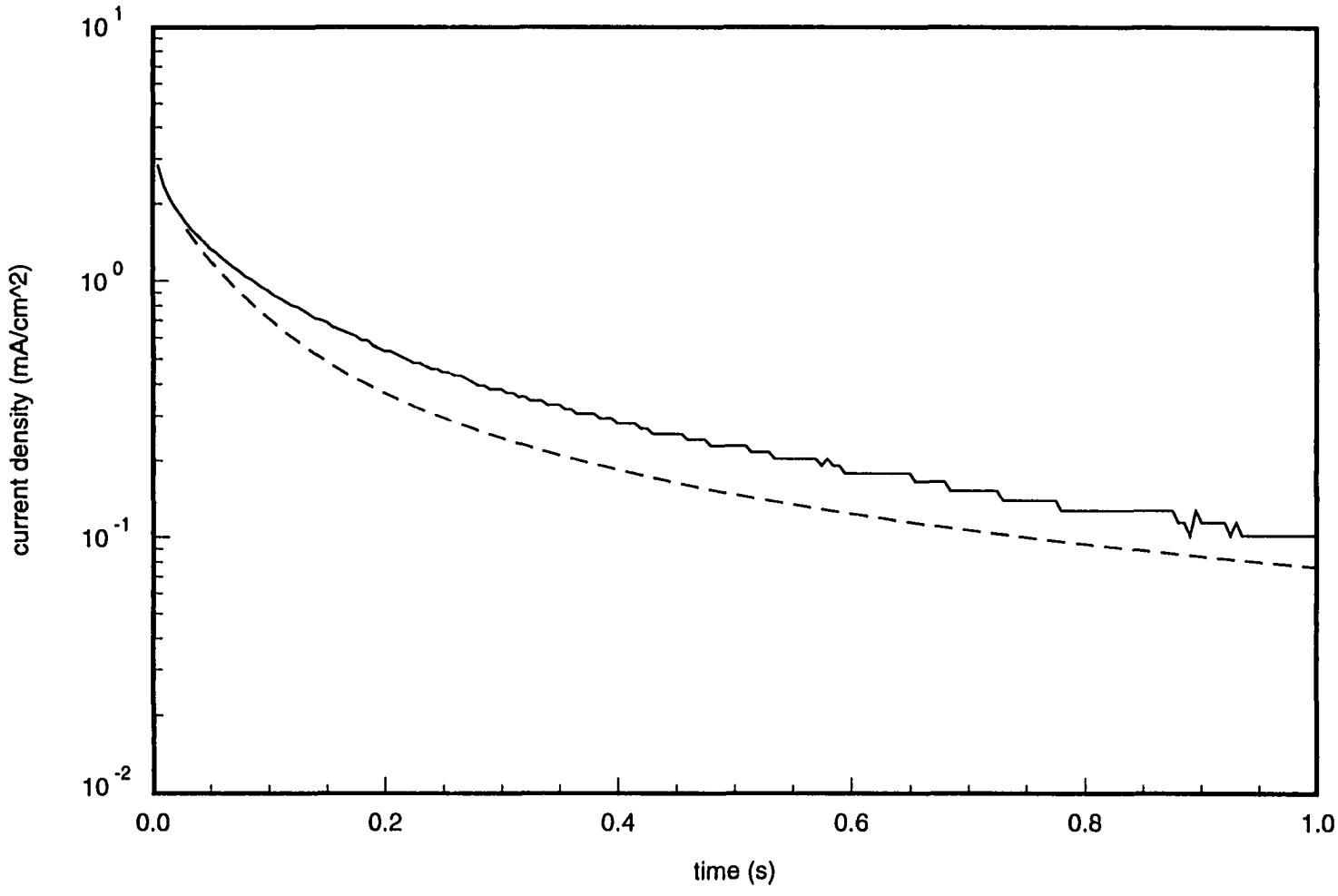

Figure 5.5 The anodic current transient of 1 s at -0.9 V; the dashed curve is the calculation result and the solid curve is the experimental data.

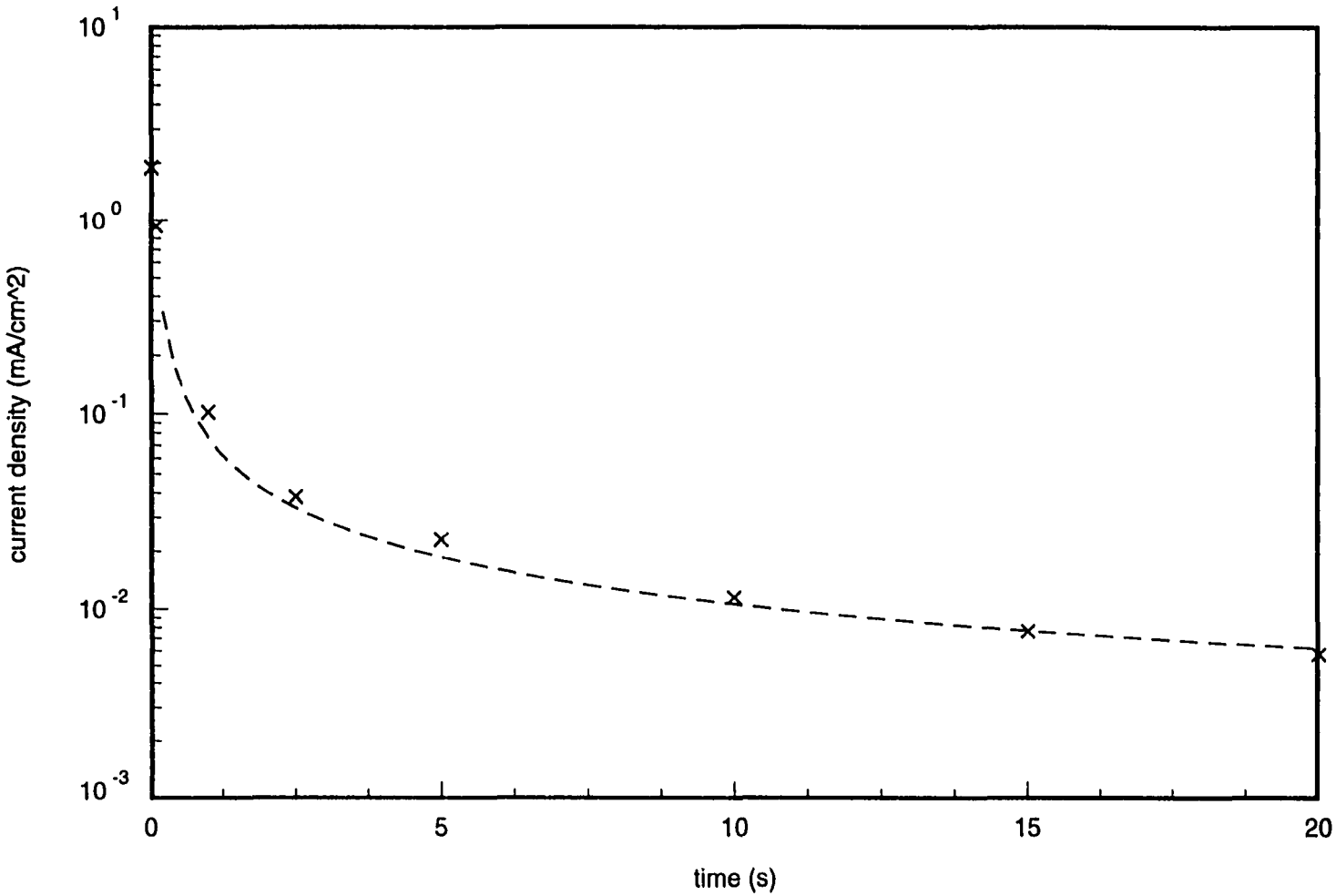

Figure 5.6 The anodic current transient of 20 s at -0.9 V; the dashed curve is the calculation result and the crosses are the experimental data.

p_i. Both changes are likely caused by film dissolution, which will be discussed further in the Discussion section.

For the case of $Q_c = 0.002 mC/cm^2$, ξ is 19.5 Å at $t = 0$ and increases rapidly to 25 Å within 4 ms. The rapid pore filling by film growth is due to the very very small porosity. 25 Å is possibly the thickness of the pretreated oxide film. According the XPS results [17], the original thickness of the air-formed oxide layer was 31 Å. After the 5 min pretreatment in 0.1 N HCl, the thickness became 24 Å based on the QCM results [18]. The consistency between the experimental and the modeling thicknesses for the pretreated oxide film is quite encouraging for the electrical model. For the case of $Q_c = 60.2\ mC/cm^2$ in 0.1 N HCl, ξ is 13 Å, which is 11 Å less than the original barrier layer thickness. As mentioned in the previous section, the oxide film pretreated in 5 wt% H_3PO_4 for 20 min is 28.4 Å thick. According to Table 5.1, ξ is 16 Å for the case of $Q_c = 24\ mC/cm^2$ in 0.1 M H_2SO_4. Hence, the electrical resistance loss due to the pore formation is equivalent to the electrical resistance of a 12.4 Å barrier layer. On the basis of the above two changes of ξ caused by cathodic charging, it may be concluded that the dissolution effect in 0.1 N HCl is almost the same as that in 0.1 M H_2SO_4.

In the calculation of the long time current decay at -0.9 V, p was substituted for p_i when ξ is equal to 17.86 Å although the pretreated oxide film prior to any cathodic charging is 28 Å. In fact, even though the structural model assumes that the porous layer appeared only when the film mass started to increase, it is possible that the porous layer not only grew into the solution phase but also into the inner layer. In other words, the interface between Phase 2 and 2' in Figure 4.2 may be retreating toward the metal phase during the cathodic charging process. If the expansion of the porous layer into the inner layer is true, then its thickness, L, is greater than what was observed by QCM.

5.3.2 Anodic Current Transients at -0.4 V after Interruptions at -0.9 V

The pitting accelerated by the prior cathodic charging is significantly attenuated by the interruption at -0.9 V. This motivated the interruption experiments (described in Chapter 3) whose results are presented in Figure 5.7. On the basis of the electrical model, R_p and the

initial value of ξ were calculated from the experimental current data by using the following equations;

$$(i^1 - i^2)(A_e R_3 + R_p) + (\eta_O^1 - \eta_O^2) + (\phi_2^1 - \phi_2^2) = -0.5, \tag{5.11}$$

$$i^2(A_e R_3 + R_p) + \eta_O^2 + \phi_2^2 = -0.13 - V_r, \tag{5.12}$$

where the superscript "1" represents the final condition of the interruption period and "2" represents the condition at -0.4 V right after both capacitive charging processes. V_r is still -1.58 V. Table 5.2 gives the calculated values of R_p and ξ. Interestingly, the long-time current decays modeled in the previous section are accompanied by different values of ξ. The comparison between the two results for ξ is presented in Figure 5.8. The two results for ξ are fairly consistent. As expected, the relation between modeled ξ and ln$t$ is linear. The modeling results are shown in Figure 5.7 and Table 5.2 gives the parameters used for the calculations of the modeling results. p is still 0.2.

The values of L and κ are uncertain, but fortunately only their ratio R_p (=L/κ) determined the current calculation results. However, the charge density parameter of the porous layer, aC_p, can be determined from τ_p only with the knowledge of L.

Table 5.2 The parameters for the modeling results in Figure 5.7.

int. time (s)	$i(0^-)$ (mA/cm^2)	$A_e R_3$ (Ω-cm^2)	$\xi(0)$ (Å)	R_p (Ω-cm^2)	C_2 ($\mu F/cm^2$)	τ_p (ms)
0.02	1.9	40.8	17.9	26.7	5.3	0.5
0.1	0.928	39.3	20.4	34.4	5.0	0.5
1.0	0.102	38.9	26.0	46.4	5.0	2.0
3.0	0.032	40.3	28.8	48.0	5.0	3.0
20.0	0.006	38.0	33.7	13.3	4.0	2.0

According to Table 5.2, R_p was changing during the interruption at -0.9 V. Since the ohmic potential drop in the porous layer is significant only if the anodic current is not too small, the accuracy of R_p calculated from Equation 5.11 is less certain when i^1 and i^2 are very small after a long interruption time. Fortunately, in case of large ξ, the anodic current is small, so the accuracy of R_p is not important for the calculated current.

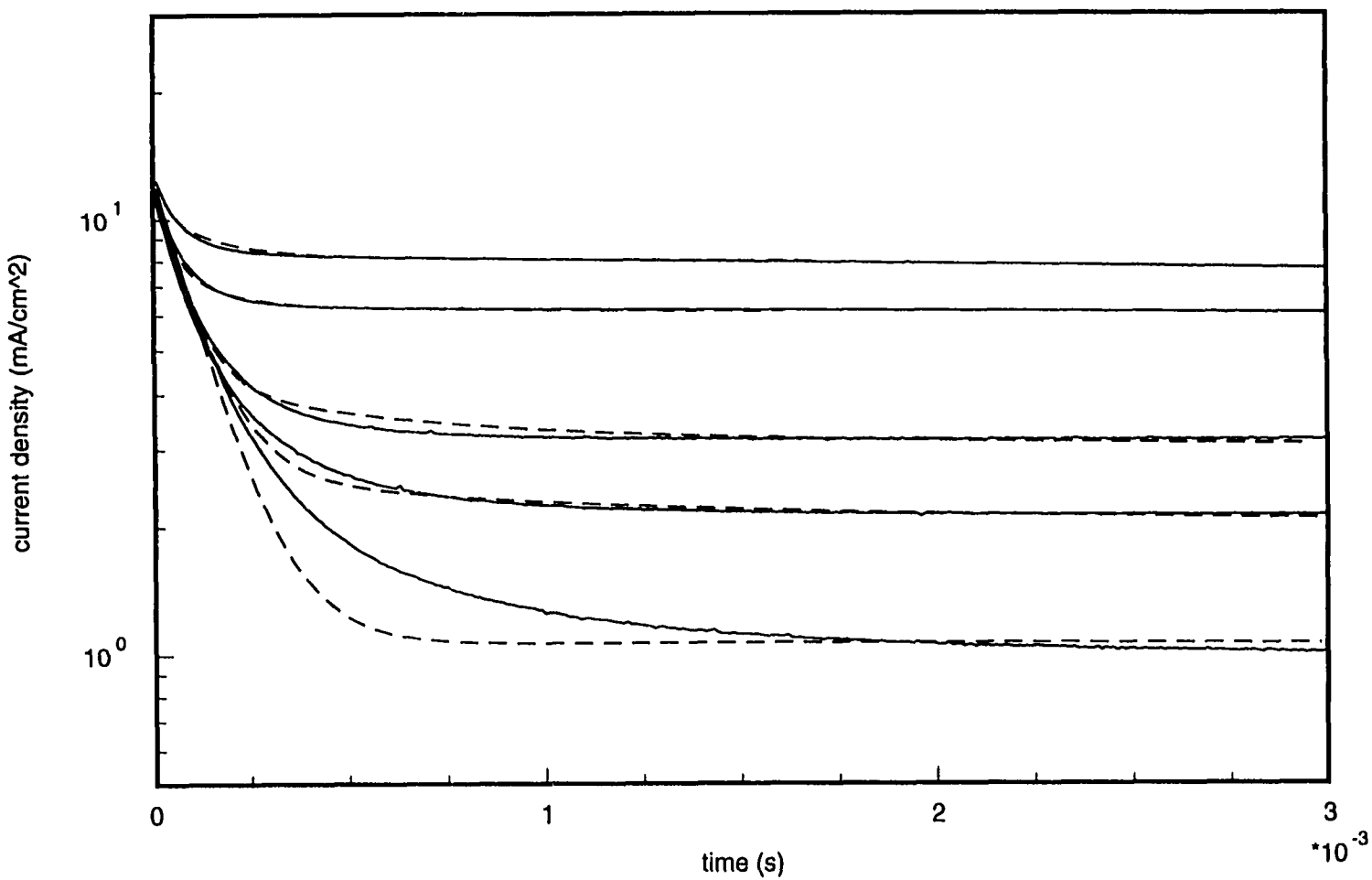

Figure 5.7 The anodic current transients at -0.4 V after interruptions at -0.9 V; the dashed curves are the calculation results and the solid curves are the experimental data. The interruption times for the solid curves from the top to the bottom are 0.02 s, 0.1 s, 1 s, 3 s and 20 s respectively.

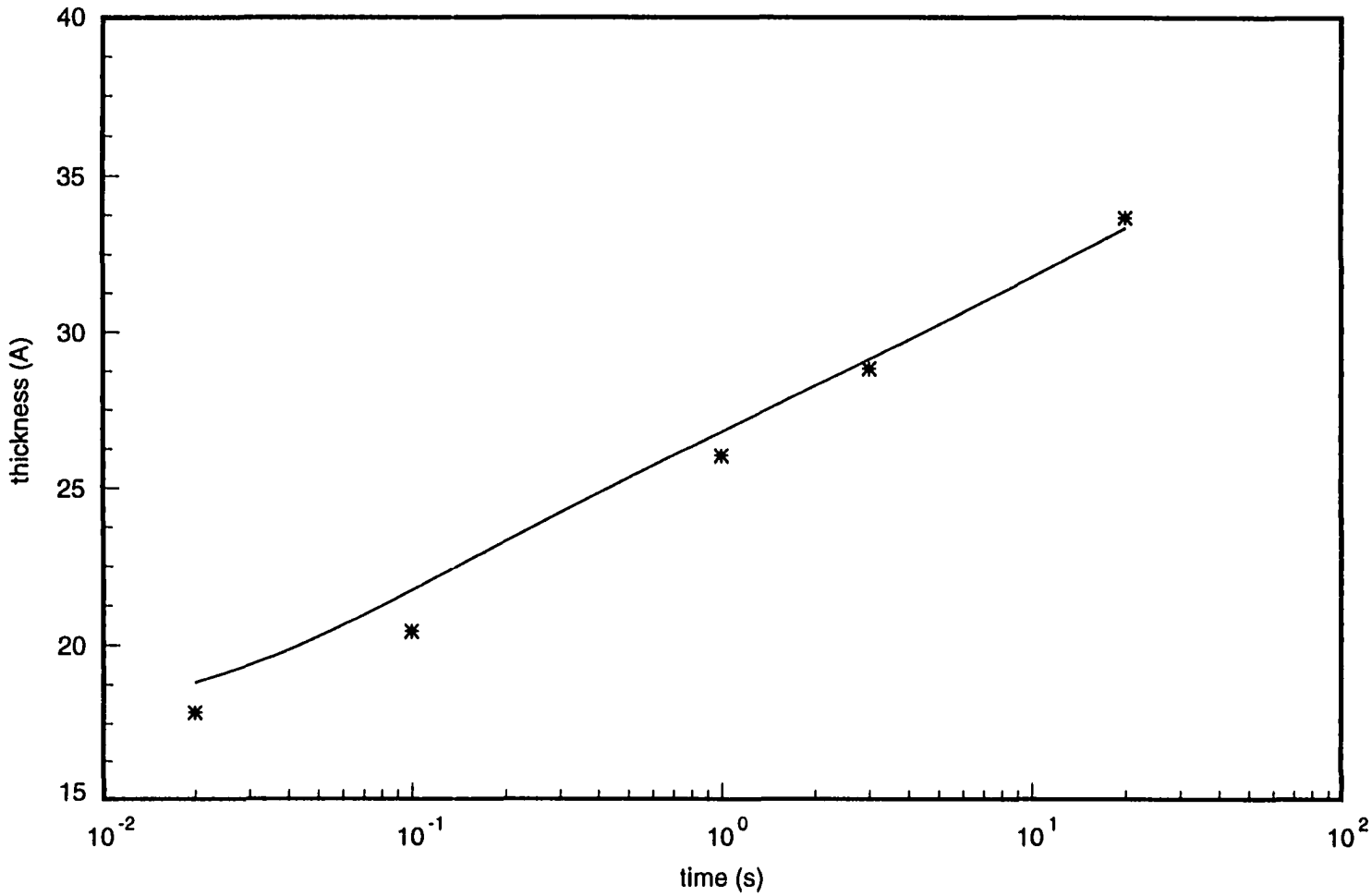

Figure 5.8 The electrically effective thickness of the inner layer, ξ, *vs.* time during the interruption period at -0.9 V. The solid line is the modeling result and the symbols were the calculated values from Equation 5.11 and 5.12.

5.3.3 The Analysis of Experimental Results

The anodic ion conduction rate of the pretreated oxide film on aluminum with no cathodic charge can be investigated by using the experimental data shown in Figure 3.4. In Figure 5.9, the stationary current at each applied potential (vs. $Ag/AgCl/4MKCl$) in Figure 3.4 was plotted on a log scale vs. the corrected potential, which is obtained by subtracting η_O and iA_eR_3 from the applied potential. In other words, the corrected potential here is equal to $(\phi_2 + V_r - 0.27)$ according to the electrical model. The linear relation between log i and the corrected potential indicates that the pretreated oxide films were high field conductors. Let the linear regression in the figure be expressed by

$$\log i = SV_a + I, \tag{5.13}$$

where V_a represents the corrected potential. According to Equation 4.31, $S = \frac{B_a}{\xi \ln 10}$ and $I = \log i_o - \frac{B_a(V_r - 0.27)}{\xi \ln 10}$. Since $S = 7.43$ and $B_a = 4.86 \times 10^{-6}\ V^{-1}cm^{-1}$, ξ is 28.4 Å. Also since $I = 5.8$ and $i_o^a = 9.8 \times 10^{-12} A/cm^2$, V_r was calculated to be -1.58 V, which is the same as the value of V_r used in the modeling calculation.

Similarly, after the 20 sec interruption at -0.9 V the stationary anodic currents, as shown in Figure 3.6, were plotted on a log scale vs. the corrected potential in Figure 5.10. The slope and the intercept of the linear regression are 6.64 and 3.82 respectively. Therefore, ξ is 31.8 Å and V_r is -1.51 V. It should be noted that the porous layer is assumed to be absent here. For the case of 20 sec interruption, ξ in Table 5.2 is 33.67 Å with $R_p = 13.33\ \Omega$. Since the two ξ values are very close to one another, R_p is more likely close to zero.

5.4 Discussion

On the basis of the modeling results shown in Table 5.1, a small period of the cathodic charging at -2.0 V ($Q_c < 3\ C/cm^2$) results in the abrupt decrease of the electrically effective thickness ξ from the initial thickness of 28 Å to 15-20 Å and the increase of the porosity p_i to 0.02. The QCM frequency of Lin and Hebert [11] shows a 2-3 Hz increase during the early period of cathodic charging, which is equivalent to only about 2 Å of uniform film dissolution.

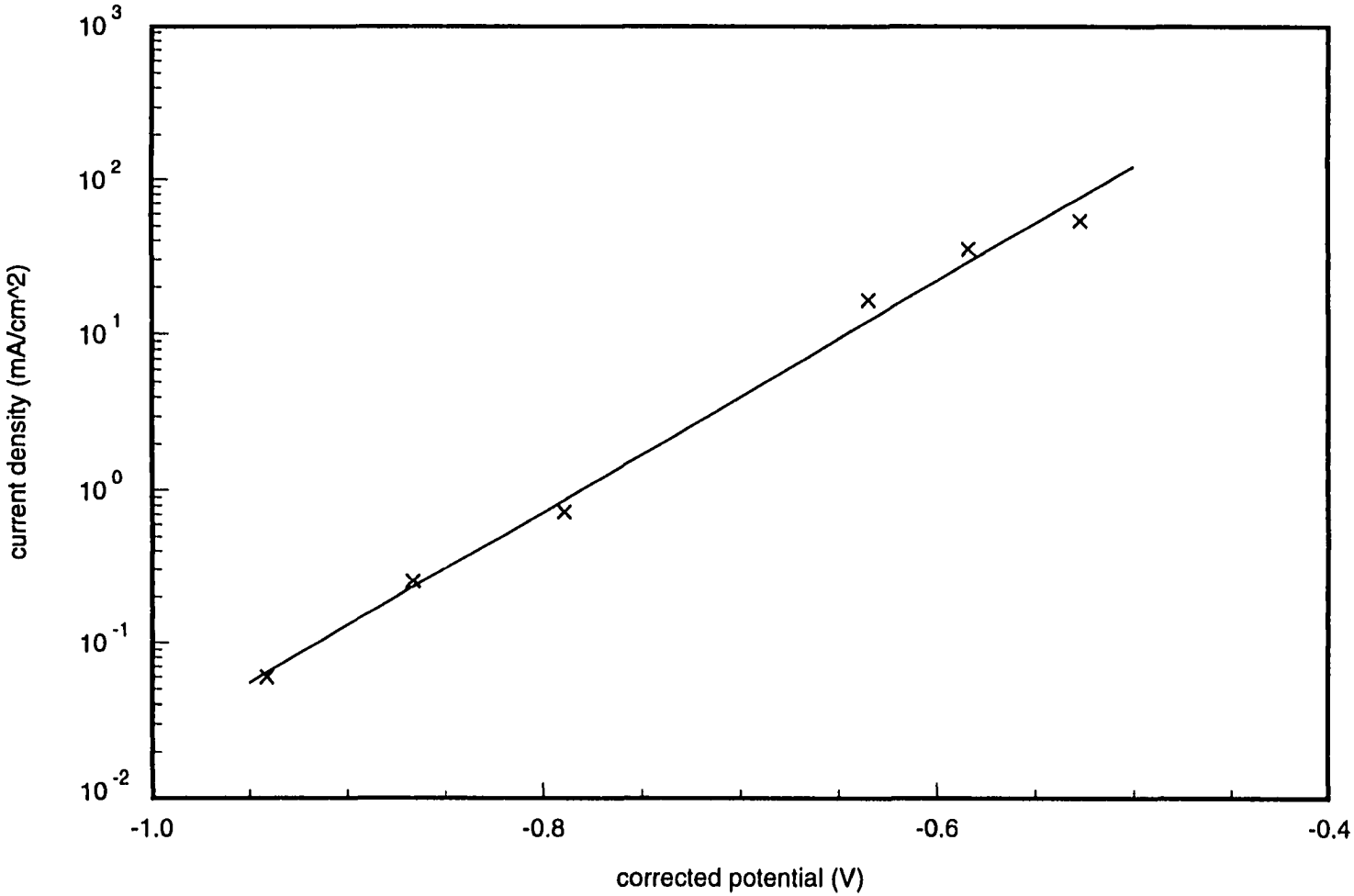

Figure 5.9 The stationary anodic currents of the aluminum electrodes right after the pretreatment vs. the corresponding corrected potentials (vs. $Ag/AgCl/4M\ KCl$). The corrected potentials were obtained by subtracting η_O and iA_eR_3 from the applied anodic potentials.

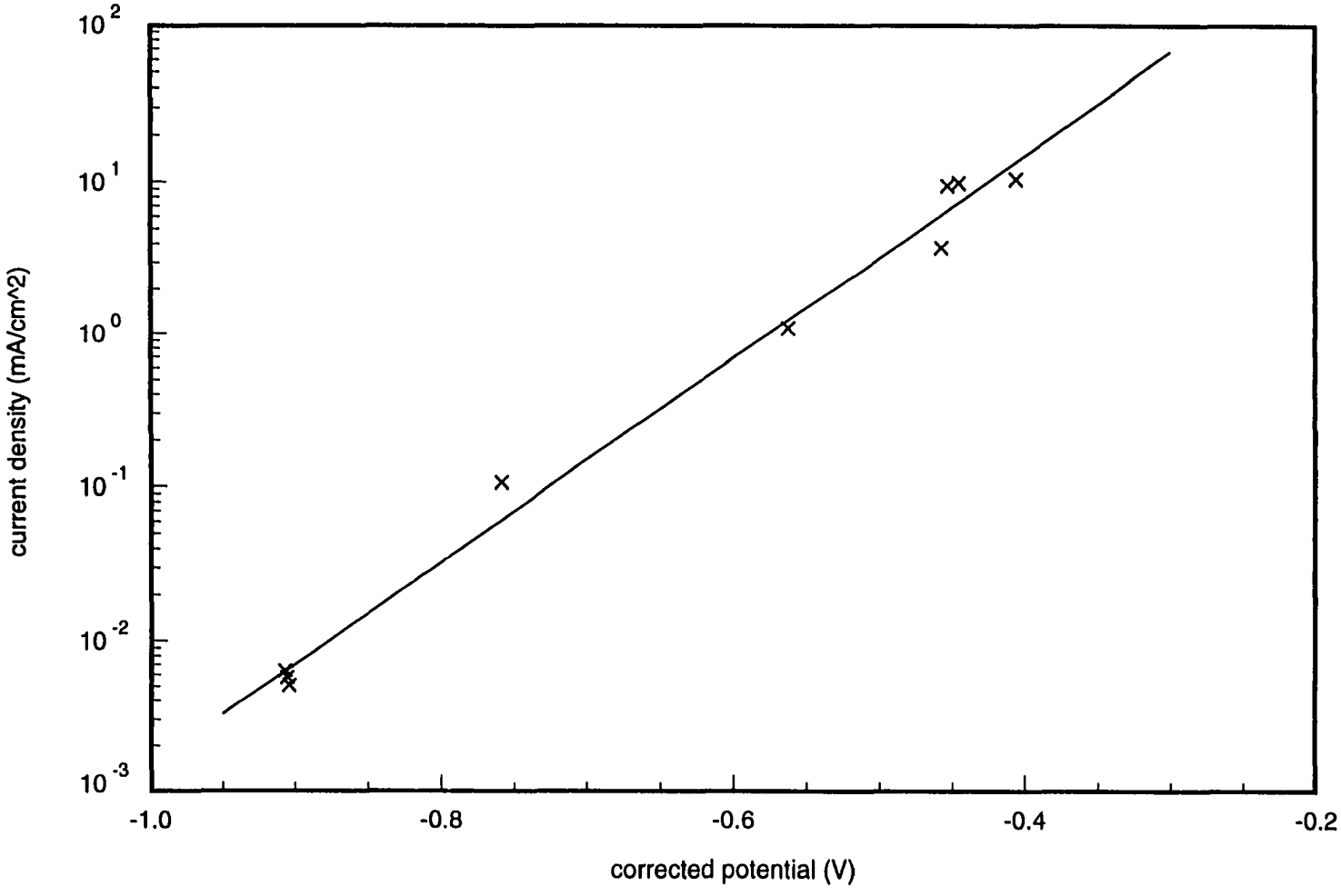

Figure 5.10 The stationary anodic currents of the aluminum electrodes after 20 sec interruptions vs. the corresponding corrected potentials (vs. $Ag/AgCl/4M\ KCl$). The corrected potentials were obtained by subtracting η_O and iA_eR_3 from the applied anodic potentials.

Therefore, the decrease of ξ can be associated with the formation of pores in the original oxide film due to non-uniform dissolution. Since the aqueous pathways in the pores are much more conductive than the oxide, the resistance of the porous layer can be much smaller than that of the inner barrier layer. The electrically effective layer thickness of the film would be mainly the inner pore-free part. The formation of pores in the oxide film by cathodic charging is also suggested by Hassel and Lohrengel [47] based on similar anodic current transients as those in Figure 5.1.

The dissolution rate of an oxide film was favored during cathodic polarization according to Equation 1.6. When the sum of the potential drops across the oxide and the film/solution interface was kept constant, the dissolution rate of the oxide film was limited in part by the rate of ionic conduction through the oxide. In case that the film thickness was irregular microscopically along the metal surface, at the thinner parts of the oxide film, faster dissolution occurred because of a higher potential drop across the oxide/solution interface and a higher electric field in the oxide. The rate of local dissolution was enhanced further as the local film was being thinned, leading to the formation of pores. On the other hand, when the applied potential was switched to an anodic value, film growth became dominant, and its rate is also limited by the transport through the film. Consequently, film grew at the pore bottoms where the film was locally thinner.

Although the localized dissolution at the thinner parts of the film explains pore formation, the initial rate of film dissolution at the pore bottoms seems to be too high. In the case of 0.002 mC/cm^2 cathodic charge in Table 5.1, the pore penetrated into the oxide film by 8 Å in only about 2 ms. The current density due to this rate of film dissolution would be 0.7 A/cm^2, which cannot be rationalized by the oxygen ion transfer kinetic expression (Equation 1.6) alone. Hence, pores might be located at pre-existing defective regions of the film or might be formed by mechanical cracking [52].

As the pore filling during early anodic current transients leads to the increase of inner pore-free layer thickness, a smaller porosity allows the film to recover its resistance in a shorter time. For instance, the anodic current with the smallest Q_c (and p) in Figure 5.1 decayed to

0.1 mA/cm^2 in only about 3 ms due to the rapid growth of the inner pore-free layer back to its initial thickness. As the porosity increased with Q_c, the inner pore-free layer stayed thin for a longer time as a result of slower pore filling. If the inner pore-free layer is the barrier for pitting, the time that the inner barrier stays thin during the subsequent anodic polarization above the pitting potential could be critical for pit formation. According to the pitting current transients given by Lin and Hebert [11], a minimum cathodic charge between 0.01 ad 0.13 mC/cm^2 was required to accelerate pitting during subsequent anodic polarization. On the other hand, when the cathodic charge exceeded 7 mC/cm^2, an additional porous layer began to grow. Under subsequent anodic polarization, the presence of this additional porous layer delayed the rise of pitting current and therefore pit nucleation, because its resistance was significant when the current was on the order of mA/cm^2.

The structural parameters of the additional porous layer can be roughly estimated from the value of τ_p, L and κ given in Table 5.1 and p equal to 0.2. If the pores are straight, cylindrical and perpendicular to the metal/film interface, the specific area a of the porous layer is $2\pi rn$, where r the pore radius and n is the number of pores per unit area. Accordingly, the porosity p is $\pi r^2 n$. When Q_c was 60.2 mC/cm^2, the capacitance density of the porous layer, aC_p $(= \tau_p \kappa / L^2)$, is 1770 F/cm^3. No C_p could be found specifically for aluminum oxide, so an order of magnitude estimate of 100 $\mu F/cm^2$ [9][50] is used to calculate the pore radius of the porous layer, r $(= 2p/a)$, to be 2.3 Å and n to be 1.2×10^{14} cm^{-2}. The distance between two neighboring pores is then 0.9 nm, which is somewhat smaller than the estimates of microcrystallite sizes within hydrated anodic alumina films, ranging from 1 to 10 nm [51].

When the metal was polarized above the pitting potential after cathodic charging in 0.1 M HCl, the number of pits was on the order of 10^6 $pits/cm^2$, much smaller than the number of pores in the oxide calculated above. The difference can be explained by the distribution of pore length along the metal surface and the model merely determined its average. Possibly, a small fraction of the pores penetrated all the way through the oxide and exposed metal surface to chloride ions and therefore pits formed at these sites. Takahashi *et al.* [48][49] found experimental evidence that such exposure of the metal at a pore bottom can occur during

cathodic polarization.

5.5 Conclusions

A mathematical model was formulated to investigate the structural change of the oxide film on aluminum due to cathodic charging. The model assumed a duplex film structure composed of a barrier layer on the metal side and a porous layer on the solution side. The processes formulated in the model include all relevant capacitive processes, conduction in both layers of the oxide film, and the interfacial reactions, such as pore filling by oxide growth at potential higher than the open circuit potential. The model was fit with the anodic current transients during subsequent anodic polarization to determine the structural parameters in the model. The relation between structural changes of the oxide film caused by cathodic charging and the rate of pitting corrosion when the metal was brought to an anodic potential soon after cathodic charging is of interest in this work.

The model produced the experimental anodic current decays from mA/cm^2 range to $\mu A/cm^2$ range over several orders of magnitude variation of time (ms to s). The structural parameters show the decrease of the inner pore-free layer thickness from initial 28 Å to 15-20 Å and the increase of the porosity of the outer porous layer to 0.02 as the results of cathodic charging ($Q_c < 7\ mC/cm^2$). These changes were considered as the growth of pores in the outer portion of the initial film. The pores may be produced by the non-uniform electrochemical dissolution of the oxide during cathodic current flow; however the rate of pore penetration is too high to be expected from the kinetics of this reaction. A small fraction of pores may penetrate entirely through the oxide film and expose metal for pitting in chloride solutions.

PART II

A DEFECT CLUSTER MODEL FOR IONIC CONDUCTION IN AMORPHOUS ANODIC OXIDE FILMS

6 IONIC CONDUCTION IN ANODIC OXIDE FILMS: A REVIEW

6.1 Introduction

This survey is concerned with the amorphous anodic oxide films on the so-called "valve metals", of which aluminum and tantalum are two common examples. Niobium, tungsten, molybdenum and zirconium are also members of the valve metal group. With these metals, an oxide film is always present, which separates the reactants, oxygen and metal. The continued growth of oxide films can be produced by setting up an electrostatic field in the oxide which causes the migration of metal and/or oxygen ions through the film. Therefore, if the oxide-coated metal is an anode of an electrolytic cell with a solution that does not dissolve the oxide, applying current can result to the formation of anodic oxide films. The overall kinetics of the growth process have been described in Chapter 1.

This chapter describes previous work relevant to the development of the model for ionic conduction. This includes electrical measurements of current/electric field relations and tracer and marker experiments revealing the details of ion transport. Also, some mechanistic ideas about ion conduction are discussed.

6.2 Experiments

6.2.1 Electrical Measurements

The field strength in the oxide required to produce ionic current densities in the normal experimental range are typically in the range of 10^6 to 10^7 V/cm. During steady-state film growth, the relation $i = A\exp(BE)$ represents the dependence of anodic current i on electric field E to a first approximation. Table 6.1 lists some of A and B values of metal oxides. Note

that the values of B of different amorphous anodic oxides are very similar.

In addition to the steady-state high field ionic conduction, the transient response of the electric field or current upon variation of either the applied current or voltage is of interest. Galvanostatic transients have been observed for aluminum and tantalum [61]. The experimental technique was to change abruptly the applied current density after establishment of steady-state conditions, and follow the potential as a function of time. A remarkable feature of these transients is that the decay of field strength toward its new steady-state value is not a function of time, but of charge passed per unit area. Also, potentiostatic transients showing this charge dependence have been observed for tantalum, aluminum and niobium [61].

Table 6.1 The values of parameter A and B.

oxide	A, Amp/cm^2	B, cm/V	Reference
Al_2O_3	$10^{-19} - 10^{-20}$	$4.7\times10^{-6} - 5.0\times10^{-6}$	Videm [39]
Ta_2O_5	10^{-18}	4.8×10^{-6}	Young [70]
Nb_2O_5	$10^{-15} - 10^{-18}$	6.4×10^{-6}	Young [71]
WO_3	10^{-15}	5.2×10^{-6}	Young [53]

6.2.2 Marker and Tracer Experiments

The transport mechanism responsible for oxide film growth on metals has been investigated by the use of inert markers and tracers. Marker experiments provide information on how much of the current is carried by metal ions migrating toward the oxide/electrolyte interface and how much by oxygen migrating in the opposite direction [67][68]. Tracer experiments observe the atomic order after the growth of the anodic oxide film.

Markers in markers experiments are chemically inert and immobile atoms buried in oxide, which identify reference planes in the oxide parallel to the two interfaces [67]. In these experiments, a thin preformed oxide is labeled initially with the ion-implanted markers deposited on its surface, and then reanodized to an increased thickness. The ideal marker atoms should be immobile and should not significantly alter the properties of the oxide in which they are embedded. Hence they should be chemically inert, uncharged, large in size, and present in trace amount. The final marker position and distribution determined by various techniques

provides a measure of the oxide growth relative to the reference planes.

For instance, Davies *et al.* [72] chose radioactive inert gas Xe^{125} as the marker to study anodic oxidation of Al and Ta. The depth of the Xe^{125} markers in the growing oxide film was measured using a β-spectrometer. The results show that the Xe^{125} remains very close to the surface under these anodizing conditions, and therefore, that the fresh oxide layers are being formed at the metal/film interface. Oxygen being the mobile species is hence suggested. In the later marker experiments of Davies *et al.* [73], the amount of metal dissolving in the electrolyte was measured to determine the transference numbers of metal and oxygen. The transference number of the ion is the fraction of the ionic current carried by the ion.

Other techniques which have been used to determine the position and distribution of markers include: (a) α spectroscopy for Rn^{222} [74]; (b) precision sectioning combined with β spectroscopy for Br^{82}, Kr^{85}, and Rb^{86} [77]; (c) Rutherford backscattering for Ar, Kr, Xe, etc. [75][76]; (d) cross-sectional transmission electron microscopy of the oxide containing Xe [78]. Instead of implanting foreign atoms, Shimizu *et al.* [78] developed thin disc-shaped Al_2O_3 crystals in the amorphous barrier oxide layers by anodic oxidation of thermally oxidized aluminum, and used them as markers. Ultramicrotomed sections of the barrier oxide were then examined in a transmission electron microscope to determine the position of the crystals. The cation transport numbers obtained using this method agree with the numbers obtained by the usual implanted xenon marker method. Table 6.2 summarizes the data of the cation transference number t_M for the growth of anodic oxide films on valve metals, which shows that both species are mobile during oxide film growth on Al, Nb, Ta, V, and W. The transference numbers of metal ions seem to increase slightly with current density according to Davies *el al.* [73] for the cases of Ta_2O_5, Nb_2O_5 and WO_3. For the case of aluminum oxide, the dependence of t_M on current density varies with the electrolyte used for anodization. Comparable transference numbers are only found in non-crystalline materials. Zirconium oxide (Zr_2O) formed anodically on Zr is crystalline, and t_M is close to zero [66].

Marker experiments can only determine how much of the new oxide is being formed by metal and/or oxygen migration. Oxygen or metal itself needs to be tagged in order to observe

Table 6.2 The transference numbers in metal oxides determined by marker experiments.

Oxide	t_M	Reference
Al_2O_3	0.44	Shimizu *el al.* [78]
	0.45	Shimizu and Kobayashi [79]
	0.40	Brown and Mackintosh [69]
	0.33-0.72	Davies *et al.* [73]
Ta_2O_5	0.28	Whitton [77]
	0.24	Pringle [67]
	0.26-0.31	Davies *et al.* [73]
V_2O_5	0.28	Mackintosh and Plattner [76]
Nb_2O_5	0.22-0.33	Davies *et al.* [73]
WO_3	0.30-0.37	Davies *et al.* [73]
Z_rO_2	0.00-0.05	Davies *et al.* [73]

how the individual atoms migrate. In most tracer experiments, O^{18} was incorporated by anodizing in $H_2^{18}O$ electrolyte and then detected by means of nuclear reactions.

Amsel and Samuel [65] applied tracer methods to determine the order of the atoms in Al_2O_3 films during anodic oxidation. For oxygen tracing, aluminum foils were oxidized first in an electrolyte containing O^{18} in both solute and solvent, and then were further oxidized in an electrolyte containing natural oxygen. The distribution of O^{18} and O^{16} in the oxide film was found to follow the sequence of oxidation. In other words, O^{18} was located between the original oxide layer and the O^{16} oxide layer formed by later anodic oxidation. These results indicated that oxygen atoms move by vacancy diffusion or exchange-interstitial diffusion as described in the next section.

In order to observe the concentration gradient of O^{18} in the anodic film, Pringle [68] used a sectioning technique to locate the tracer species. The sectioning technique basically thinned the anodic oxide on tantalum in such a way as to leave a series of steps in the oxide surface. The resolution of O^{18} concentration detected by mean of nuclear reactions was improved by about an order of magnitude. On anodizing tantalum first in O^{16} electrolyte and then in O^{18} electrolyte, the O^{18} incorporated last was found outside the O^{16} layer incorporated first. There was also a small mixing between O^{18} and O^{16} at the boundary. Thus, oxygen conduction occurs by substitutional diffusion in this system as well.

6.3 Theoretical Models

Many earlier models of the ionic conduction in solids rely on the use of a defect model originally developed by Frenkel [58]. This model emphasizes that ionic conduction occurs through the transport of mobile charged point defects in a crystal lattice. Although anodic oxide films on valve metals, such as Al, Ta, Nb and W, have an amorphous structure instead of a crystalline structure [66], the point defect model is appropriate as a first approximation. This section will first review the point defect model. It will be explained below that point defect model fails to predict comparable transference numbers for cations and anions, as is characteristic of amorphous oxide films (Table 6.2). Hence, some recent mechanisms have ascribed comparable transference numbers to a correlated motion of cations and anions through the oxide. These models will be described in more detail in this section.

6.3.1 The Transport of Point Defects

Point defects with which we are concerned here are atomic imperfections in crystalline solids. *Vacancies* and *interstitials* are two major types of atomic imperfection [63]. *Vacancies* are unoccupied sites which in the ideal ordered crystal should be occupied. *Interstitials* are atoms occupying sites which in the ideal ordered crystals should not be occupied. The atomic imperfections often occur in ionized form. The transport of metal and oxygen may be achieved by the movements of atomic imperfections in several ways [65]. One possible mechanism is interstitial transport, namely the diffusion of interstitial atoms through the lattice in interstitial positions. Another possible mechanism is substitutional transport such as vacancy diffusion and "exchange interstitial" diffusion. Vacancy diffusion takes place as a lattice atom jumps into an adjacent vacancy position. In the case of "exchange interstitial" transport, a moving interstitial atom hits a lattice atom at rest and takes its place in a substitutional position, the process being repeated by the atom initially at rest. Interstitial transport reverses the initial order of the atoms but the other two types of transport conserve it.

Current can be conducted by the jump of charged defects through an oxide film. Since the current-field relation does not follow Ohm's law, Verwey first proposed a high-field mechanism

for the migration of cationic species through the film [59]. Note that the mechanism is based on the idea that interstitial metal ions are the mobile entity. However, the same mechanism is applied in the literature to describe the movement of any type of defect. The mechanism is based on the potential-distance diagram shown in Figure 6.1. The equilibrium sites are located where the energy is minimum. The interstitial ions each sitting in an equilibrium site are crudely considered as vibrating in simple harmonic motion with a frequency ν. In order to jump from one equilibrium site to another, an ion must overcome an energy barrier with a magnitude of W shown in Figure 6.1.

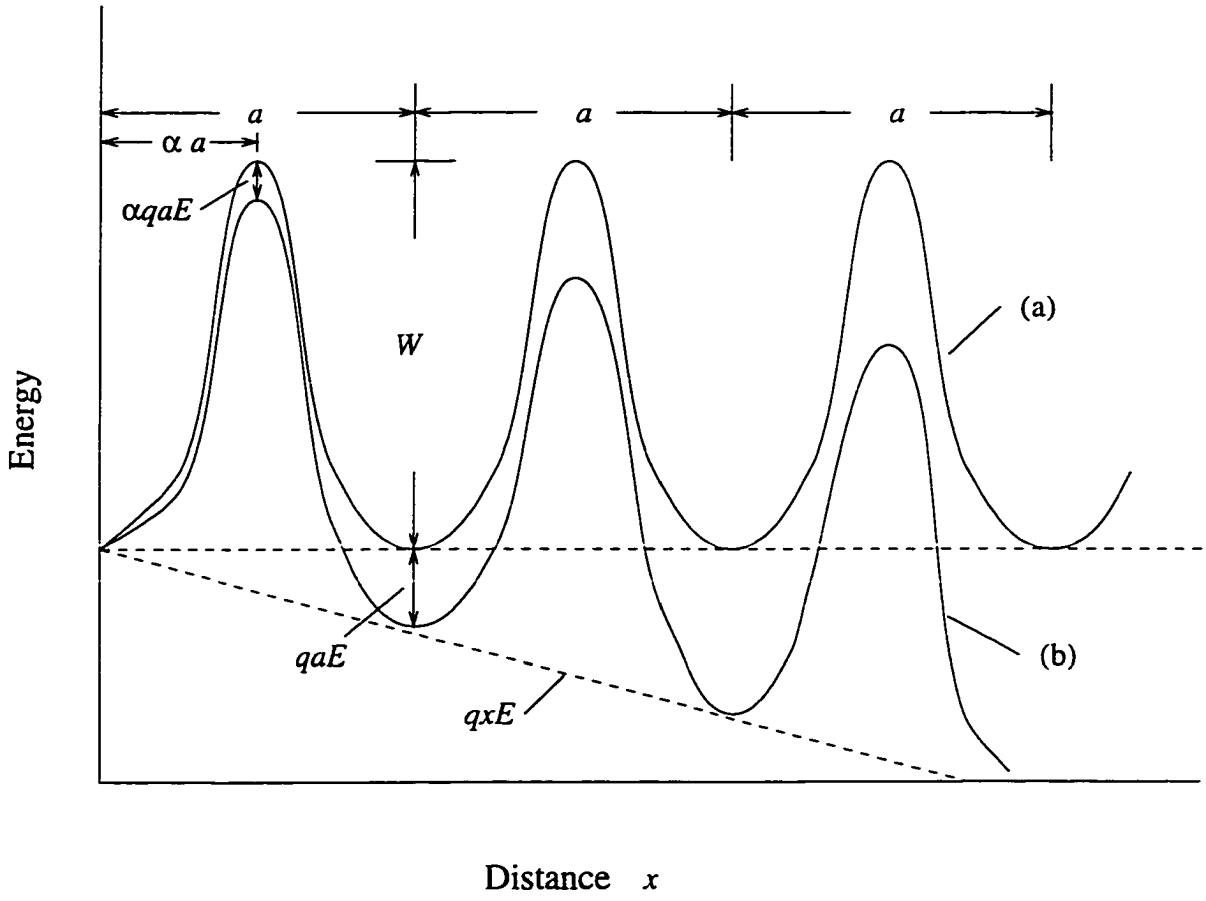

Figure 6.1 Energy of migrating ions vs. distance with (b) and without (a) an applied field.

In the absence of a field, the frequency of an ion jump varies exponentially with W and can be written as $\nu\exp(-\frac{W}{kT})$. The field E is assumed to reduce the height of the barrier from W to $(W - \alpha aqE)$ for ions moving with the field and to increase the barrier for ions moving against the field from W to $(W + (1 - \alpha)aqE)$. a is the jump distance and α corresponds to a "transfer coefficient" which describes the position of the barrier between two neighboring equilibrium sites. q is the ionic charge. Let the concentration of the mobile ions be c. The flux of ions is then written as

$$N = ca\nu[\exp(-\frac{W - \alpha aqE}{kT}) - \exp(-\frac{W + (1 - \alpha)aqE}{kT})]. \tag{6.1}$$

With the electric field of the order of $10^6 - 10^7$ V/cm, only one of the exponential terms in the above equation is important. For example, in case that the ions carry positive charge, the first term will dominate. The current density i $(= N_A qN)$ is therefore written as

$$i = N_A qca\nu\exp(-\frac{W}{kT})\exp(\frac{\alpha aqE}{kT}) = i_0\exp(\frac{\alpha aqE}{kT}). \tag{6.2}$$

N_A is the Avogadro constant. This equation gives the current density as a function of the field strength in the form of $i = A\exp(BE)$ with $A = i_0$ and $B = \frac{\alpha aq}{kT}$. This current-field relation is widely observed experimentally during the growth of oxide films as described in Section 6.2.1.

As will be discussed later in this chapter, the concentrations of various defects differ from each other dramatically with a small difference in the formation energy of the defect. Also, a small difference of the activation energy for the jump, W, leads a large difference in the mobilities. The term αaq is expected to be different between point defects with various charge and jump distances. With the consideration of these three factors, it is unavoidable that the charge flux by one kind of point defect will dominate the ionic conduction and the charge fluxes by the other kinds of point defects are simply negligible. Thus, the point defect model predicts that within experimental precision the transference number for cations or anions should be 0 or 1. However, the transport numbers for cations and anions are always found to be of the same order of magnitude. Therefore, ionic conduction in the amorphous oxides cannot be modeled as independent transport of point defects.

6.3.2 Liquid Region Mechanism

Because comparable transport numbers in oxides cannot be explained with a model of point defects, Mott [66] suggested the following model, valid only for non-crystalline oxides:

> ...it is suggested that in an oxide we may consider an activation energy W_0 sufficient to bring, say, $n = 20$ atoms to a state in which their vibrations are sufficient for them to act as liquid and, for a time, of order 10^{-12} s, in which they are in this condition, both ions could have moved under the influence of the field, giving comparable transport numbers.

This concept is called the liquid region mechanism in this chapter. This mechanism, as stated above, is qualitative. However, if developed into a quantitative model, this mechanism might possibly explain comparable transference numbers.

6.3.3 The Migration of Network Defects

Network defects were first proposed by Dignam [60] within the framework of the random-network model of the vitreous state proposed by Zachariasen [62] for covalent materials. Figure 6.2 shows the steps in the formation and the migration of network defects for B_2O_3. A pair of network defects can be imagined to form by the rupture of one of the metal-oxygen bonds as shown in Figure 6.2(a), followed by shifting oxygen partner 1 from metal 1 to metal 2 as shown from Figure 6.2(a) to Figure 6.2(b). The net result would be a stoichiometric excess of one half an oxygen in the immediate vicinity of oxygen 2 and one-third of a metal ion in that of metal 1. The ionized form of the defects should be strongly favored since vitreous oxides have fairly high dielectric constants. Hence, the bond between metal atom and oxygen is broken in such a manner that the metal atom loses an electron to the oxygen. Further partner exchange can lead to the migration of the anionic and/or cationic defects. The migration of an anionic defect is illustrated in Figure 6.2(c). The region passed through by a network defect will not return precisely to its original structure. In contrast, a given region of the crystal passed through

by a point defect will return precisely to its original structure even though the motion of the defect causes a disturbance in the lattice in the vicinity of the defect.

Ion transport by the migration of network defects appears to preserve the order in both metal and oxygen subnetworks. If anodically formed vitreous metal-oxide films grow by the motion of network defects, then all of the metal newly incorporated into the film will appear in the oxide next to the metal/oxide interface, and all the oxygen newly incorporated will appear next to the oxide/electrolyte interface. The motion of either cationic or anionic defects involves a cooperative motion of both metal and oxygen species in the vicinity of the defect. The transference number predicted by the model should then be between 0 and 1. The electric field would modify the activation energy for the migration of the mobile network defect as well as the enthalpy of formation of the network defect pair, and the high-field ionic conduction behavior might then be derived from this model.

The migration of covalent network defects is a qualitative model for the ionic conduction in vitreous solids. In fact, whether the network model for covalent materials can be applied for the amorphous oxides is doubtful because the oxides on valve metals are ionic materials.

6.3.4 Microscopic Nonsimultaneous Place Exchange

Fromhold [57] pictured a correlated motion of cations and anions by a microscopic nonsimultaneous place-exchange mechanism. Figure 6.3 shows the time evolution of a sequence of correlated place-exchange events in an oxide layer in Fromhold's place-exchange model. First, a cation exchanges position with an adsorbed oxygen as shown from (a) to (b). The formation of a single place-exchanged pair (hopon) requires a free energy increase. However, the second exchange shown in (c) leads to no free energy change of the system. After the initial place exchange between a cation and an adsorbed oxygen, a local excess charge appears, which would constitute the defect referred to as a *hopon*. The activation energy of a place-exchange event inside the lattice, W_H, can be lowered by the electric field, E, in the forward direction as

$$W^{(f)} = W_H - q_H E a, \tag{6.3}$$

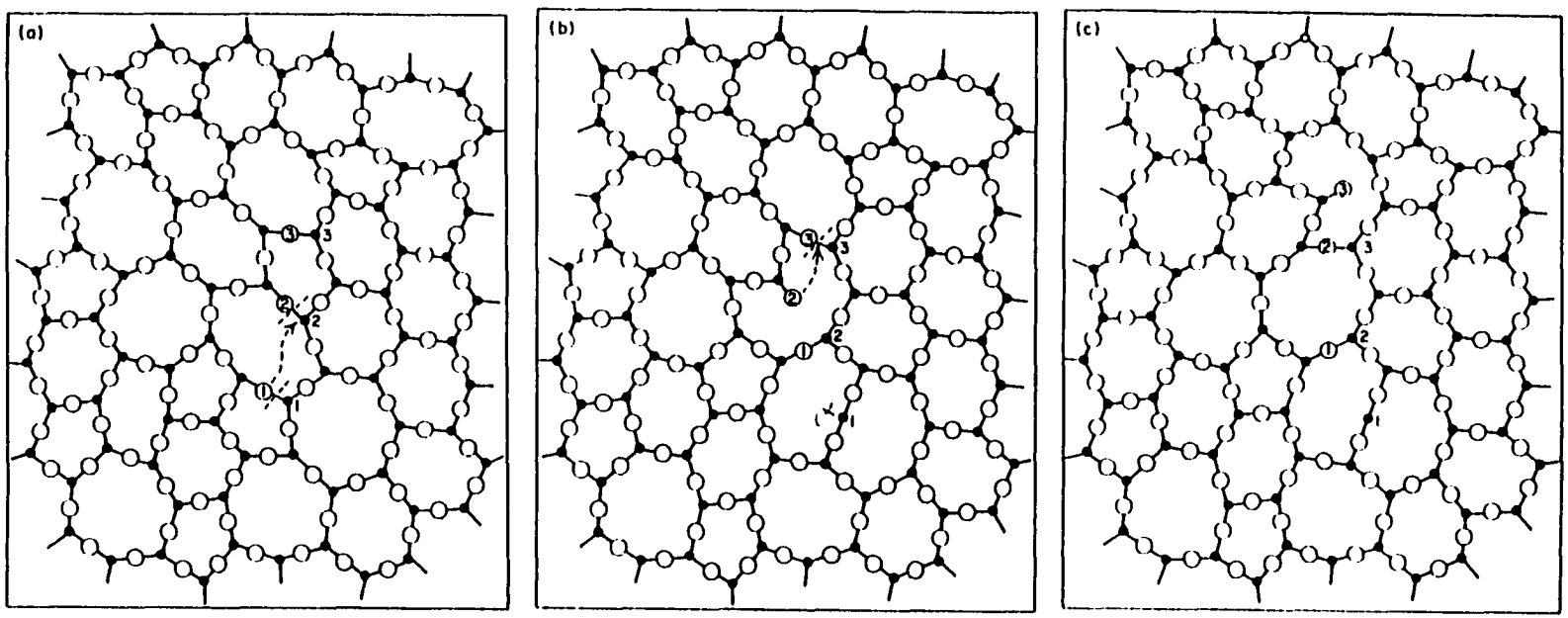

Figure 6.2 The sketch of the formation and migration of network defects given in Reference [60]. Metal atoms are shown as solid circles and oxygen atoms by open circles.

where q_H is the charge of the hopon and a is one half of one atomic distance. The activation energy for the reverse motion of a hopon is thus

$$W^{(r)} = W_H + q_H E a. \tag{6.4}$$

The activation energy expressions given by the above two equations are similar to the activation energy expressions for the movement of a vacancy or an interstitial in the point defect model. High field conduction can therefore be derived from this model as well.

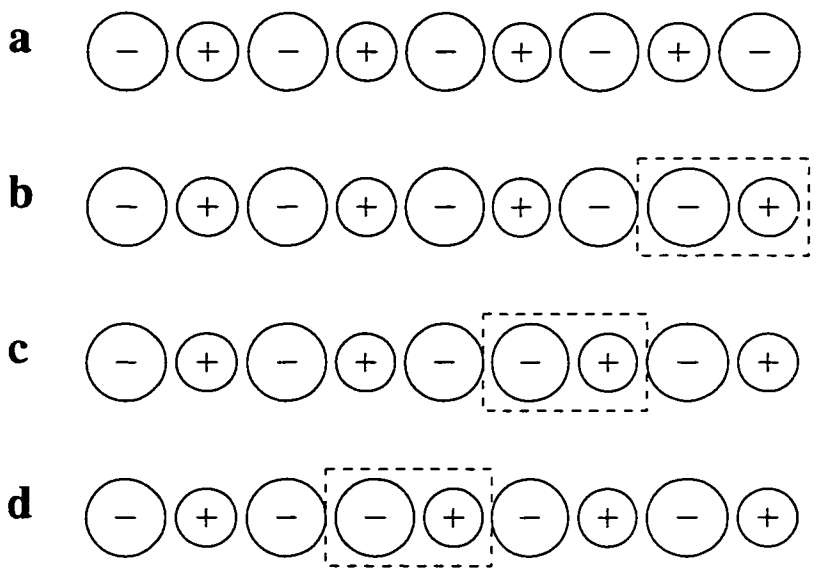

Figure 6.3 Sequential nonsimultaneous place-exchange events [57]. (a) is before place exchange. (b) is after the first place-exchange event. (c) and (d) are after the second and the third place exchange respectively.

Hopons may be generated at the metal/oxide interface as well. One cannot deduce the source interface for place exchange by an examination of the order within the ion arrays of the formed oxide. The transference numbers experimentally determined by measurements of the relative quantities of oxide formed at the two interfaces are given by the following two equations.

$$t_a = \frac{|z_a|}{|z_a| + |z_c|} \tag{6.5}$$

$$t_c = \frac{|z_c|}{|z_a| + |z_c|} \tag{6.6}$$

The place exchange event may involve more than two ions. For example, the rotation of the stoichiometric unit MO_p ($p = |z_c/z_a|$) may constitute the mode of hopon transport. In this case, equal volumes of oxide would be formed at the two interfaces. On the other hand, Fromhold suggested the correlated motion of two place exchanges through the oxide layer in a two-dimensional system since it is energetically favorable. More details are available in Reference [57]. The estimation of the formation energy of the hopon and W_H was not carried out to support the model.

Mott [66] commented that Fromhold's place change is possible only in a non-crystalline material and likely includes many more than the two ions involved. The concept of place exchange involving many ions driven by an electric field is perhaps identical with the polarization of an ionic liquid by the electric field.

6.4 The Concentrations of Point Defects in Aluminum Oxide

Point defects in ionic solids can be generated thermally within a solid or through kinetic reactions at its surface. This section investigates the concentrations of point defects formed within aluminum oxide based on their formation energies. Aluminum oxide was chosen as an example because the energies of point defects in α-alumina have been calculated by Catlow and James [80]. As will be shown soon, because of the low concentrations, few point defects are expected to be present within the oxide. Therefore, it is suggested that the point defects for ionic conduction are generated at the metal/oxide interface or at the oxide/solution interface and then migrate through the oxide.

In principle, various possible types of point defects are present at the same time in an ionic solid. The concentrations of the point defects are directly related to the thermodynamic equilibria between various point defects, and the thermodynamic equilibria between the solid compound and neighboring phases [64]. When the inter-phase reaction is not important, the formation energies of the point defects will govern the their concentrations.

Let us assume that aluminum oxide has four basic kinds of point defects: aluminum vacancy, aluminum interstitial, oxygen vacancy, and oxygen interstitial. The stoichiometric formation

of aluminum and oxygen vacancies in aluminum oxide can written as

$$0 \rightleftharpoons 2V_{Al}^{-3} + 3V_O^{+2}, \quad K_V = [V_{Al}^{-3}]^2[V_O^{+2}]^3. \tag{6.7}$$

V denotes a vacancy and Y_X denotes an X site occupied by Y. K denotes an equilibrium constant. The charges are associated with the point defects since space charge appears with the presence of the point defects. Aluminum and oxygen interstitials in aluminum oxide can be produced by

$$Al_2O_3 \rightleftharpoons 2Al_I^{+3} + 3O_I^{-2}, \quad K_I = [Al_I^{+3}]^2[O_I^{-2}]^3. \tag{6.8}$$

I denotes an interstitial. A lattice ion can be misplaced to form a vacancy and an interstitial, namely

$$Al_{Al} \rightleftharpoons V_{Al}^{-3} + I_{Al}^{+3}, \quad K_{Al} = [V_{Al}^{-3}][I_{Al}^{+3}], \tag{6.9}$$

$$O_O \rightleftharpoons V_O^{+2} + I_O^{-2}, \quad K_O = [V_O^{+2}][I_O^{-2}]. \tag{6.10}$$

Since $2Al_{Al} + 3O_O = Al_2O_3$, only three of the above four equilibria are independent. However, if the oxide is isolated and the point defects are generated only by lattice ions leaving their lattice positions, the interstitial concentration is equal to the vacancy concentration and only two of the above equilibria are required for the determination of the point defect concentrations.

The equilibrium concentrations of the point defects are related by the equilibrium constants. The equilibrium constants can be written as

$$K = \exp(-\frac{\Delta G^\circ}{kT}) = \exp(\frac{\Delta S^\circ}{kT})\exp(-\frac{\Delta H^\circ}{kT}), \tag{6.11}$$

in which ΔG°, ΔH°, and ΔS° are respectively the standard free energy, the enthalpy and the entropy of the reaction. The enthalpies of the above reactions can be calculated from the formation energies of the point defects. There has been considerable success in the calculation of defect energies in ionic oxides based on the Mott-Littleton method.

Basically, the Mott-Littleton method computes the formation energy of a point defect by modeling the interionic potential. The vacancy formation energy is that required to remove a

lattice ion to infinity while the remaining lattice relaxes to equilibrium. Likewise, the formation energy of an interstitial is that required to bring an ion from infinity to an interstitial site with a corresponding relaxation of the surrounding lattice. Catlow and James [80] have computed the formation energies of the point defects in α-alumina based on the Mott-Littleton method. Since no calculation has been performed for amorphous alumina, the calculation results for α-alumina were applied in the calculation of the enthalpies of the above reactions. As a result, the enthalpy of Reaction 6.7 is 23.52 eV, that of Reaction 6.8 is 26.67 eV, that of Reaction 6.9 is 12.9 eV, and that of Reaction 6.10 is 8.12 eV. The entropies of these reactions are not available and will be assumed negligible. This assumption is suggested by the fact that the S/k term was found negligible compared with the H/kT term for the formations of various point defects in many ionic compounds [64]. By using the rate constants calculated from the enthalpies of the reactions, one obtains the following relations between the defect concentrations at 298 K.

$$\log K_V = 2\log[V_{Al}^{-3}] + 3\log[V_O^{+2}] = -398 \tag{6.12}$$

$$\log K_I = 2\log[Al_I^{+3}] + 3\log[O_I^{-2}] = -451 \tag{6.13}$$

$$\log K_{Al} = \log[V_{Al}^{-3}] + \log[Al_I^{+3}] = -219 \tag{6.14}$$

$$\log K_O = \log[V_O^{+2}] + \log[O_I^{-2}] = -137 \tag{6.15}$$

In case that the point defects are formed only by lattice ions leaving their lattice positions, $\log[V_O^{+2}] = \log[V_I^{-2}] = -69$ according to Equation 6.14 and $\log[V_{Al}^{-3}] = \log[Al_I^{+3}] = -110$ according to Equation 6.15. The concentrations have the unit of *mole/liter*. These are considered as the intrinsic defect concentrations. By substituting these two results into Equation 6.12 and 6.13, one can see that consistency between these relations is fair.

With the given magnitudes of these concentrations, the concentrations of point defects formed by thermal motion of the oxide ions are considered negligible. The formation energies of the point defects in the other anodic oxides on valve metals are not available, so similar calculation cannot be performed. Their intrinsic defect concentrations may be low as well. Therefore, it is suggested that for the ionic conduction by point defects, point defects have to be generated at either the metal/oxide interface or the oxide/solution interface.

7 A DEFECT CLUSTER MODEL FOR IONIC CONDUCTION IN AMORPHOUS ANODIC OXIDE FILMS

7.1. Introduction

Models for ionic conduction based on independent hopping of point defects do not yield comparable fluxes of both metal and oxygen ions under an external field. Therefore, the concept of a polarized conductive region surrounding each hopping oxygen vacancy is introduced into the model of ionic conduction. In this model it will be seen that metal ion transport occurs as a byproduct of vacancy diffusion.

Transport by oxygen vacancies is proposed in the model based on the experimental observations of Amsel *et. al.* [65] and Pringle [68]. Vacancy transport is considered to be the rate limiting step. The atomic packing of the oxides is considered as a close packing of oxygen ions with metal ions located in some of the interstitial sites between oxygen ions. In the amorphous oxide, conductive regions for metal ion migration are located where oxygen ions are locally farther apart, so metal ions can migrate through the oxygen lattice with a lower activation energy. Such a conductive region is considered to be created by the relaxation of the oxygen ions surrounding the oxygen vacancy. The metal ions within this conductive region migrate under the electric field until the conductive region is electrically polarized. A mathematical model is developed for the overall ionic conduction across the oxide based on the hopping of oxygen vacancies and the polarization of the conductive regions surrounding each oxygen vacancy.

7.2 The Vacancy-Centered Cluster

In general, a conductive region is assumed located where the gap between oxygen ions is spacious enough for metal ions to pass through without overlap between the metal ion and the oxygen ions forming the gap. Any such overlap would lead to a repulsion force preventing the passing metal ion from moving further. The presence of conductive regions then depend on the distribution of O-O distance in the oxide. In Appendix C, the distribution of O-O distance in the oxide is simulated based on the free volume model [81]. The simulation results indicate that the variation in the O-O distance across the oxide is very small. Hence, no "easy path" across the oxide exists for the migration of metal ions, due to the presence of higher O-O distances. On the other hand, the relaxation of the oxygen ions surrounding an oxygen vacancy can increase the distances between oxygen ions, so a conductive region can be created. This section proposes the existence of a conductive region surrounding each oxygen vacancy in which metal ions can migrate with little activation energy.

The absence of an oxygen ion from an oxygen lattice site leads to a net charge of $2e$ associated with metal ions coordinating the vacant site. To a first approximation, the electric field around the vacancy can be viewed as arising from a point charge at the vacancy. The electric field due to the point charge is a function of the distance from the charge, r, as

$$E_r = \frac{2e}{4\pi\epsilon r^2}. \tag{7.1}$$

For the first layer of oxygen ions surrounding the vacancy, r is about 3 Å and E_r is as much as 32 MV/cm with $\epsilon = 10\epsilon_0$. Similarly, for the second layer r is 6 Å and E_r decreases to 8 MV/cm. Hence one may expect that the oxygen ions surrounding the vacancy move towards the vacancy due to the electric field. Since the electric field at the second layer of oxygen ions is much smaller than that at the first layer, the displacement of the second layer is much smaller. The idea that ions close to a charged defect center are displaced away from perfect lattice position to a greater extent than remote ions was also suggested by Grimes and Catlow [84] based on their defect simulations. They stated that the attenuation in displacive forces is more rapid than $1/r^2$, due to electrostatic screening by the first oxygen layer. If the first

layer of oxygen ions are considered as a unit, say a sphere, the displacement of the oxygen ions towards the vacancy will shrink the sphere and open up a gap between the sphere and its surroundings. As the gap is widened, the activation energy for metal ions to migrate in the gap is reduced significantly. Then, the gap can be considered as a conductive spherical shell, and metal ions will polarize the shell under an electric field.

The purpose of this discussion is to suggest that due to the inward displacements of the oxygen ions surrounding an oxygen vacancy, a conductive gap for metal ion migration is formed around the vacancy. The region affected by the relaxation around a vacancy includes the 12 nearest oxygen neighbors of a vacancy and the conductive gap surrounding the 12 oxygen ions and will be called the vacancy-centered cluster from now on. Figure 7.1 illustrates a vacancy-centered cluster formed by the displacements of 6 oxygen ions surrounding a vacancy site (A or B) on a hexagonal close-packed layer of oxygen ions. An oxygen vacancy is enclosed by three more oxygen ions on top of the layer and three more at bottom of the layer. The conductive gap moves with the vacancy as the vacancy hops from site to site, as shown in Figure 7.1. In a crystalline material, the oxygen ions are closest packed, so the extensive displacement of oxygen ions toward the vacancy is impossible and the easy path for metal ion migration cannot be created.

7.3 Polarization within a Vacancy-Centered Cluster

Under an external field, polarization within a vacancy-centered cluster can be achieved by the migration of metal ions in the field direction. The conductive region around each oxygen vacancy resembles a conductive spherical shell as shown in Figure 7.2. Thus, the transport of metal ions within the region can be formulated as the problem of the polarization of a conductive spherical shell embedded in a dielectric material under a uniform field.

For the new, perturbed electrostatic potential outside of the sphere, Laplace's equation gives

$$\nabla^2\phi = 0. \tag{7.2}$$

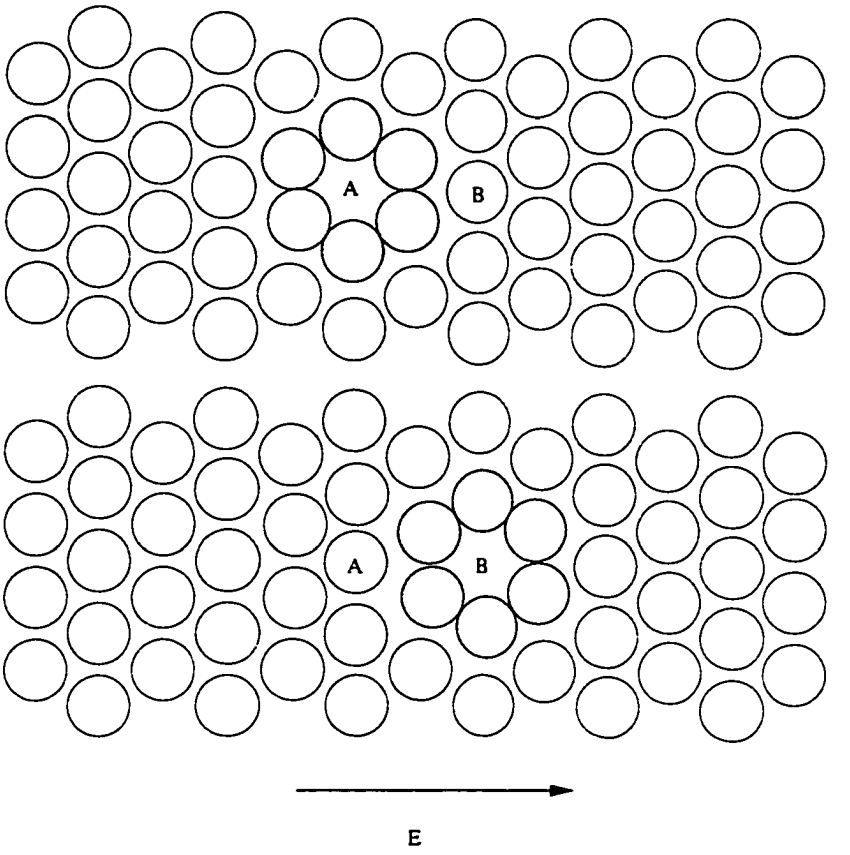

Figure 7.1 The displacement of a vacancy-centered cluster as the vacancy hops from site A to site B. The shaded circles are the oxygen ions neighboring the vacancy.

The method of separation variables was applied to solve the above equation [85]. The choice of the spherical shape of the conductive cluster simplifies the application of the boundary conditions at the surface of the conductor. The potential within the conductive spherical shell has to be uniform after the polarization because a non-zero potential gradient will cause more charge flow. Let the conductive region and the plane $\theta = \pi/2$ be at zero potential, then

$$\phi(r_0) = 0. \tag{7.3}$$

r_0 is the outer radius of the sphere. Because again the potential in the conductive region is required to be uniform, $\frac{\partial \phi}{\partial r}|_{r=r_i} = 0$. Any net charge within the region of $r < r_0$ must migrate to the surface of $r = r_0$. According to Gauss's law,

$$\oint -\frac{\partial \phi}{\partial r}|_{r=r_0} dS = \frac{q_n}{\epsilon}. \tag{7.4}$$

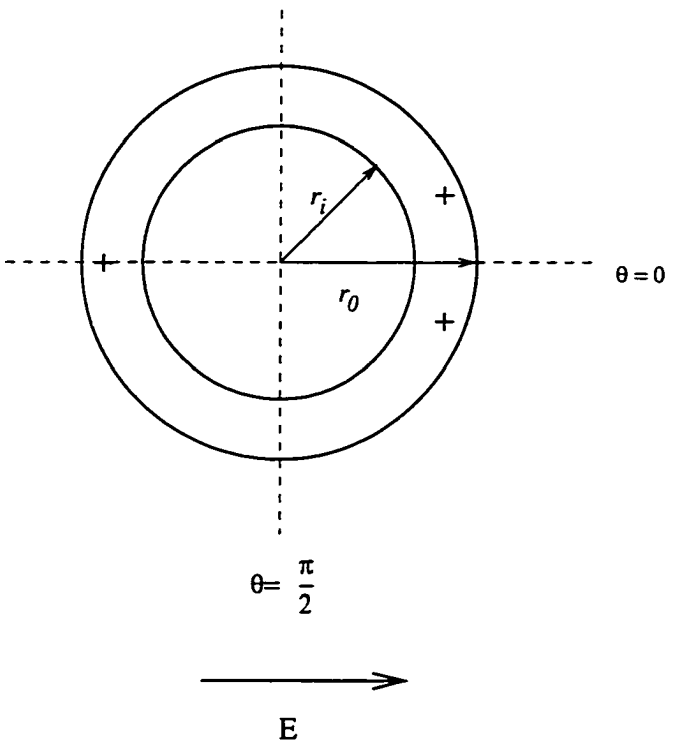

Figure 7.2 The conductive spherical shell. The radius of the outer surface is r_0 and that of the inner surface is r_i.

If the unperturbed electrostatic field is E, the potential far away from the sphere is expressed as

$$\phi(r \to \infty) = -Er\cos(\theta). \tag{7.5}$$

With the above three boundary conditions, the solution of Equation 7.2 is

$$\phi = \frac{q_n}{4\pi\epsilon}(\frac{1}{r} - \frac{1}{r_0}) + Er(\frac{r_0^3}{r^3} - 1)\cos(\theta). \tag{7.6}$$

The induced surface charge density, determined from Equation 7.6 by using Gauss's law, is

$$\sigma = -\epsilon\frac{\partial\phi}{\partial r}|_{r=r_0} = \frac{q_n}{4\pi r_0^2} + 3E\epsilon\cos(\theta). \tag{7.7}$$

Since only metal ions are considered responsible for the polarization, the transport of metal ions can be derived from the surface charge distribution. Based on the above equation, one can see that the surface charge density with $\theta < \pi/2$ is more positive than that with $\theta > \pi/2$. As a result of polarization, the number of metal ions on the downfield side of the spherical

shell is more than that on the upfield side of the spherical shell. The non-uniform distribution of metal ions in the conductive region around a vacancy is *roughly* illustrated on a hexagonal closed-packed layer of oxygen ions in Figure 7.3. The figure illustrates the accumulation of metal ions at the downfield side of the cluster *qualitatively*. A quantitative discussion of this accumulation will be given later in the Discussion section.

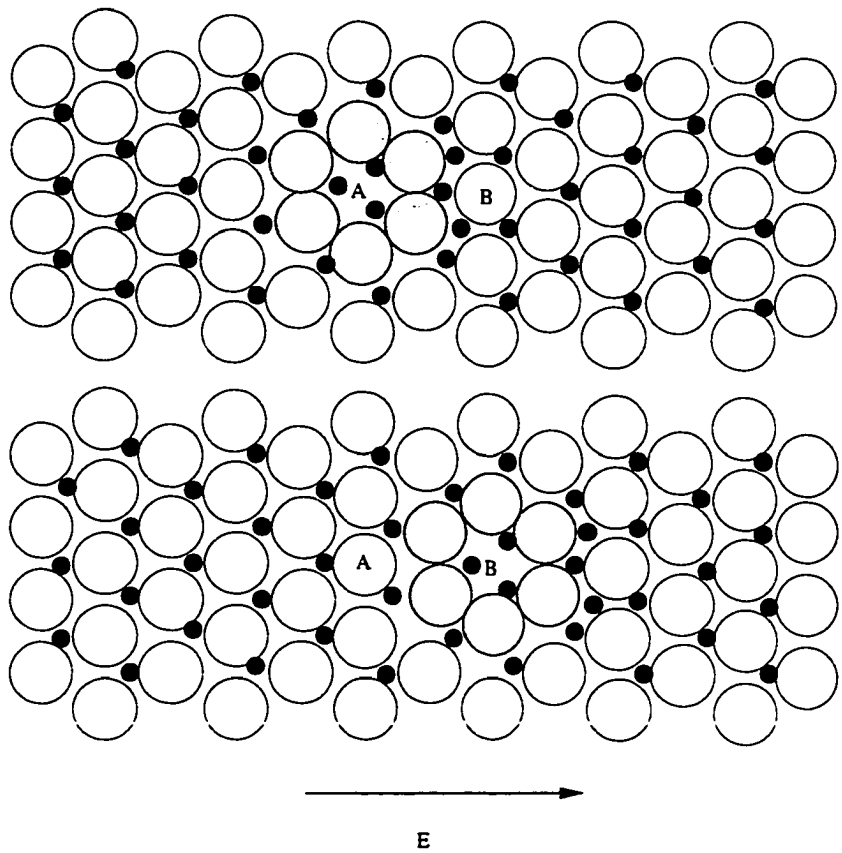

Figure 7.3 The polarization of the vacancy-centered cluster. The large open circles are oxygen ions and the small solid circles are metal ions. The shaded circles are the oxygen ions neighboring the vacancy.

The radius of the conductive region is related to the distribution of the interstitial sites within the region. The interstitial sites are either octahedral or tetrahedral. The distance between the center of the vacancy and that of a tetrahedral site in the conductive region is $1.17a_{O-O}$, where a_{O-O} is the distance between the centers of two neighboring oxygen ions.

The distance between the center of the vacancy and that of an octahedral site in the conductive region is $1.23a_{O-O}$. Because the average O-O distance for the oxides is about 2.98 Å, as shown in Table C.1, the average distance between the center of the oxygen vacancy and that of either type of interstitial site in the conductive region is $1.20 \times 2.98 = 3.57$ Å, which is used later for the value of r_0.

The transference number of metal ion is calculated from the polarization of the conductive region. The details are given in Section 7.6. It should be noted that the above calculation is basically for a macroscopic system, and is used in this work to approximate the *average* polarization behavior of the microscopic conductive region.

7.4 The Hopping of the Oxygen Vacancy

Once a vacancy-centered cluster is polarized spontaneously by an external field, the metal ions in the conductive gap stop moving. The next step is the jump of an oxygen ion immediately outside the cluster into the cluster. A vacancy-centered cluster can allow an addition of another oxygen ion mainly due to the void space offered by the vacancy. The oxygen ion jump is promoted by the electric field as will be discussed below. One possible mechanism for the jump is that the jumping oxygen pushes one of its neighboring oxygen ions in the cluster into the vacancy site in order to make room for its addition at the cluster boundary. As a result of the jump, the vacancy is relocated to the site which the jumping oxygen just left, as shown in Figure 7.1.

If the top of the energy barrier for the motion of the oxygen ion into the cluster is located at the cluster boundary, the frequency for the oxygen ion to jump into the cluster depends on the free energy change associated with the displacement of the oxygen ion from its lattice site to the cluster boundary. Since the metal ions neighboring the jumping oxygen ion are expected to migrate at the same time, one needs to consider the displacements of both metal and oxygen ions to account for the free energy change.

Such simultaneous motions of metal and oxygen ions have been viewed as the rotation of a group having composition MO_p by Fromhold [57], where p is the number of oxygen ions

in a rotation group. If $p = |z_M/z_O|$, MO_p is the stoichiometric unit containing one metal ion, and p is the number of oxygen ions belonging to one metal ion in the oxide. In this model, the transport of metal ions associated with the oxygen jump can be measured as the rotation of a M_pO unit. Similarly, if $p = |z_O/z_M|$, M_pO is the stoichiometric unit containing one oxygen ion, and p is the number of metal ions belonging to each jumping oxygen as well as each stationary oxygen ion in the oxide. If a stoichiometric unit M_pO is considered as an electrically neutral unit embedded in an electrically neutral environment, it constitutes an electric dipole. The electrostatic energy of the oxide increases during its rotation due to dipole-dipole interactions with the surrounding dipoles. On the other hand, non-stoichiometric rotation would also involve electrostatic energy increase due to charge-charge interactions. as metal ions are separated from their stoichiometric units. Therefore, the stoichiometric rotation is considered to be most energetically favorable, and it is taken as the elementary process of oxygen transport.

Figure 7.4 illustrates that the rotation of the stoichiometric unit MO results in the displacements of both ions: the metal ion moves from r_0 to r and the oxygen ion moves from r to r_0. With the presence of a potential difference $\Delta\phi$ between r and r_0 ($\Delta\phi = \phi(r) - \phi(r_0)$), the change in electric potential energy associated with the rotation is $(z_M - z_O)e\Delta\phi$ ($= -2z_O e\Delta\phi$). The free energy change due to the rotation is then written as

$$\Delta F = \Delta F^\circ - 2z_O e\Delta\phi, \tag{7.8}$$

where ΔF° is the free energy change with a uniform potential. If the rotation associated with the oxygen jump is that of the stoichiometric unit of M_pO, the number of metal ions moves from r to r_0 is p and the charge associated with these metal ions is $2e$. As a result, the free energy change due to the rotation of the stoichiometric unit of M_pO is also expressed by Equation 7.8.

The potential difference can be calculated from Equation 7.6 with r_0 equal to the radius of the cluster and r equal to $(r_0 + (1/2)a_{M-O})$, where a_{M-O} is the M-O bond length. The jump frequency is therefore written as

$$\nu_j = \nu\exp(-\frac{\Delta F^\circ}{kT})\exp(\frac{2z_O e\Delta\phi}{kT}) \tag{7.9}$$

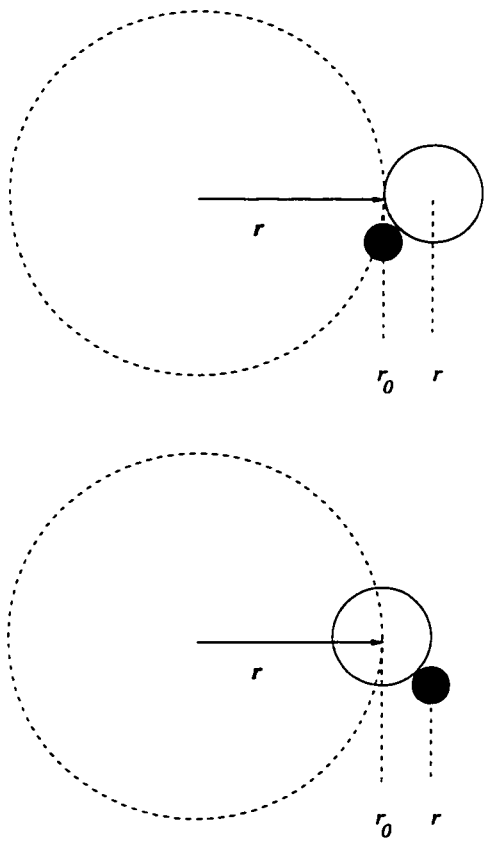

Figure 7.4 The rotation of the stoichiometric unit MO. The large dashed circle represents the cluster boundary. The small solid circle represents a metal ion and the open circle represents an oxygen ion.

$$= \nu_0 \exp(\frac{2z_O e\Delta\phi}{kT}). \tag{7.10}$$

Since the potential difference varies in the θ direction according to Equation 7.6, the jump frequency for an oxygen ion neighboring the cluster depends on its location on the cluster surface.

The frequency variation of the jump caused by the potential gradient, namely (ν_j/ν_0), was calculated as a function of θ. For the vacancy-centered cluster of 12 oxygen ions, the radius of the polarization boundary r_0 is 3.57 Å. The M-O distance for the oxides is approximately 1.7 Å, so r is 5.27 Å. The net cluster charge, q_n, is assigned to be equal to the vacancy charge, $2e$, for the time being, although it can be more as will be explained later. For the case of aluminum oxide, the dielectric constant of 10 and the applied field of 7.3 MV/cm were used

to determine $\Delta\phi(=\phi(r))$, and the plot of $\ln(\nu_j/\nu_0)$ vs. θ is presented in Figure 7.5. The frequency decreases dramatically with θ, which indicates that only that of the jump of the oxygen ion located closest to $\theta = 0$ is considerable.

In Figure 7.1, $\theta = 0$ is located on the right side of the cluster, and $\theta = \pi$ is located on the left side of the cluster. Therefore, the oxygen ion at site B is to jump into the cluster and the vacancy is to hop from site A to site B. The vacancy-centered cluster also moves with the vacancy. The overlap between the old location and the new location of the vacancy-centered cluster is approximately equivalent to the overlap of two spheres of the same size. Let the overlap be enclosed by the surface of $0 < \theta < \theta'$ of the old cluster, as shown in Figure 7.6. The area of this surface, A^R, can be written as

$$A^R = 2\pi r_{cl}^2(1 - \cos\theta'), \tag{7.11}$$

where r_{cl} is the cluster radius. By integrating the surface charge on A^R according to Equation 7.7, one obtains q^R, the total surface charge which remains in the cluster after the vacancy jump, q^R.

$$q^R = \frac{q_n}{2}(1 - \cos\theta') + 3\pi E\epsilon r_{cl}^2(1 - (\cos\theta')^2). \tag{7.12}$$

The charge not included in the new cluster, q^L, is the total surface charge on A^L, the area of the old cluster which does not overlap to the new cluster. q^L is $q_n - q^R$, or

$$q^L = \frac{q_n}{2}(1 + \cos\theta') + 3\pi E\epsilon r_{cl}^2(-1 + (\cos\theta')^2). \tag{7.13}$$

After the jump, the charge q^L becomes immobile space charge.

The value of the overlap angle, θ', needs to be determined for the model calculation described in the next section. Considering the overlap of two spheres of the same size, one can determine the overlap angle from their radii and the distance between the centers. The polarization boundary has a radius of 3.57 Å and the distance between their centers is 5.27 Å, so θ' is 0.25 π.

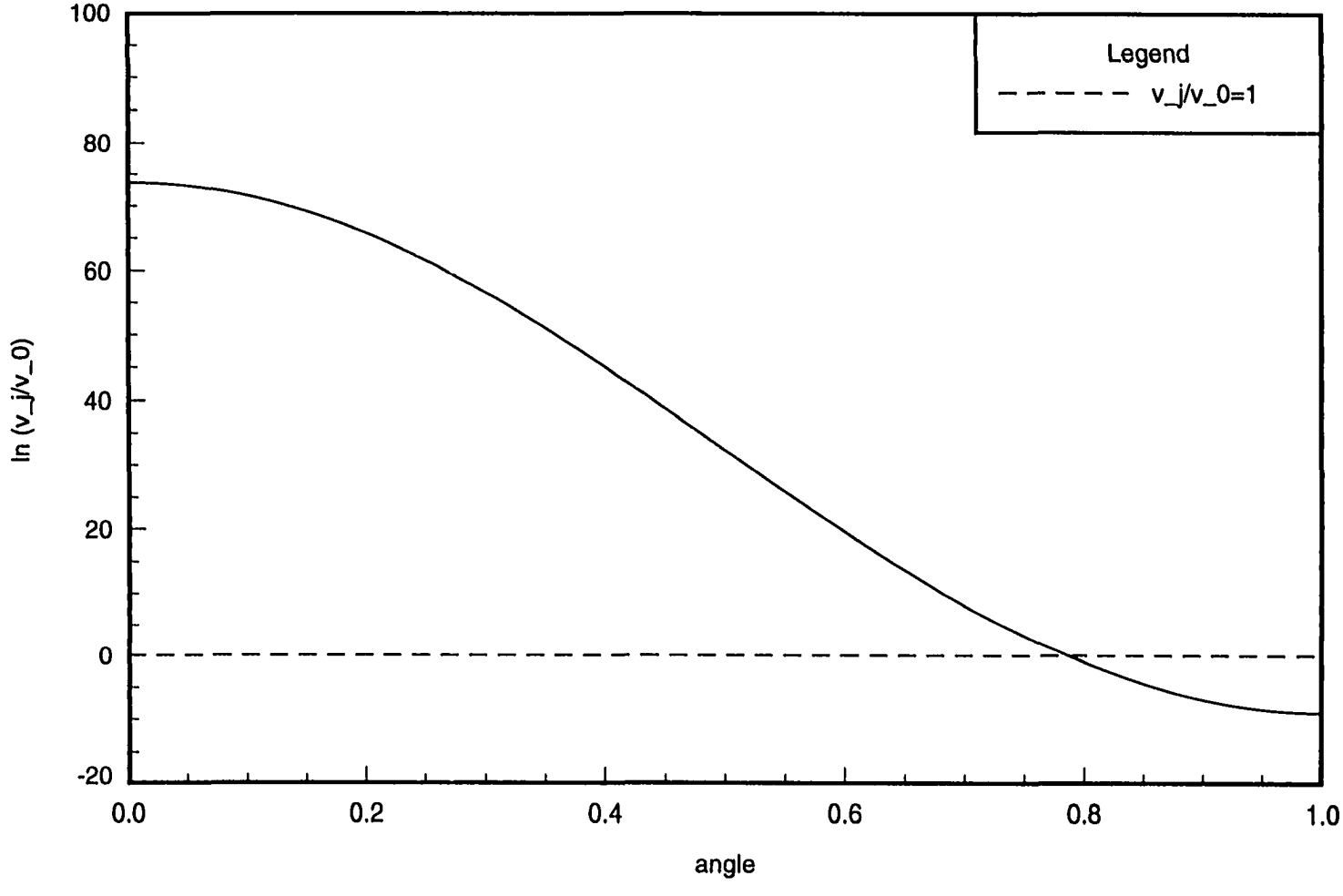

Figure 7.5 The variation of the jump frequency, ν_j/ν_0, in the θ direction.

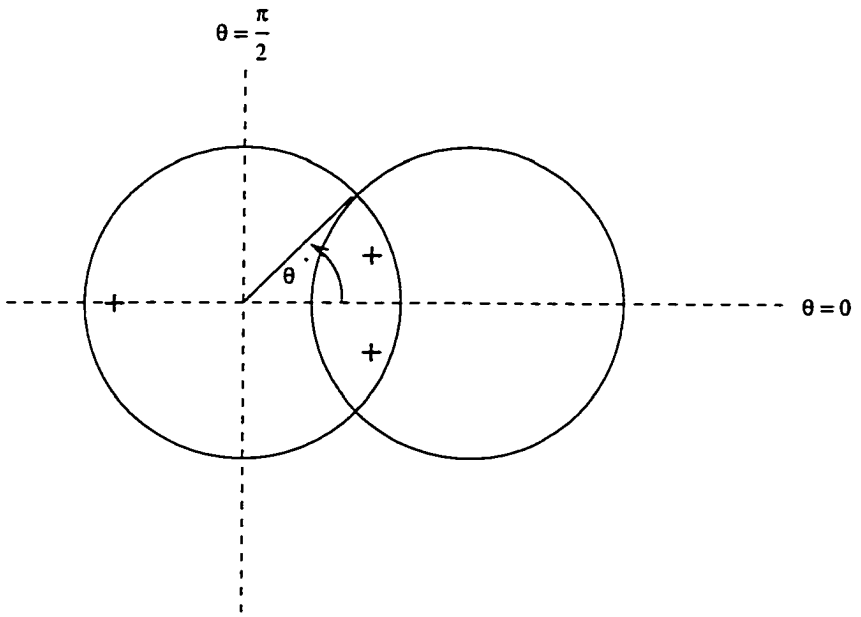

Figure 7.6 The overlap between the old and new locations of a cluster. The large circles represent the cluster boundaries.

7.5 Overall Ionic Conduction Process

The physical processes of the present model includes the hopping of the oxygen vacancy across the oxide film and the polarization of the vacancy-centered cluster between each hop of the oxygen vacancy. Oxygen vacancies are generated near the metal/oxide interface, because some oxygen ions next to the interface react with metal to form new oxide. Once a vacancy is formed, the oxygen ions immediately next to a vacancy will move towards the vacancy and a gap between these oxygen ions and the surrounding ones will appear. The gap is an easy path for the migration of metal ions, so metal ions migrate in the gap according to the electric field, resulting in polarization of the gap. After the polarization one of the oxygen ions next to the gap moves into the cluster and leaves behind a vacancy, as shown in Figure 7.1. As a result, the vacancy changes its location and the cluster associated with the vacancy moves along with it. Around the previous site of the vacancy, the oxygen ions relax back to their original positions so the easy path for metal ion migration no longer exists. On the other hand, the oxygen ions surrounding the new site of the vacancy move towards the vacancy, so another easy path is formed. The two processes, the polarization on the surface of the vacancy-centered

cluster and the oxygen ion jump, take place alternatively until the oxygen vacancy arrives at the oxide/solution interface to be filled by an oxygen ion from solution.

In the mathematical model for ionic conduction across an oxide film, vacancy-centered clusters are the mobile charge carriers in oxide. The charge associated with each cluster, q_n, can be written in terms of the electric field E and q^L,

$$q_n = q^R + q^L \tag{7.14}$$

$$= \frac{6\pi\epsilon r_{cl}^2 E(1-(\cos\theta')^2)+2q^L}{(1+\cos\theta')}. \tag{7.15}$$

In the region outside the moving charged clusters, immobile space charge may exist due to the non-stoichiometric concentration of metal ions vs. oxygen ions, which is described by Q_s as

$$Q_s = Fz_M(c_M - \frac{|z_O|}{|z_M|}c_O), \tag{7.16}$$

where c_M and c_O are the concentrations of metal ions and oxygen ions, and z_M and z_O are the charge numbers of the metal ions and the oxygen ions respectively. According to the model, lattice oxygen ions are immobile, so c_O is fixed and any variation of Q_s is related to a variation of c_M.

When the vacancy at the center of a cluster is filled by an oxygen ion, the charge of an oxygen ion is introduced into the cluster. If this charge is evenly distributed, the total charge left behind by the cluster after it moves with the vacancy is then approximately $(q^L + z_O e A^L/A_{cl})$, where A_{cl} is the surface area of the cluster, z_O is the charge number of the oxygen ions, and e is the elementary charge. On the other hand, the new cluster includes some new ions which did not belong to the old cluster before the oxygen jump. As the new cluster forms around the new vacancy site, immobile charge associated with new ions becomes a part of the mobile cluster charge. This incorporated charge is approximately equal to $(\frac{A^L}{A_{cl}}\frac{4}{3}\pi r_{cl}^3)Q_s$. Therefore, on the upfield side of a moving cluster, immobile space charge is generated, and on the downfield side of a moving cluster, immobile space charge is absorbed by the cluster. As vacancy-centered clusters sweep through a region, the immobile space change density outside moving clusters could be altered. In order to macroscopically model Q_s in terms of this process, the cluster size is assumed to be much smaller than the length scale on which Q_s varies. Hence,

the time dependence of Q_s is written as

$$\frac{\partial Q_s}{\partial t} = N_A c_{cl} \frac{v_{cl}}{a}((q^L + (1+\cos\theta')\frac{z_O e}{2}) - (Q_s(1+\cos\theta')\frac{V_{cl}}{2})), \tag{7.17}$$

where v_{cl}, c_{cl}, and V_{cl} are the velocity, the concentration and the volume of the cluster respectively. a is the distance between the old vacancy site and the new one. The right side of the equation consists of two terms: The first term represents the charge left behind by the cluster as the cluster moves with the vacancy, and the second term represents the charge which is included in the moving cluster.

The mole balance on moving clusters is

$$\frac{\partial c_{cl}}{\partial t} = -\frac{\partial (c_{cl} v_{cl})}{\partial x}. \tag{7.18}$$

The space charge consists of the charge in the clusters and the charge outside the clusters. To calculate the net space charge density, one must consider both parts. The part of the space charge density due to the charge carried by the clusters is $c_{cl} q_n N_A$. Since the volume fraction of the region outside of the clusters is $(1 - N_A c_{cl} V_{cl})$, the part of the space charge density due to the immobile charge outside of the clusters is $Q_s(1 - N_A c_{cl} V_{cl})$ (when c_{cl} is small, i.e. less than 10^{-4} $mole/cm^3$, the volume fraction of the clusters is generally negligible). The space charge density is then $(c_{cl} q_n N_A + Q_s(1 - N_A c_{cl} V_{cl}))$. As a cluster moves through the oxide, the charge which moves with a cluster is $(q_n - Q_s V_{cl})$, so the charge flux, or the current, is $N_A c_{cl} v_{cl}(q_n - Q_s V_{cl})$. Accordingly, the charge balance is written as

$$\frac{\partial (c_{cl} q_n N_A + Q_s(1 - N_A c_{cl} V_{cl}))}{\partial t} = -\frac{\partial (N_A c_{cl} v_{cl}(q_n - Q_s V_{cl}))}{\partial x}. \tag{7.19}$$

Poisson's equation is applied to relate the gradient of the electric field, E, to the space charge density,

$$\frac{\partial E}{\partial x} = \frac{(q_n c_{cl} N_A + Q_s(1 - N_A c_{cl} V_{cl}))}{\epsilon}. \tag{7.20}$$

The cluster velocity is the vacancy velocity, and the hopping frequency of the vacancy is equal to the jump frequency of an oxygen ion. Therefore,

$$v_{cl} = a\nu_j = a\nu \exp(-\frac{\Delta F^\circ}{kT}) \exp(\frac{2 z_O e \Delta\phi}{kT}). \tag{7.21}$$

$\Delta\phi$ is a function of E and q_n according Equation 7.6.

The model consists of four equations, Equation 7.17, 7.18, 7.19, and 7.20 with four variables, c_{cl}, E, Q_s, and q_n. Experimentally, oxide films grow at a constant rate when a constant current is applied. For numerical convenience, the quasi-steady-state approximation was used in solving the modeling equations. Namely, within a very short period, the film thickness is unchanged. At the quasi steady state, all the time derivatives in the model equations are zero. As a result, both the current ($= N_A c_{cl} v_{cl}(q_n - Q_s V_{cl})$) and the mole flux of the cluster ($=c_{cl} v_{cl}$) are independent of x, which makes $(q_n - Q_s V_{cl})$ independent of x.

According to Equation 7.17 at steady state, Q_s can be related to q^L as

$$Q_s = \frac{2q^L + z_O e(1 + \cos\theta')}{(1 + \cos\theta')V_{cl}}, \tag{7.22}$$

Since q^L is related to E and q_n according to Equation 7.13, Q_s in Equation 7.20 can be written in terms of q_n and E as

$$Q_s = \frac{q_n - 6\pi\epsilon r_{cl}^2 E(1 - \cos\theta') + z_O e}{V_{cl}}. \tag{7.23}$$

By rearranging this equation, one relates the charge which moves with a cluster, $(q_n - Q_s V_{cl})$, to the electric field E as

$$q_n - Q_s V_{cl} = 6\pi\epsilon r_{cl}^2 E(1 - \cos\theta') - z_O e. \tag{7.24}$$

As explained above, $(q_n - Q_s V_{cl})$ is independent of x at steady state, so E is constant across the oxide as well. The electric field is uniform only if the space charge density is zero, meaning

$$c_{cl} q_n N_A + Q_s(1 - N_A c_{cl} V_{cl}) = 0. \tag{7.25}$$

Based on Equation 7.25 and 7.24, Q_s and q_n can be written in terms of c_{cl} and E as

$$Q_s = -N_A c_{cl}(6\pi\epsilon r_{cl}^2 E(1 - \cos\theta') - z_O e), \tag{7.26}$$

$$q_n = (1 - N_A c_{cl} V_{cl})(6\pi\epsilon r_{cl}^2 E(1 - \cos\theta') - z_O e). \tag{7.27}$$

By substituting Equation 7.27 into Equation 7.6 and then Equation 7.6 into Equation 7.21, one finds that the cluster velocity v_{cl} depends on c_{cl} and E. Thus, the flux of clusters ($=v_{cl} c_{cl}$)

is a function of c_{cl} and E. Based on Equation 7.18 at steady state, $v_{cl}c_{cl}$ is independent of x. Since E is a constant, c_{cl} is a constant as well.

Therefore, at steady state, the electric field and the cluster concentration are both uniform in the oxide. The cluster charge q_n and the space charge density outside of the clusters are also constant across the oxide. The net space charge density is zero.

7.6 Model Calculations

For the model calculations, the values of the cluster concentration c_{cl} and the electric field E need to be specified. According to Cabrera and Mott [86], the oxidation at the metal/oxide interface takes place at certain active sites, such as "kinks". If the rate limiting process for ionic conduction is the hop of the oxygen vacancy across the oxide, the vacancy concentration near the metal/oxide interface is then dependent on the density of active sites at the metal/oxide interface. The density of kink sites is considered constant, so the cluster concentration c_{cl} may be assumed to be constant at the metal/oxide interface. c_{cl} should be much smaller than the concentration of lattice ions, which is on the order of 10^{-2} $mole/cm^3$. E is variable, for example ranging from 7.3 MV/cm to 8.1 MV/cm for the case of aluminum oxide. The values of some of the parameters in the equations for the steady state have been given before, e.g. $r_{cl} = 3.57$ Å, $r = 5.27$ Å and $\theta' = 0.25\pi$. Note that a in Equation 7.17 is equivalent to r in Equation 7.6.

The values of Q_s and q_n with c_{cl} set to 10^{-4} $mole/cm^3$ are listed in Table 7.1 with the corresponding applied field and dielectric constant for each oxide. The results for aluminum oxide are plotted in Figure 7.7 as an example. As shown in the figure, Q_s decreases linearly with E but q_n increases linearly with E. Q_s can be decreased by the decrease of c_M in the region outside of the clusters. q_n can be increased by the addition of metal ions into a cluster. These two processes can occur at the same time by the transfer of some metal ions in the region outside of the clusters into the clusters. In other words, when E is increased, some metal ions are transfered into the clusters due to higher polarization. Remember that the net space charge is still zero.

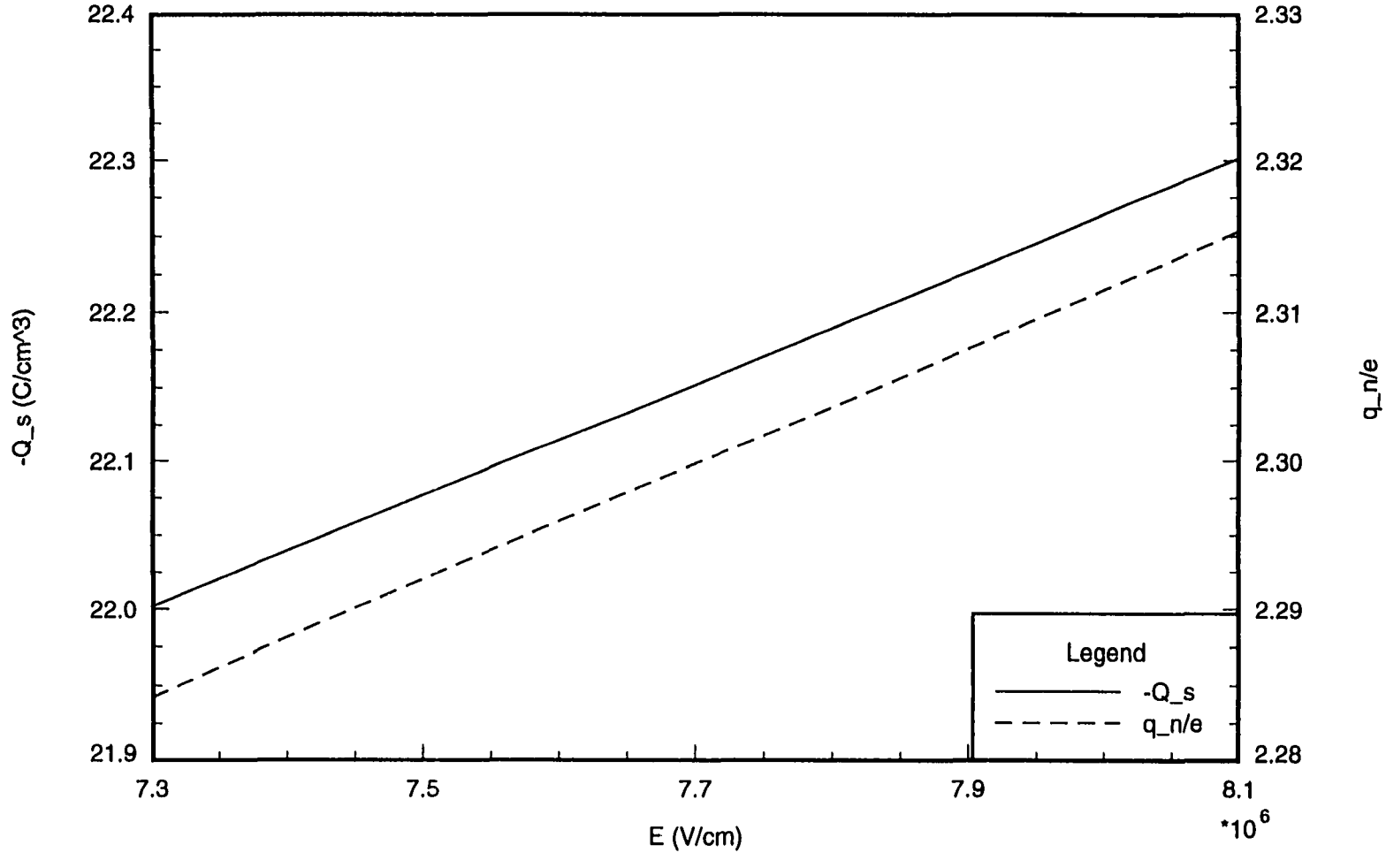

Figure 7.7 $(-Q_s)$ and q_n vs. E for aluminum oxide with c_{cl} set to 10^{-4} $mole/cm^3$.

With the given field ranges, the variations of Q_s and q_n are all small. This result suggests that the transient changes in the applied current during film growth can be achieved very rapidly by varying the electric field. Note that if a different value of c_{cl} were applied in the calculation, Q_s is proportional to c_{cl}, but q_n is independent of c_{cl} when $c_{cl} < 10^{-4}\ mole/cm^3$.

Table 7.1 The values of Q_s, q_n and q^R at steady state.

Oxide	ϵ/ϵ_0	$E\ (MV/cm)$	$-Q_s\ (C/cm^3)$	q_n/e	q^R/e
Al_2O_3	10.0 [39]	7.3-8.1 [39]	22.0-22.3	2.28-2.32	0.58-0.61
Ta_2O_5	23.2 [56]	5.8-7.2 [70]	24.3-25.5	2.52-2.65	0.82-0.94
Nb_2O_5	41.4 [55]	3.5-5.0 [71]	24.7-27.0	2.56-2.80	0.86-1.10
WO_3	41.7 [53]	4.9-5.9 [53]	26.9-28.5	2.80-2.96	1.09-1.25

When a cluster arrives at the oxide/solution interface, an oxygen ion from solution fills the oxygen vacancy and some of the metal ions in the cluster near the oxide/solution interface will react with solution to form new oxide at the oxide/solution interface. The net charge to be discharged at the oxide/solution interface is $(q_n - V_{cl}Q_s - 2e)$ per cluster, which is solely associated with metal ions. On other hand, for every cluster created at the metal/oxide interface, an oxygen ion is extracted from the original oxide to react with metal to form new oxide. Therefore, the transference number of metal ions is calculated as

$$t_M = \frac{q_n - V_{cl}Q_s - 2e}{q_n - V_{cl}Q_s}, \tag{7.28}$$

$$= \frac{6\pi\epsilon r_{cl}^2 E(1-\cos\theta')}{6\pi\epsilon r_{cl}^2 E(1-\cos\theta') + 2e}. \tag{7.29}$$

The transference number is independent of the cluster concentration but it is dependent on electric field, dielectric constant, and the cluster radius. Table 7.2 summarizes the calculated transference numbers of various metal oxides according their applied electric fields and dielectric constants. Some of the experimental values from Table 6.2 are listed for comparison. Note that the experimental values listed in the table are obtained by using various experimental current densities, not by using the electric fields specified in the table. As described in Section 7.2.2, the experimental values of t_M for the oxides increase with current density in most cases. However due to the limited quantity of t_M data, the experimental relation between t_M and E cannot be well defined. The plots of the calculated transference number vs. the electric field

are presented in Figure 7.8. In general, the calculated transference number increases linearly with the electric field.

The relation between the current density i and electric field E is also of interest. The formula for the current density i in the model is written as

$$i = (q_n - Q_s V_{cl}) N_A c_{cl} v_{cl} \tag{7.30}$$

$$= (q_n - Q_s V_{cl}) N_A c_{cl} a\nu \exp(-\frac{\Delta F^\circ}{kT}) \exp(\frac{2 z_O e \Delta\phi}{kT}). \tag{7.31}$$

Again, the values of q_n, Q_s and $\Delta\phi$ all can be calculated from the values of c_{cl} and E. With $c_{cl} < 10^{-4}\ mole/cm^3$, $Q_s V_{cl}$ is negligible in comparison with q_n, and $N_A c_{cl} V_{cl}$ in Equation 7.27 can be neglected as well. In the above equation, a is approximately equal to 5.27 Å and ν is $10^{12}\ sec^{-1}$ [86]. The values of ΔF° are expected to be on the order of magnitude of 1 eV [86]. The value of ΔF° is not required for the determination of B in the equation of $i = A\exp(BE)$. However, for the plot of $\log(i)$ vs. E, a value of ΔF° for each oxide is determined from the experimental current density at the lower value of the applied field listed in Table 7.2. Again, c_{cl} is taken to be $10^{-4}\ mole/cm^3$. The values of ΔF° for the oxides are as follows; for aluminum oxide $\Delta F^\circ = 2.56\ eV$, for tantalum oxide, $\Delta F^\circ = 1.87\ eV$, for niobium oxide, $\Delta F^\circ = 1.35\ eV$, and for tungsten oxide, $\Delta F^\circ = 1.01\ eV$. The calculated current density and the experimental current density are plotted vs. the electric field in Figure 7.9. The slopes of all four model curves are nearly the same, which is $(4.81 \pm 0.02) \times 10^{-6}\ cm/V$ and the slopes of the experimental curves are given in Table 6.1.

Table 7.2 The transference numbers of the oxides.

Oxide	ϵ/ϵ_0	$E\ (MV/cm)$	Calculated t_M	Experimental t_M
Al_2O_3	10.0 [39]	7.3-8.1 [39]	0.12-0.14	0.40-0.45
Ta_2O_5	23.2 [56]	5.2-7.2 [70]	0.21-0.25	0.24-0.31
Nb_2O_5	41.4 [55]	3.5-5.0 [71]	0.22-0.29	0.22-0.33
WO_3	41.7 [53]	4.9-5.9 [53]	0.28-0.32	0.30-0.37

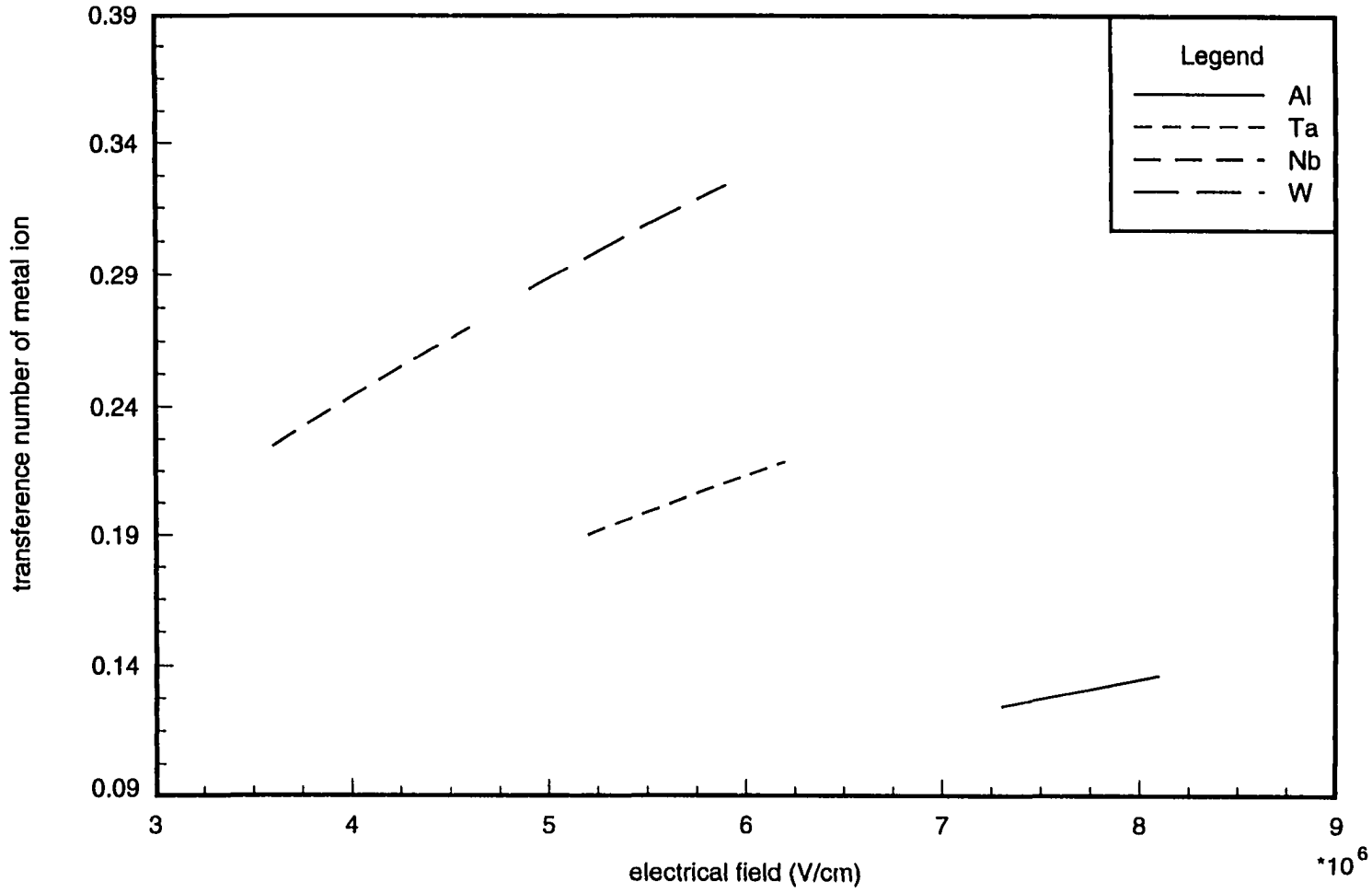

Figure 7.8 The transference number t_M vs. the electric field E of the oxides.

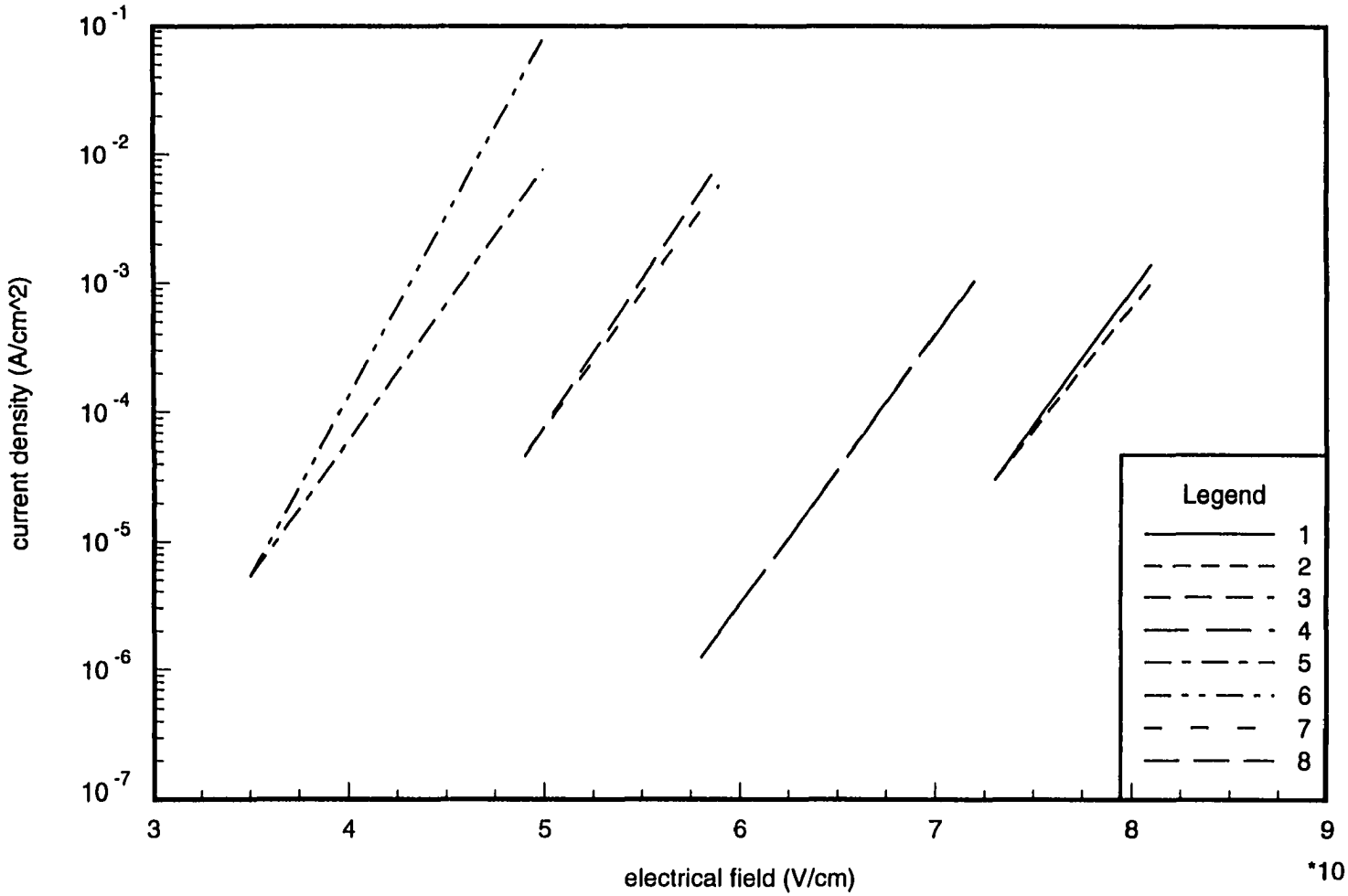

Figure 7.9 Current density i vs. electric field E from the modelings and experimental data. Curves 1, 3, 5 and 7 are the modelings for the oxides of Al, Ta, Nb, and W respectively. Curves 2, 4, 6, and 8 are the experimental data for the oxides of Al [39], Ta [70], Nb [71], and W [53] respectively.

7.7 Discussion

The defect cluster model predicts comparable transference numbers for metal and oxygen ions and the high field conduction current-field relation observed during the growth of anodic oxide films on Al, Ta, Nb, and W. The knowledge of the experimental dielectric constants of these anodic oxide films and the applied electric fields in these films allowed the calculations of transference numbers based on the model. The rate limiting step for ionic conduction in this model is the jump of an oxygen ion neighboring the defect cluster into the cluster, and the energy barrier for the jump is modified by the potential gradient along the path of the jump. This potential gradient determines the field coefficient B in the current-field relation $i = \exp(BE)$.

The transference numbers of metal ions predicted by this model agree with the experimental value well except that of aluminum ion, as shown in Table 7.2. The calculated t_{Al} is lower than the experimental value. The difference can be reduced if the cluster radius r_{cl} is more than 3.57 Å, since the transference number increases with the cluster radius r_{cl} according to Equation 7.29. In fact, it is reasonable to expect larger defect clusters in aluminum oxide due to the small size of aluminum ions. For the sake of clarity, the sizes of the metal ions are listed in Table 7.3 with two different coordination numbers (CN). By comparing the sizes of the metal ions with the same CN, one can see that Al^{+3} is the smallest in the table. In the determination of $r_{cl} = 3.57$ Å for the previous model calculations, the inward displacement of the oxygen ions surrounding an oxygen vacancy has been considered to decay so rapidly with the distance from the vacancy center that only the gap between the first layer and the second layer of oxygen ions is widened enough for metal ions to migrate easily. This may not be the case for aluminum oxide. For small metal ions like aluminum ions, a small increase in the gap width can be sufficient for their easy migration. Therefore, the smaller gap between the second layer and the third layer of oxygen ions surrounding an oxygen vacancy may allow aluminum ions to migrate until polarization is achieved.

Assuming that aluminum ions can migrate easily in the gap between the second layer and the third layer of oxygen ions surrounding an oxygen vacancy, one then changes the value of

Table 7.3 The radii of the metal ions [82].

metal ion	radius with CN=4, (Å)	radius with CN=6, (Å)
Al^{+3}	0.39	0.54
Ta^{+5}		0.64
Nb^{+5}	0.48	0.64
W^{+6}	0.42	0.60

r_{cl} to 6.57 Å for the model calculation. The new value of r_{cl} is calculated as the sum of the previous value 3.57 Å and the distance between the inner gap and the outer gap, which is approximately 3 Å. r is then 8.27 Å and θ' is 0.28 π. The calculated results with these new parameters are given in Table 7.4 along with the previous calculated results with r_{cl} = 3.57 Å. Q_s, q_n and t_{Al} still vary proportionally with E, similar to the previous results shown in Figure 7.7 and 7.8. The increase of q_n with r_{cl} indicates that larger vacancy-centered clusters carry more excess aluminum ions. Hence, the transference number of aluminum ions increases with r_{cl}. The new values of t_{Al} are very close to the experimental values. The new value of the field coefficient B is different from the previous one, but it is still close to the experimental values. The outcome suggests that the radii of the vacancy-centered clusters in aluminum oxide may be closer to 6.57 Å than 3.57 Å.

Table 7.4 The calculated results with two different values of r_{cl} for aluminum oxide.

r_{cl} Å	$-Q_s$ (C/cm^3)	q_n/e	q^R/e	t_{Al}	B (cm/V)
6.57	30.7-32.0	3.19-3.32	1.55-1.68	0.37-0.40	5.28×10^{-6}
3.57	22.0-22.3	2.28-2.32	0.58-0.61	0.12-0.14	4.80×10^{-6}

For comparison, the transference numbers and the field coefficients with r_0 = 6.57 Å for the other oxides were also calculated and listed in Table 7.5. Similarly, the calculated transference numbers are significantly higher than the previous results with r_0 = 3.57 Å, and the B values are close to the previous results. Since the previous results of t_M with r_0 = 3.57 Å are closer to the experimental data, the radii of the vacancy-centered clusters in tantalum oxide, niobium oxide and tungsten oxide may be closer to 3.57 Å than 6.57 Å.

So far, it is assumed that the polarization within the conductive gap surrounding each

Table 7.5 The calculated results with $r_{cl} = 6.57$ Å for Ta_2O_5, Nb_2O_5 and WO_3.

Oxide	$-Q_s$ (C/cm^3)	q_n/e	q^R/e	t_M	B (cm/V)
Ta_2O_5	40.1-45.5	4.16-4.73	2.56-3.09	0.52-0.58	5.31×10^{-6}
Nb_2O_5	42.0-51.8	4.37-5.28	2.73-3.74	0.54-0.63	5.37×10^{-6}
WO_3	51.4-58.0	5.34-6.02	3.70-4.38	0.63-0.67	5.35×10^{-6}

oxygen vacancy can be accomplished by the accumulation of metal ions at the downfield side of the vacancy-centered cluster. Since each metal ion must occupy an interstitial site, the accumulation of metal ions is possible only if there are enough interstitial sites. The estimation of the number of interstitial sites between the first layer and the second layer of oxygen ions surrounding a vacancy is given as follows.

In a FCC packing of oxygen ions, the number of octahedral sites belonging to an oxygen ion is 1 and that of tetrahedral sites is 2. Hence, the number of the interstitial sites belonging to the first layer of oxygen ions and the vacancy is $(2+1)\times13 = 39$. The number of octahedral sites around an oxygen ion is 6 and that of tetrahedral sites around an oxygen ion is 8. Hence, the number interstitial sites around the vacancy and within the first layer of oxygen ions is 14. As a result, the number of interstitial sites belonging the first layer oxygen ions and located within the conductive gap is (39-14)=25. Since some of the interstitial sites in the conductive gap belongs to the third layer oxygen ions, the number of interstitial sites in the gap is more than 25. For the oxides considered in this work, only a fraction of interstitial sites are occupied. Aluminum ions occupy 2/9 of interstitial sites, tantalum and niobium ions occupy 2/15 of interstitial sites, and tungsten ions occupy 1/9 of interstitial sites. In other words, each metal ion are neighbored by 3 to 8 vacant interstitial sites in various oxides.

The accumulation of metal ions is measured by q^R, the total surface charge between $0 < \theta < \theta'$. Based on the values of q^R/e given in Table 7.1, only less than one extra metal ion is located between $0 < \theta < \theta'$ in the gap after polarization. The number of the interstitial sites between $0 < \theta < 0.25\pi$ is more than 3 $(= 25A^R/A_{cl})$. 2 of the 3 sites must be vacant because a low fraction (less than 1/3) of interstitial sites are occupied by metal ions as explained above. The two vacant sites can easily accommodate one extra metal ion, so the polarization of the

conductive gap can be achieved. For the polarizations with $r_0 = 6.57$ Å, the values of q^R are given in Table 7.4 and 7.5, which correspond to less than one extra metal ion located between $0 < \theta < 0.28\pi$ on the cluster surface. Apparently more vacant sites are located between the second layer and the third layer of oxygen ions than those between the first layer and the second layer, so more than 2 vacant sites can be found between $0 < \theta < 0.28\pi$ on the cluster surface. Therefore, the polarization with $r_0 = 6.57$ Å can also be achieved.

When a vacancy-centered cluster is just formed at the metal/oxide interface, it carries a $2e$ charge associated with the metal ions coordinating the oxygen vacancy. According to the calculation results for steady state, the charge associated with a vacancy-centered cluster, q_n, is always greater than $2e$. This means that some metal ions must be added to the cluster at the metal/oxide interface before the cluster moves away from the interface. The addition of positively charged metal ions into a positively charge cluster may be explained on the basis of the electric field on the cluster surface after polarization. According to Equation 7.6, the electric field in the r direction around a polarized cluster is

$$E_r = \frac{q_n}{4\pi\epsilon r^2} + E(2\frac{r_0^3}{r^3} + 1)\cos(\theta). \tag{7.32}$$

For a cluster still in contact with metal, a negative value of E_r at $\theta = \pi$ and $r = r_0$ would lead to the migration of the metal ions newly formed by the oxidation of metal into the cluster. The addition of positively charged metal ions into the cluster increases q_n and therefore increases $E_r(r_0, \pi)$ according to Equation 7.32. This migration of metal ions across the metal/cluster interface may no longer be possible when $E_r(r_0, \pi)$ increases to zero. Consequently, the value of q_n with $E_r(r_0, \pi) = 0$ can give an estimation of the maximum quantity of metal ions which could be added into a cluster at the metal/oxide interface. By comparing this value of q_n with the steady state value of q_n, one may show the possibility of steady state. The values of q_n calculated from Equation 7.32 with $E_r(r_0, \pi) = 0$ are listed in Table 7.6 for the oxides. The steady state values of q_n are also listed in the table for comparison. Since the steady state values of q_n are all smaller, it is suggested that the steady state values of q_n is possible by the addition of metal ions into clusters.

Table 7.6 The values of q_n calculated from Equation 7.32 with $E_r(r_0, \pi) = 0$ and its steady state values.

Oxide	ϵ/ϵ_0	E (MV/cm)	r_0 (Å)	q_n/e, (Eqn. 7.32)	q_n/e, steady state
Al_2O_3	10.0 [39]	7.3-8.1 [39]	6.57	6.57-7.29	3.19-3.32
Ta_2O_5	23.2 [56]	5.2-7.2 [70]	3.57	3.21-4.44	2.52-2.65
Nb_2O_5	41.4 [55]	3.5-5.0 [71]	3.57	3.85-5.50	2.56-2.80
WO_3	41.7 [53]	4.9-5.9 [53]	3.57	5.43-6.54	2.80-2.96

The polarization calculations presented in Section 7.3 are valid when the surface charge density σ is not too high. If the surface charge density σ is very high, the electrostatic repulsion between point charges needs to be considered. This repulsion acts against charge accumulation, so the polarization by the external electric field may not be completed.

7.8 Conclusions

A defect cluster model has been developed for ionic conduction in amorphous anodic oxide films. A defect cluster in this context is a vacancy-centered cluster which is created by the extensive ionic displacement in response to the creation of an oxygen vacancy. The physical processes in the model include the hopping of oxygen vacancies, as the rate limiting step, and the metal ion transport within each vacancy-centered cluster. Since each vacancy-centered cluster moves as its center, an oxygen vacancy, hops downfield, the metal ion transport within each cluster can proceed through an oxide.

The metal ion transport within a vacancy-centered cluster was quantitatively modeled as the polarization of a conductive cluster under an electric field. A mathematical model was formulated for the overall ionic conduction across an oxide. The modeling equations were solved for the quasi steady state of constant current. On the basis of the steady-state solution, the transference number t_M and the field coefficient B in the current-field relation $i = A\exp(BE)$ were derived for Al_2O_3, Ta_2O_5, Nb_2O_5 and WO_3. The model calculations give values of t_M very close to the experimental values. Also with the consideration that the hopping of an oxygen vacancy involves the rotation of a stoichiometric unit OM_p, the model predicts the values of B to be about 5×10^{-6} cm/V for all the oxides, which is close to most of experimental values.

8 GENERAL CONCLUSIONS

This dissertation includes two parts: Part I investigates the structural change of the oxide film on aluminum caused by cathodic charging and hoped to link any possible change in the oxide film to pitting susceptibility. Part II proposed a defect cluster model to quantitatively simulate the correlated motions of metal and oxygen ions in an amorphous oxide during anodic oxidation.

In Part I, a mathematical model was formulated to investigate the structural change of the oxide film on aluminum due to cathodic charging. The model assumed a duplex film structure composed of a barrier layer on the metal side and a porous layer on the solution side. The processes formulated in the model include all relevant capacitive processes, conduction in both layers of the oxide film, and the interfacial reactions, such as pore filling by oxide growth at potential higher than the open circuit potential. The model was fit with the anodic current transients during subsequent anodic polarization to determine the structural parameters in the model. The relation between structural changes of the oxide film caused by cathodic charging and the rate of pitting corrosion when the metal was brought to an anodic potential soon after cathodic charging is of interest in this work.

The model produced the experimental anodic current decays from mA/cm^2 range to $\mu A/cm^2$ range over several orders of magnitude variation of time (ms to s). The structural parameters show the decrease of the inner pore-free layer thickness from initial 28 Å to 15-20 Å and the increase of the porosity of the outer porous layer to 0.02 as the results of cathodic charging ($Q_c < 7\ mC/cm^2$). These changes were considered as the growth of pores in the outer portion of the initial film. The pores may be produced by the non-uniform electrochemical dissolution of the oxide during cathodic current flow; however the rate of pore penetration

is too high to be expected from the kinetics of this reaction. A small fraction of pores may penetrate entirely through the oxide film and expose metal for pitting in chloride solutions.

In Part II, a defect cluster model has been developed for ionic conduction in amorphous anodic oxide films. A defect cluster in this context is a vacancy-centered cluster which is created by the extensive ionic displacement in response to the creation of an oxygen vacancy. The physical processes in the model include the hopping of oxygen vacancies, as the rate limiting step, and the metal ion transport within each vacancy-centered cluster. Since each vacancy-centered cluster moves as its center, an oxygen vacancy, hops downfield, the metal ion transport within each cluster can proceed through an oxide.

The metal ion transport within a vacancy-centered cluster was quantitatively modeled as the polarization of a conductive cluster under an electric field. A mathematical model was formulated for the overall ionic conduction across an oxide. The modeling equations were solved for the quasi steady state of constant current. On the basis of the steady-state solution, the transference number t_M and the field coefficient B in the current-field relation $i = A\exp(BE)$ were derived for Al_2O_3, Ta_2O_5, Nb_2O_5 and WO_3. The model calculations give values of t_M very close to the experimental values. Also with the consideration that the hopping of an oxygen vacancy involves the rotation of a stoichiometric unit OM_p, the model predicts the values of B to be about 5×10^{-6} cm/V for all the oxides, which is close to most of experimental values.

APPENDIX A THE ELECTRICAL CONDUCTIVITY OF THE POROUS LAYER

During the cathodic charging period at -2.0 V, the cathodic current increased with time initially possibly because the electrical resistance of the oxide film decreased due to non-uniform dissolution of the film. After increasing for about 8 sec, the cathodic current started to decay at a constant rate. Meanwhile, the film mass increased at a constant rate [11]. Since the film growth may result in the increase of the film electrical resistance, Lin and Hebert suggested that the decay of the cathodic current is caused by the film growth.

For the structural model shown in Figure 4.2, the inner layer is considered to be the native oxide layer. The mass increase measured by QCM during cathodic charging is therefore considered to be due to the growth of the porous layer. Since the electrical conductivity of the porous layer is assumed to be uniform in the electrical model, i and ϕ_p are related as

$$\phi_p = i\frac{L}{\kappa}. \tag{A.1}$$

The potential drop across the metal/film/solution system is

$$V_H - V_r = \phi_2 + i(\frac{L}{\kappa} + A_e R_3). \tag{A.2}$$

L can be calculated from the mass increase, Δm (g/cm^2), and the density, ρ (g/cm^3). According to equation 4.37, ϕ_2 is approximately constant since the cathodic current decays only within a small range. By rearranging the above equation, one gets

$$\Delta m = \frac{\kappa\rho}{i}(V_H - V_r - \phi_2) - \kappa\rho A_e R_3. \tag{A.3}$$

Δm *vs.* $1/i$ was plotted in reference [11] and the slope and the intercept are 1.46×10^{-8} $A - g/cm^4$ and -1.78×10^{-8} g/cm^2. The density of aluminum hydroxide, 2.4 g/cm^3, is used

for ρ by assuming the porosity of the porous layer is small. $A_e R_3$ is about 30 $\Omega - cm^2$. Hence, the conductivity of the porous layer, κ, calculated from the intercept, is 2.5×10^{-8} $\Omega^{-1} cm^{-1}$. Consequently, $(V_r + \phi_2)$ calculated from the slope is -1.485 V. For comparison, Dzimitrowicz *et al.* [40] reported 6×10^{-9} $\Omega^{-1} cm^{-1}$ for the proton conductivity of hydrous aluminum oxide produced by precipitation, on the same order of the magnitude as the calculated value of κ.

APPENDIX B COMPUTER PROGRAM

This computer program models the current transient at -0.4 V after a 3 sec interruption at -0.9 V, which is shown in Figure 5.7. The number of the collocation points is eight. When the accumulated calculation error is unacceptable, the program ends by itself. For the further calculation, the number of the collocation points was reduced to seven and the final solutions of i, ξ, ϕ_2, and $\phi_{p,j}$ obtained by this program are used as the initial conditions.

```
C                       Declare variables
      INTEGER     NP ,NEQ, NPARAM
      PARAMETER   (NP=8, NEQ=NP+3, NPARAM=50)
C
      INTEGER     IDO, IEND, IMETH, INORM, NOUT
      REAL        A(1,1), FCN, FCNJ, HINIT, PARAM(NPARAM), TOL, X,
     &            XEND, Y(NEQ), CUR, E(10), YN(5), ZCN(5),
     &            V, IA1, R
      EXTERNAL    FCN, IVPAG, SSET, UMACH
C
      DIMENSION   ZC(10), Q(10, 10), C(10, 10), D(10, 10),
     &            QINV(10, 10), AC(10,10), BC(10,10)
      COMMON      AC, BC,  V, IA1, R
C
       OPEN (UNIT=25,FILE='ITRA8',STATUS='NEW')
C
      ZC(1) = 0.
      ZC(2) = 0.0337652429
      ZC(3) = 0.1693953068
      ZC(4) = 0.3806904070
      ZC(5) = 0.6193095931
      ZC(6) = 0.8306046933
      ZC(7) = 0.9662347571
      ZC(8) = 1
       ZCN(1) = 0.0469100771
       ZCN(2) = 0.2307653450
```

```
       ZCN(3) = 0.5000000000
       ZCN(4) = 0.7692346551
       ZCN(5) = 0.9530899230
      DO 10 I = 1, NP
      DO 10 J = 1, NP
      Q(I, J) = ZC(I)**(J-1)
      C(I, J) = (J-1)*ZC(I)**(J-2)
      D(I, J) = (J-1)*(J-2)*ZC(I)**(J-3)
  10  CONTINUE
C
      CALL LINRG(NP, Q, 10, QINV, 10)
C
      CALL MRRRR(NP,NP,C,10,NP,NP,QINV,10,NP,NP,AC,10)
      CALL MRRRR(NP,NP,D,10,NP,NP,QINV,10,NP,NP,BC,10)
C
      HINIT = 1.0E-4
      INORM = 2
      IMETH = 2
      CALL SSET (NPARAM, 0.0, PARAM, 1)
      PARAM(1) = HINIT
      PARAM(10)= INORM
      PARAM(12)= IMETH
C
      IDO = 1
      X   = 0
      DO 6 I = 1, NP
      Y(I)= 48.026835*0.032E-3 *(1-ZC(I))
    6 CONTINUE
      Y(NP+1)= 0.8895811
      Y(NP+2) = 0.0560464
      Y(NEQ) = 1.
      TOL = 1.0E-4
C
      DO 12 IEND=1, 100
        XEND = IEND*0.00002
        CALL IVPAG (IDO, NEQ, FCN, FCNJ, A, X, XEND, TOL, PARAM, Y)
C                     Output results
         WRITE (25,*) X, (V-Y(NP+1)-Y(1)-Y(NP+2))/R*1000.,
     &   IA1*1.E3
         PRINT '(T8,A,F10.7)','XI=', X
         PRINT '(T8,A,F10.7)','Y(1)=', Y(1)
         PRINT '(T8,A,F10.7)','Y(NP+1)=', Y(NP+1)
         PRINT '(T8,A,F10.7)','Y(NP+2)=', Y(NP+2)
         PRINT '(T8,A,F10.7)','Y(NP+3)=', Y(NP+3)
       CALL MRRRR (NP,NP,QINV,10,NP,1,Y,10,NP,1,E,10)
      DO 50 I= 1, 5
```

```
      YN(I)= E(1)+E(2)*ZCN(I)+E(3)*ZCN(I)**2+E(4)*
     &    ZCN(I)**3+E(5)*ZCN(I)**4+E(6)*ZCN(I)**5+
     &    E(7)*ZCN(I)**6 + E(8)*ZCN(I)**7
      PRINT '(T8,A,I1,A,F10.7)','Y(',(I+1),')=', YN(I)
   50 CONTINUE
   12 CONTINUE
C                          Finish up
      IDO = 3
      CALL IVPAG (IDO, NEQ, FCN, FCNJ, A, X, XEND, TOL, PARAM, Y)
C
      CLOSE(25)
      END
C
      SUBROUTINE FCN (NEQ, X, Y, YPRIME)
      INTEGER    NEQ, NP
      REAL       X, Y(NEQ), YPRIME(NEQ), C12, R, DEL, K, ALF,
     &           V, BA, L, IAO, AS, ASS, KK, ILO, ICO, P, B1, B2,
     &           ALFC, ALFP, ALFM, G, IL, IA1, FT, DELO, VOL
      DIMENSION  S(10), AC(10,10), BC(10,10), ZC(10)
      COMMON AC, BC, V, IA1, R
C
      C12 = 5.E-6
      R = 40.32
      IAO = 9.8E-12
      BA = 4.86E-6
      DEL = 4.8026825E-8
      K = 0.1E-8
      ALF = DEL**2/0.003
      V = -0.13 + 1.5784562
      FT = 96500./8.314/298.15
      P = 0.2
      VOL = 20.
      L = 20.E-8 * 1.4412308
      KK = VOL/(P*3*96500*L)
      ICO = 3.6E-6*P
      ILO = 2.6E-6*P
      ALFM = 0.24
      ALFP = 1.76
      ALFC = 1.11
C
      NP = NEQ -3
      IL = ILO*(EXP(ALFP*FT*Y(NP+2))-EXP(-ALFM*FT*Y(NP+2)))
      G = FT*(ALFC*ICO*EXP(ALFC*FT*Y(NP+2))+ALFP*ILO*
     &   EXP(ALFP*FT*Y(NP+2))+ALFM*ILO*EXP(-ALFM*FT*Y(NP+2)))
      B1 = BA/(Y(NEQ)*L)*IAO*(EXP(Y(NP+1)*BA/(Y(NEQ)*L))
     &     +EXP(-Y(NP+1)*BA/(Y(NEQ)*L)))
```

```
      IA1 = IA0*(EXP(Y(NP+1)*BA/(L*Y(NEQ)))
     &   -EXP(-Y(NP+1)*BA/(L*Y(NEQ))))
      B2 = ((V-Y(NP+1)-Y(NP+2)-Y(1))/R-IA1)/C12
C
      DO 5 I = 1, NP
       S(I) = 0
   5  CONTINUE
C
      Y(1) = (V-Y(NP+1)+AS-Y(NP+2))/(1-R*K/DEL*AC(1,1))
      DO 20 I = 1, NP-1
      DO 20 J = 1, NP
      S(I) = S(I) + BC(I,J)*Y(J)*ALF/DEL**2
  20  CONTINUE
C
      DO 40 I = 1, NP-1
      YPRIME(I) = S(I)
  40  CONTINUE
C
       YPRIME(NP) = 0
       YPRIME(NP+3) =  KK*IL
       YPRIME(NP+1) = (B2*G+B1*Y(NP+1)/(Y(NEQ)*L)*KK*IL*L)
     &       /(G+B1)
       YPRIME(NP+2)=   B2-YPRIME(NP+1)
C
      RETURN
      END
```

APPENDIX C FREE VOLUME MODEL AND CONDUCTIVE CLUSTER

The free-volume model was first applied to the amorphous phase to link glass transition to thermal expansion [87]. In the model, the transition from glass to liquid can be associated with the introduction of appreciable volume into the system. In this work, this model is used for the determination of the variation of the O-O distances across an oxide. As explained in Chapter 7, the mobility of metal ions may depend on the O-O distances. Therefore, with the knowledge of the O-O distance distribution in an oxide, one can determine whether there exists an easy path for metal ions to migrate.

The first assumption in the model is that a local volume v on the molecular scale can be associated with each molecule. The local free energy, $f(v)$, a function of cell volume, has a form similar to the underlying intermolecular potential. In order to distinguish between solidlike and liquidlike cells, $f(v)$ is approximated as the following.

$$f(v) = f(v_0) + \frac{1}{2}K(v - v_0)^2, \; v < v_c, \tag{C.1}$$

$$= f(v_0) + L(v - v_c), \; v > v_c. \tag{C.2}$$

v_0 corresponds to the minimum on the curve of $f(v)$ vs. v, and the critical volume v_c is related to the location of the point of inflection. K and L are constants. The free volume is defined as $v_f = v - v_c$ as the linear regime of $f(v)$ permits the free exchange of free volume among neighboring cells. In other words, two adjacent cells with volume in excess of v_c can transfer a volume increment between them because the energy increase of the expanding cell is exactly balanced by the energy decrease of the contracting one. Therefore, cells with $v > v_c$ are called liquidlike, while those with $v < v_c$ are called solidlike. Liquidlike clusters are clusters of liquidlike cells, each one of which has a sufficiently large number of liquidlike neighbors that

a free exchange of free volume can take place within the cluster, without constraining any changes in the volumes of any neighboring solidlike cells simultaneously.

The distribution of cell volumes is determined by minimizing the free energy. In addition to the summation of local free energy of all cells in the system, the free energy also depends on the entropy of mixing of solidlike and liquidlike cells, and the communal entropy. The communal entropy arises from the delocalization of the molecules out of their individual cells and their consequent movement throughout the communal volume of a liquidlike cluster. The intricate mathematical development of the Cohen-Grest free-volume thermodynamic theory of the glass transition cannot be treated here in depth. In short, by optimizing the free energy, Cohen and Grest [81] derived the following expressions for the probability of a cell that has a volume v as

$$P(v) = M\exp(-\frac{K(v-v_0)^2}{2kT}),\ v < v_c, \tag{C.3}$$

$$= N\exp(-\frac{v-v_c}{\bar{v}_f}),\ v > v_c. \tag{C.4}$$

M and N are constants and $\bar{v}_f$ is the average free volume. The probability that a cell is liquidlike is

$$p = \int_{v_c}^{\infty} P(v)dv, \tag{C.5}$$

If p is known, the distribution of liquidlike clusters across a solid can be simulated through a computer experiment. Considering solid as composed of a number of ordered sites, one simply determines one random number for each site and occupies the site if the random number is smaller than p and the site has a sufficient large number of occupied neighbors. Finite liquidlike clusters in the lattice grow as p increase from small values. At the percolation threshold, p_c, an infinite cluster forms across the lattice. At this point the entire material behaves as a liquid.

The application of free volume model ideas to ionic conduction in amorphous oxides is now considered. The oxides contain ions of two different sizes. The radii of metal ions (Al, Ta, Nb, and W) are roughly half the radius of an oxygen ion or less [82]. If a cell volume is associated with each oxygen ion, as cell volumes expand, oxygens are generally farther apart. When the space between oxygen ions are open to a certain degree, metals ions can migrate under the

electric field from one interstitial site to another with little activation energy, as is the case in the liquid phase. For the purpose of describing ionic conduction, conductive cells are defined as those with a sufficiently large volume that metal ions can easily move through the oxygen lattice.

Because oxides are at a temperature much lower than the glass transition temperature, the approximation of no free volume, defined as above, can be adopted. Hence, to simulate the fluctuation of cell volumes, equation C.3 are used to obtain $p(v)$. By applying the constraints of $p(\infty)$ equal to one and the relation between $P(v)$ and the average cell volume $\bar{v}$ as

$$\bar{v} = \frac{\int_{v_0}^{\infty} P(v)vdv}{\int_{v_0}^{\infty} P(v)dv}, \tag{C.6}$$

equation C.3 can be rewritten as

$$p(v) = erf(\frac{v - v_0}{\sqrt{\pi}(\bar{v} - v_0)}). \tag{C.7}$$

The average cell volume $\bar{v}$ can be determined from the oxide density.

In the computer simulation of cell volume distribution, amorphous oxide is considered as a FCC packing of oxygen ions with metals ions located at interstitial sites, similar to the structure of crystalline aluminum oxide. First, the numbers and sizes of *intrinsic* conductive clusters are simulated by the program given at the end of this appendix. The program was developed base on the computational technique outlined by Binder and Stauffer [89]. Basically, every site in FCC lattice is given a random number, and if a site has a random number smaller than p and at least six of its neighbors have also a random number smaller than p, the site is considered as an element of a conductive cluster.

The number of octahedral voids belonging to one sphere in a closest packing is one, and that of tetrahedral voids is two. Because of the low stoichiometric ratio of metal vs. oxygen in the oxides, only a fraction of interstitial sites in the oxides are occupied by metal ions. Each metal ion is surrounded by some vacant interstitial sites, so it can find a vacant site to hop into under a driving force. In contrast, oxygen ions in the oxides are closely packed and cannot hop unless a oxygen vacancy happens to be nearby.

For a metal ion to hop between tetrahedral and octahedral sites in a FCC oxygen lattice, it has to pass through a 3-fold coordinated hole formed by three oxygen ions, the size of which depends on O-O distance. In general, the average O-O distance can be estimated from the average cell volume determined from the density. For instance, according to the density data given in Table C.1, the average O-O distance, a_{O-O}, is about 3.0 Å. If a metal ion was squeezed into a 3-fold coordinated void, the M-O distance would be $0.5775a_{O-O}$. On the other hand, tetrahedral and octahedral M-O distances would be $0.6125a_{O-O}$ and $0.707a_{O-O}$ respectively.

Table C.1 The average cluster size along with the density and ionic radius data used for the probability calculations.

Oxide	Density (g/cm^3)	v/v_0	Average O-O (Å)	$r_{M^{+n}}$ Å [82]	Conductive O-O (Å)	v/v_0	p	$\sum n(s)s/\sum n$
Al_2O_3	3.17 [54]	1.25	2.94	0.39	3.00	1.33	0.30	3.3
Ta_2O_5	8.03 [83]	1.32	2.99	0.48	3.15	1.55	0.17	1.5
Nb_2O_5	4.74 [83]	1.31	2.98	0.48	3.15	1.55	0.16	1.4
WO_3	6.80 [53]	1.33	2.99	0.42	3.05	1.40	0.33	4.7

The known value for tetrahedral Al-O bond length in crystalline compounds is 1.75 Å and that for octahedral Al-O bond length is 1.95 Å [88]. However, the Al-O bond length associated with a 3-fold coordinated cation is not available. Note that the repulsion force increases with the coordination number (CN), which in turn increases the M-O bond length. Therefore, the M-O bond length associated a 3-fold coordinated cation should be smaller than that associated with a tetrahedral coordinated cation. Conventionally, M-O bond length has been divided into two individual radii for M and O, which again depend on coordination number. The radius of O^{-2} with CN equal to 3 is 1.36 Å and that with CN equal to 4 is 1.38 Å. However, the radius of Al^{+3} with CN equal to 3 is not available. Therefore, the Al-O bond length with a 3-fold coordination is estimated to be 1.73 Å considering only the change in the O^{-2} radius with CN. Without the adjustment for the Al^{+3} radius with CN, this estimated value may be a little high. According to the ionic radius data of some metal ions given in Reference [82], i.e. Be^{+2} and Te^{+4}, the radius with CN equal to 3 is generally about 0.1 Å less than that with CN equal to 4. If this difference is considered, then the Al-O bond length with a 3-fold coordination could be 1.63 Å or smaller.

Assuming that an aluminum ion can pass through the 3-fold coordinated holes which can accommodate 1.73 Å Al-O bond length, one then determines the minimum oxygen cell volume required for the easy migration of aluminum ions based on the minimum required O-O distance. For the other oxides, the required O-O distance for the easy migration of metal ions was adjusted based on the difference in the sizes of metal ions. In Table C.1 the cationic radius data are for the tetrahedral coordinated cations. For instance, Ta^{+5} is about 0.09 Å greater than Al^{+3} in radius, so the Ta-O bond length with CN equal to 3 is estimated to be 1.82 Å and the required O-O distance for the easy migration of Ta is 3.15 Å.

The parameters used in Equation C.7 for the calculation of $p(v)$ are given in Table C.1. v in the table represents the minimum cell volume of a conductive cell calculated based on the minimum required O-O distance. v_0 is the cell volume of oxygen ions in the crystalline oxide with a FCC oxygen lattice, which can be determined from the density data. Crystalline aluminum oxides have various crystalline structures, and among them α-alumina has a hexagonal closed-packed oxygen lattice and a highest density, 3.99 g/cm^3. For the other oxides listed in Table C.1, none of their crystalline structures are known exactly to be hexagonal [90], so the corresponding density data cannot be used for the determination of $\bar{v}$. Therefore, the density of α-alumina was used for the determination of $\bar{v}$ for all four oxides. Table C.1 gives the probability for the simulations of various oxide. In the computer simulation of conductive clusters, the program gives every site on a FCC lattice of 10^6 a random number, and if a site has a random number smaller than p and at least six of its neighbors have also a random number smaller than p, the site is considered as an element of a conductive cluster. The purpose of the six-neighbor requirement is to simulate only compact, or approximately spherical clusters, instead of branching clusters. For cationic interstitials to migrate throughout a conductive cluster under an external electric field, 3-fold coordinated voids, each of which is centered between three conductive cells, can be found across a compact conductive cluster, but this is not the case for a branching conductive cluster. The simulation results with the probabilities for aluminum oxide and tantalum oxide are shown in Figure C.1 as the plots of the cluster number, $n(s)$, vs. the cluster size, s. These clusters represent finite isolated local regions in

the oxides in which metal ions can migrate across the oxygen lattice and change their oxygen neighbors. The average cluster sizes defined as $\frac{\sum n(s)s}{\sum n}$ are given in Table C.1.

The low values of p indicate that only a small fraction of the oxygen cells are conductive. This is due to the fact that the variation in the cell volume associated with each oxygen ion is very small and few oxygen cells have a sufficiently large volume for the easy migration of metal ions. Therefore, the cluster sizes are in general very small. The existence of finite conductive clusters in the oxides suggests that metal ions could migrate across oxygen the lattice under an electric field in some local bounded regions in which the oxygen ions are farther apart. The oxygen ions are considered to be relatively stationary because any exchange of their cell volumes will result in an increase of local free energy according to the free-volume model.

```
      INTEGER     NL, MAXS, MAX
      PARAMETER   (NL=100,MAXS=NL*NL, MAX=(NL+1)**2*10)
      DIMENSION   LEVEL((NL+1)*(NL+1)), N(MAX), NS(7), NSUM(32),
     +            NSM(10*MAXS), LOLD((NL+1)*(NL+1)),
     +            INDEXP(NL*NL), LABELP(NL*NL), LABELN(NL*NL)
      LOGICAL     RNT((NL+1)*(NL+1)), RNC((NL+1)*(NL+1)),
     +            RNB((NL+1)*(NL+1))
      LOGICAL     TOP, LEFT, TL, U1, U2, U3
      INTEGER     INTEG
      REAL*8    G05CAF, COUNTP, CHI, CHIP
      EXTERNAL  G05CAF
      DATA NSUM/32*0/, NS/7*0/
*
      L=NL
      P=  0.1682
      TAUM1=96.0/91.0
      ALOG2=1.0000001/ALOG(2.0)
      LARGE=2048
      MAX6=MAX*6
      N(MAX)=MAX
      LP1=L+1
      LIMIT=MAX-L*L*0.40
      IREC=0
      INDEX=0
      CHI=0
      CHIP=0
      COUNTP=0
```

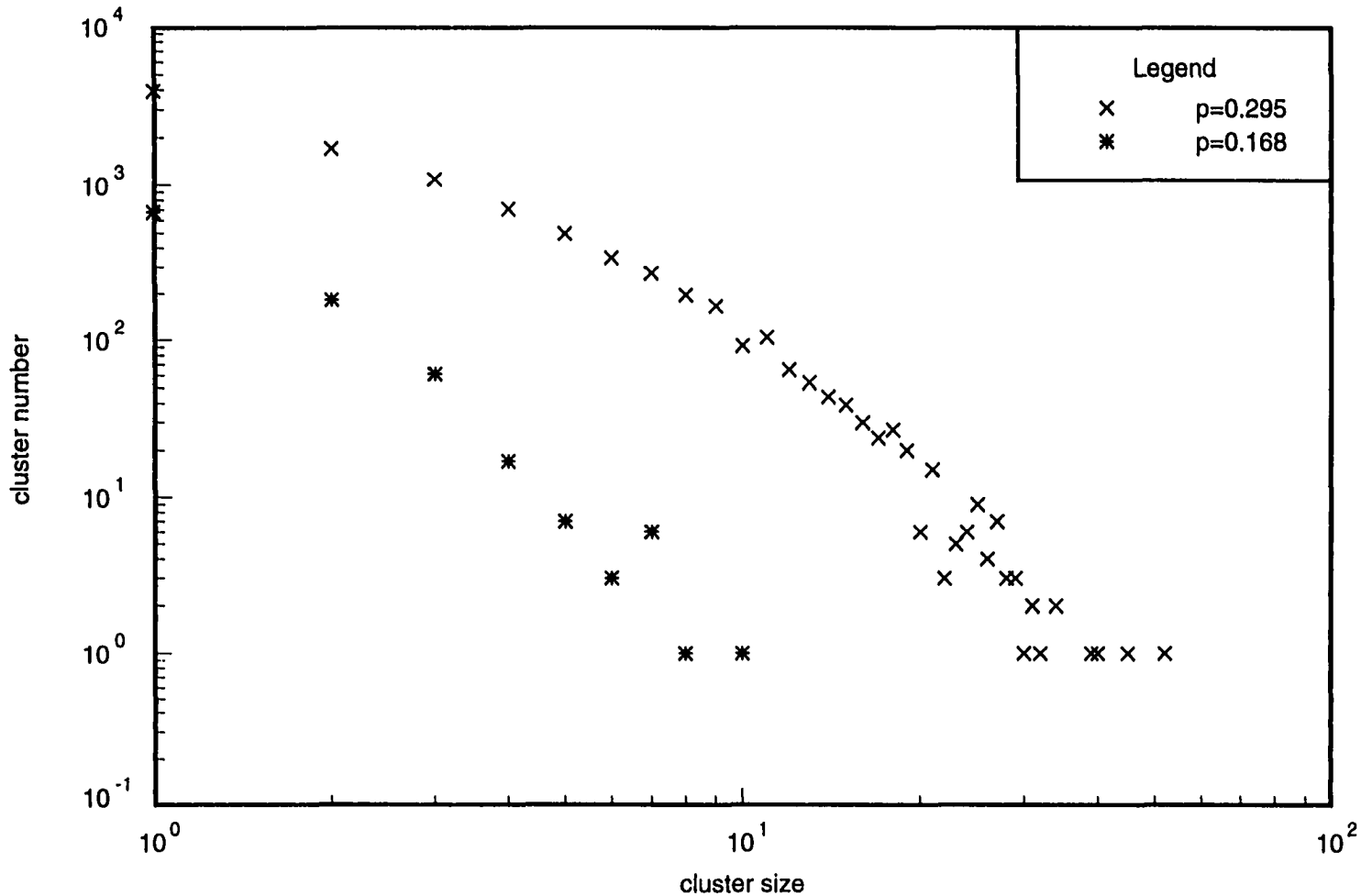

Figure C.1 The number vs. the size of the conductive clusters with $p = 0.295$ and $p = 0.168$.

```
      COUP=0
      IF(L.GT.131070) STOP 1
      INDC=0
*
      DO 1 I=1, (NL+1)**2
         RNT(I)=0
 1       LEVEL(I)=MAX
*
      DO 100 I=1, LP1
         RNC(I)=0
 100     RNB(I)=0
      DO 110 J=2, LP1
         RNC(1+(J-1)*LP1)=0
         RNB(1+(J-1)*LP1)=0
         DO 110 I=2, LP1
            RNC(I+(J-1)*LP1)=(G05CAF(X).LE.P)
 110        RNB(I+(J-1)*LP1)=(G05CAF(X).LE.P)
*
      DO 3 K=2, LP1
         write(13,*) K-1, COUP
         IF ((K.GT.4).AND.(COUP.EQ.0)) THEN
         WRITE(*,*) 'PERCOLATION STOP AT', K-1
         write(*,*)
         DO 58 I=1, LP1*LP1
            IF (LEVEL(I).EQ.MAX) GOTO 58
            COUP=COUP+1
            INDEXP(COUP)=I
            LABELP(COUP)=LEVEL(I)
 58      CONTINUE
         COUPOLD=COUP
         GOTO 40
         END IF
*
* check the percolation
         IF (K.EQ.3) THEN
         DO 44 I=1, LP1*LP1
           IF (LEVEL(I).EQ.MAX) GOTO 44
           COUP=COUP+1
           INDEXP(COUP)=I
           LABELP(COUP)=LEVEL(I)
 44        CONTINUE
         COUPOLD=COUP
         END IF
*
         IF (COUP.NE.0.AND.K.GT.3.AND.K.LT.L) THEN
         COUP=0
```

```
      DO 204 I=1, LP1*LP1
      IF (LEVEL(I).EQ.MAX) GOTO 204
      DO 202 IP=1, COUPOLD
      IF (LEVEL(I).NE.LABELP(IP)) GOTO 202
         COUP=COUP+1
         INDEXP(COUP)=I
         LABELN(COUP)=LABELP(IP)
         GOTO 204
202   CONTINUE
204   CONTINUE
      DO 38 I=1, COUP
38       LABELP(I)=LABELN(I)
      COUPOLD=COUP
      END IF
*
40    INDC=INDC+1
      IF (INDC.EQ.3) INDC=0
      IF(INDEX.LT.LIMIT) GOTO 20
*
      IREC=IREC+1
      IF(K.LE.3) STOP 2
      J=INDEX
      DO 21 JD=2, LP1
      DO 21 I=2, LP1
         IC=I+(JD-1)*LP1
         LEV=LEVEL(IC)
         IF(LEV.EQ.MAX) GOTO 21
*
         IF(LEVEL(IC-1).NE.MAX) GOTO 24
         LABEL=LEV
         IF(N(LEV).GE.0) GOTO 27
         MS=N(LEV)
22       LABEL=-MS
         MS=N(LABEL)
         IF(MS.LT.0) GOTO 22
         N(LEV)=-LABEL
         IF(LABEL.GT.INDEX) GOTO 25
27       J=J+1
         N(J)=N(LABEL)
         N(LABEL)=-J
         LEVEL(IC)=J-INDEX
         GOTO 21
24       LEVEL(IC)=LEVEL(IC-1)
         GOTO 21
25       LEVEL(IC)=LABEL-INDEX
21    CONTINUE
```

```
         IF(J.GE.MAX) STOP 3
         IF(IREC.EQ.1) WRITE(*,2) P, J
*
* locate the cells which are parts of percolation
         write(*,*) 'K=', K, 'COUP=', COUP
         DO 46 IP=1, COUP
C            write(16,*) INDEXP(I), LABELP(I), LEVEL(INDEXP(I)),
C     +                  LABELN(I)
 46         LABELP(IP)=LEVEL(INDEXP(IP))
*
         DO 26 IS=1, INDEX
         NIS=N(IS)
         IF(NIS.LE.0) GOTO 26
         FNIS=NIS
         CHI=CHI+FNIS*FNIS
         CHIP=CHIP+FNIS
         NSM(NIS)=NSM(NIS)+1
         IF(NIS.GE.8) GOTO 261
         NS(NIS)=NS(NIS)+1
         GOTO 26
*
 261     INTEG=ALOG(FNIS)*ALOG2-2
         NSUM(INTEG)=NSUM(INTEG)+1
C         IF(NIS.GE.LARGE) WRITE(*,97) NIS
 26      CONTINUE
*
         INDEX1=J-INDEX
         IF(INDEX1.LE.0) STOP 4
         DO 23 IND=1, INDEX1
 23         N(IND)=N(IND+INDEX)
         INDEX=INDEX1
         IF(IREC.NE.(IREC/500)*500) GOTO 20
         WRITE(*,2) P,INDEX,J,K
         WRITE(*,96) NS, J
         WRITE(*,93) NSUM
 20      CONTINUE
*
         DO 106 I=1, LP1*LP1
 106        LOLD(I)=LEVEL(I)
*
         IF (K.EQ.2) GOTO 300
         DO 200 I=1, (LP1**2)
            RNT(I)=RNC(I)
 200        RNC(I)=RNB(I)
         DO 205 I=1, LP1
 205        RNB(I)=0
```

```
      DO 210 JD=2, LP1
         RNB(1+(JD-1)*LP1)=0
         DO 210 I=2, LP1
210      RNB(I+(JD-1)*LP1)=(G05CAF(X).LE.P)
*
300   DO 3 JD=2, LP1-1
      DO 3 I=2, LP1-1
         IC=I+(JD-1)*LP1
         IF(.NOT.RNC(IC)) GOTO 9
         IF(INDC.EQ.1) GOTO 62
         IF(INDC.EQ.2) GOTO 63
         IF(INDC.EQ.0) GOTO 64
62       IF(INT(RNC(IC+1))+INT(RNC(IC+LP1))+INT(RNC(IC+1+LP1))+
     +      INT(RNC(IC-1))+INT(RNC(IC-LP1))+INT(RNC(IC-LP1-1))+
     +      INT(RNT(IC))+INT(RNT(IC+LP1))+INT(RNT(IC+1+LP1))+
     +      INT(RNB(IC))+INT(RNB(IC-1))+INT(RNB(IC+LP1)).GT.(-6))
     +      GOTO 9
         MLEFT=LEVEL(IC-1)
         LTOP=LEVEL(IC-LP1)
         MTOP=LTOP
         LTL=LEVEL(IC-1-LP1)
         MTL=LTL
         LU1=LOLD(IC)
         MU1=LU1
         LU2=LOLD(IC+LP1)
         MU2=LU2
         LU3=LOLD(IC+1+LP1)
         MU3=LU3
         GOTO 1000
63       IF(INT(RNC(IC+1))+INT(RNC(IC+LP1))+INT(RNC(IC+1+LP1))+
     +      INT(RNC(IC-1))+INT(RNC(IC-LP1))+INT(RNC(IC-LP1-1))+
     +      INT(RNT(IC))+INT(RNT(IC-LP1))+INT(RNT(IC+1))+
     +      INT(RNB(IC))+INT(RNB(IC+1))+INT(RNB(IC+LP1+1)).GT.(-6))
     +      GOTO 9
         MLEFT=LEVEL(IC-1)
         LTOP=LEVEL(IC-LP1)
         MTOP=LTOP
         LTL=LEVEL(IC-1-LP1)
         MTL=LTL
         LU1=LOLD(IC-LP1)
         MU1=LU1
         LU2=LOLD(IC)
         MU2=LU2
         LU3=LOLD(IC+1)
         MU3=LU3
         GOTO 1000
```

```
 64         IF(INT(RNC(IC+1))+INT(RNC(IC+LP1))+INT(RNC(IC+1+LP1))+
     +          INT(RNC(IC-1))+INT(RNC(IC-LP1))+INT(RNC(IC-LP1-1))+
     +          INT(RNT(IC))+INT(RNT(IC-1-LP1))+INT(RNT(IC-1))+
     +          INT(RNB(IC))+INT(RNB(IC-1-LP1))+INT(RNB(IC-LP1)).GT.(-6))
     +          GOTO 9
            MLEFT=LEVEL(IC-1)
            LTOP=LEVEL(IC-LP1)
            MTOP=LTOP
            LTL=LEVEL(IC-1-LP1)
            MTL=LTL
            LU1=LOLD(IC-1-LP1)
            MU1=LU1
            LU2=LOLD(IC-1)
            MU2=LU2
            LU3=LOLD(IC)
            MU3=LU3
            GOTO 1000
*
 1000       IF(MLEFT+MTOP+MTL+MU1+MU2+MU3.EQ.MAX6) GOTO 4
            LEFT=MLEFT.LT.MAX
            TOP=MTOP.LT.MAX
            TL=MTL.LT.MAX
            U1=MU1.LT.MAX
            U2=MU2.LT.MAX
            U3=MU3.LT.MAX
*
            IF(.NOT.TOP.OR.N(LTOP).GE.0) GOTO 12
            MS=N(LTOP)
 13         MTOP=-MS
            MS=N(MTOP)
            IF(MS.LT.0) GOTO 13
            N(LTOP)=-MTOP
*
 12         IF(.NOT.TL.OR.N(LTL).GE.0) GOTO 15
            MS=N(LTL)
 14         MTL=-MS
            MS=N(MTL)
            IF(MS.LT.0) GOTO 14
            N(LTL)=-MTL
*
 15         IF(.NOT.U1.OR.N(LU1).GE.0) GOTO 17
            MS=N(LU1)
 16         MU1=-MS
            MS=N(MU1)
            IF(MS.LT.0) GOTO 16
            N(LU1)=-MU1
```

```
*
 17         IF(.NOT.U2.OR.N(LU2).GE.0) GOTO 19
            MS=N(LU2)
 18         MU2=-MS
            MS=N(MU2)
            IF(MS.LT.0) GOTO 18
            N(LU2)=-MU2
*
 19         IF(.NOT.U3.OR.N(LU3).GE.0) GOTO 41
            MS=N(LU3)
 42         MU3=-MS
            MS=N(MU3)
            IF(MS.LT.0) GOTO 42
            N(LU3)=-MU3
*
 41         MNEW=MIN(MTOP,MTL,MLEFT,MU1,MU2,MU3)
            LEVEL(IC)=MNEW
*
            ICI=1
            IF(TOP) ICI=ICI+N(MTOP)
            IF(LEFT.AND.MTOP.NE.MLEFT) ICI=ICI+N(MLEFT)
            IF(TL.AND.MTL.NE.MLEFT.AND.MTL.NE.MTOP)
     +      ICI=ICI+N(MTL)
            IF(U1.AND.MU1.NE.MTL.AND.MU1.NE.MLEFT.AND.MU1.NE.MTOP)
     +      ICI=ICI+N(MU1)
            IF(U2.AND.MU2.NE.MU1.AND.MU2.NE.MTL.AND.MU2.NE.MLEFT
     +      .AND.MU2.NE.MTOP) ICI=ICI+N(MU2)
            IF(U3.AND.MU3.NE.MU2.AND.MU3.NE.MU1.AND.MU3.NE.MTL.AND.
     +      MU3.NE.MLEFT.AND.MU3.NE.MTOP) ICI=ICI+N(MU3)
            N(MNEW)=ICI
*
            IF(TOP.AND.MTOP.NE.MNEW) N(MTOP)=-MNEW
            IF(LEFT.AND.MLEFT.NE.MNEW) N(MLEFT)=-MNEW
            IF(TL.AND.MTL.NE.MNEW) N(MTL)=-MNEW
            IF(U1.AND.MU1.NE.MNEW) N(MU1)=-MNEW
            IF(U2.AND.MU2.NE.MNEW) N(MU2)=-MNEW
            IF(U3.AND.MU3.NE.MNEW) N(MU3)=-MNEW
            GOTO 3
 4       INDEX=INDEX+1
         LEVEL(IC)=INDEX
         N(INDEX)=1
         GOTO 3
 9       LEVEL(IC)=MAX
         IF (.NOT.RNC(IC)) COUNTP=COUNTP+1
 3    CONTINUE
*
```

```
      IF (COUP.NE.0) WRITE(*,*) 'PERCOLATION !!', COUP
      IF (INDEX.EQ.0) GOTO 35
      DO 6 IS=1, INDEX
         NIS=N(IS)
         IF(NIS.LT.0) GOTO 6
         FNIS=NIS
         CHI=CHI+FNIS*FNIS
         CHIP=CHIP+FNIS
         NSM(NIS)=NSM(NIS)+1
         IF(NIS.GT.8) GOTO 61
         NS(NIS)=NS(NIS)+1
         GOTO 6
 61      INTEG=ALOG(FNIS)*ALOG2-2
         NSUM(INTEG)=NSUM(INTEG)+1
C         IF(NIS.GE.LARGE) WRITE(*,97) NIS
 6    CONTINUE
*
C      COUNTP=COUNTP/(LP1-2)**2/(LP1-1)
      write(*,*)
      write(*,*) 'COUNTP= ', COUNTP, COUNTP/(LP1-2)**2/(LP1-1)
      CLUSUM=0
      DO 400 I=1, MAXS
      IF (NSM(I).EQ.0) GOTO 400
      CLUSUM=CLUSUM+NSM(I)
      write(8,95) I, NSM(I)
 400  CONTINUE
      write(*,*) 'Nfin = ',  CHIP/CLUSUM, CHIP, CHIP/NL**3
*
 35   WRITE(*,96) NS
 95   FORMAT(2X, I8, I12)
 96   FORMAT(" NS:", I9, 7I8)
 97   FORMAT(" CLUSTER OF SIZE ", I12)
 93   FORMAT(" BINS:",4(/,8I9))
 2    FORMAT(F15.8,3I12,F20.4)
*
      WRITE(*,93) NSUM
      CHI=(CHI/L)/L/L
      WRITE(*,2) P,L,INDEX,IREC,CHI
      PI=2.0**(35.0)
      ISUM=0
      DO 905 INDEX=1, 32
         INTEG=33-INDEX
         ISUM=ISUM+NSUM(INTEG)
         CHI=(ISUM*(PI)**TAUM1/L)/L/L
         IF(ISUM.GT.0) WRITE(*,2) CHI,ISUM,INT(PI), INTEG
 905     PI=PI/2.0
```

```
      DO 906 INDEX=1, 7
         NIS=8-INDEX
         ISUM=ISUM+NS(NIS)
         CHI=(ISUM*REAL(NIS)**TAUM1/L)/L/L
906      WRITE(*,2) CHI,ISUM,NIS
         STOP
         END
```

REFERENCES

[1] R. Kirchheim, *Electrochim. Acta*, **32**, p. 1619 (1987).

[2] K. J. Vetter and F. Gorn, *Electrochim. Acta*, **18**, p. 321 (1973).

[3] D. D. Pollock, "Electrical Conduction in Solids: An Introduction," p. 241, American Society for Metals, Metals Park, OH (1985).

[4] H. Kaesche, in "Passivity of Metals," R. P. Frankenthal and J. Kruger, Editors, p. 935, The Electrochemical Society, Inc., Princeton, NJ (1978).

[5] Jose R. Galvele, in "Treatise on Materials Science and Technology," J. C. Scully, Editor, p. 1, Academic Press Inc., New York, NJ (1983).

[6] A. Despič and V. Parkhutik, in "Modern Aspects of Electrochemistry," J. O'M. Bockris, R. E. White, and B. E. Conway, Editors, p. 401, Plenum Press, New York, NJ (1989).

[7] R. H. Broadbent, *Electrochem. Technol.*, **6**, p. 163 (1968).

[8] G. E. Thompson and G. C. Wood, *Corros. Sci.*, **18**, p. 721 (1978).

[9] C. K. Dyer and R. S. Alwitt, *J. Electrochem. Soc.*, **128**, p. 300 (1981).

[10] C.-F. Lin and K. R. Hebert, *J. Electrochem. Soc.*, **137**, p. 3723 (1990).

[11] C.-F. Lin and K. R. Hebert, *J. Electrochem. Soc.*, **141**, p. 104 (1994).

[12] R. S. Alwitt, H. Uchi, T. R. Beck, and R. C. Alkire, *J. Electrochem. Soc.*, **131**, p. 13 (1984).

[13] N. F. Jackson, *Electrocomp. Sci. and Tech.*, **2**, p. 33 (1975).

[14] Z. Szklarska-Smialowska, "Pitting Corrosion of Metals," p. 8, National Association of Corrosion Engineers, Houston, TX (1986).

[15] Z. Szklarska-Smialowska, "Pitting Corrosion of Metals," p. 377, National Association of Corrosion Engineers, Houston, TX (1986).

[16] L. Young, "Anodic Oxide Films,"p. 193, Academic Press, New York, NY (1961).

[17] C.-F. Lin, M. D. Porter and K. R. Hebert, *J. Electrochem. Soc.*, **141**, p. 96 (1994).

[18] C.-F. Lin, Ph.D. Thesis, Iowa State University, Ames, IA (1992).

[19] H.-H. Strehblow, *Werkst. Korros.*, **35**, p. 437 (1984).

[20] H. Böhni, in "Corrosion Mechanisms," F. Mansfeld, Editor, p. 285, Marcel Dekker, Inc., New York, NY (1987).

[21] T. P. Hoar and W. R. Jacob, *Nature*, **216**, p. 1299 (1967).

[22] J. R. Gavele, in "Passivity of Metals," R. P. Frankenthal and J. Kruger, Editors, p. 310, The Electrochemical Society, Inc., Princeton, NJ (1978).

[23] T. P. Hoar, D. C. Mears and G. P. Rothwell, *Corros. Sci.*, **5**, p. 279 (1965).

[24] J. Painot and J. Augustynski, *Electrochem. Acta*, **20**, p. 747 (1975).

[25] G. C. Wood, W. H. Sutton, J. A. Richardson, T. K. N. Riley and A. G. Malherbe in "Localized Corrosion," R. W. Staehle, B. F. Brown, J. Kruger and A. Agrawal, Editors, p. 526, National Association of Corrosion Engineers, Houston, TX (1971).

[26] G. Okamoto, K. Tachibana, S. Nishiyama and T. Sugita in "Passivity and its Breakdown on Iron and Iron Base Alloys," R. W. Stachle and H. Okada, Editors, p. 106, National Association of Corrosion Engineers, Houston, TX (1976).

[27] N. Sato, *Electrochim. Acta*, **16**, p. 1683 (1971).

[28] C. Y. Chao, L. F. Lin and D. D. Macdonald, *J. Electrochem. Soc.*, **128**, p. 1187 (1981).

[29] L. F. Lin, C. Y. Chao and D. D. Macdonald, *J. Electrochem. Soc.*, **128**, p. 1194 (1981).

[30] B. J. Wiersma and K. R. Hebert, *J. Electrochem. Soc.*, **138**, p. 48 (1991).

[31] John Newman, "Electrochemical Systems," p. 378, Prentice-Hall Inc., Englewood Cliffs, NJ (1991).

[32] K. R. Hebert, unpublished work.

[33] D. D. Wagman *et al.*, *J. of Phys. and Chem. Ref. Data*, Vol. 11, Supple. No. 2, p. 2-30 (1982).

[34] I. Rousar, K. Micka, and A. Kimla, "Electrochemical Engineering," v. 2, p. 123, Elsevier Sci. Pub. Co., New York, NY (1986).

[35] John Newman, *op. cit.*, p. 454.

[36] F. P. Incropera and D. P. DeWitt, "Fundamentals of Heat and Mass Transfer," 3rd ed., p. 237, John Wiley & Sons, New York (1990).

[37] W. Wilhelmsen and T. Hurlen, *Electrochim. Acta.*, **32**, p. 95 (1987).

[38] J. Bessone, C. Mayer, K. Jüttner and W. J. Lorenz, *Electrochim Acta.*, **28**, p. 171 (1983).

[39] K. Videm, "The Electrochemistry of Uniform Corrosion and Pitting of Aluminum," Kjeller Report, p. 17, p. 24, Institute for Atomenergi, Kjeller, Norway (1974).

[40] D. J. Dzimitrowicz, J. B. Goodenough, and P. J. Wiseman, *Mat. Res. Bull.*, **17**, p. 971 (1982).

[41] L. Young, *op. cit.*, p. 220.

[42] W. J. Bernard and J. W. Cook, *J. Electrochem. Soc.*, **106**, p. 643 (1959).

[43] A. Charlesby, *Pro. Phys. Soc.*, B., **66**, p. 317 (1953).

[44] T. Våland and K. E. Heusler, *J. Electroanal. Chem.*, **149**, p.71 (1983).

[45] M. Pourbaix, "Atlas of Electrochemical Equilibria in Aqueous Solutions," p. 168, Pergamon Press, Oxford (1966).

[46] Bruce A. Finlayson, "Nonlinear Analysis in Chemical Engineering," McGraw-Hill Inc., p. 73, p.191 (1980).

[47] A. W. Hassel and M. M. Lohrengel, *Electrochim. Acta*, **40**, p.433 (1995).

[48] H. Takahashi, K. Kasahara, K. Fujiwara and M. Seo, *Corros. Sci.*, **36**, p. 677 (1994).

[49] H. Takahashi, K. Fujiwara and M. Seo, *Corros. Sci.*, **36**, p. 689 (1994).

[50] Y. G. Bérubé and P. L. De Bruyn, *J. Colloid Interface Sci.*, **28**, p.92 (1968).

[51] G. E. Thompson and G. C. Wood, in *Treatise on Materials Science and Technology*, Vol. 23, J. C. Scully, Editor, p. 273, Academic Press, Inc., New York (1983).

[52] K. Shimizu, K. Kobayashi, G. E. Thompson and G. C. Wood, *Phil. Mag. A.*, **66**, p. 643 (1992).

[53] L. Young, *op. cit.*, p. 272.

[54] L. Young, *op. cit.*, p. 212.

[55] L. Young, *op. cit.*, p. 188.

[56] L. Young, *op. cit.*, p. 93.

[57] A. T. Fromhold, Jr., *J. Electrochem. Soc.*, **127**, p. 411 (1980).

[58] J. Frankel, *Z. Phys.*, **35**, p. 652 (1926).

[59] K. J. Vetter, "Electrochemical Kinetics. Theoretical and Experimental Aspects," p. 759, Academic Press Inc., New York, NY (1967).

[60] M. J. Dignam, "Oxides and Oxide Films," Vol. 1, p. 190, New York, M. Dekker (1972).

[61] M. J. Dignam, "Oxides and Oxide Films," Vol. 1, p. 236, New York, M. Dekker (1972).

[62] W. H. Zachariasen, *J. Am. Chem. Soc.*, **54**, p. 3841 (1931).

[63] F. A. Kröger, "The Chemistry of Imperfect Crystals," chap 7, North-Holland Publishing Co.-Amsterdam (1964).

[64] F. A. Kröger, "The Chemistry of Imperfect Crystals," chap 14. North-Holland Publishing Co.-Amsterdam (1974).

[65] G. Amsel and D. Samuel, *J. Phys. Chem. Solids*, **23**, p. 1707 (1962).

[66] N. F. Mott, *Philosophical Magazine B*, **55**, p. 117 (1987).

[67] J. P. S. Pringle, *J. Electrochem. Soc.*, **120**, p. 398 (1973).

[68] J. P. S. Pringle, *J. Electrochem. Soc.*, **120**, p. 1391 (1973).

[69] F. Brown and W. D. Mackintosh, *J. Electrochem. Soc.*, **8**, p. 1096 (1973).

[70] L. Young, *Trans. Faraday Soc.*, **50**, p. 153 (1954).

[71] L. Young, *Trans. Faraday Soc.*, **52**, p. 502 (1956).

[72] J. A. Davies, J. P. Pringle, R. L. Graham, and F. Brown, *J. Electrochem. Soc.*, **109**, p. 999 (1962).

[73] J. A. Davies, B. Domeij, J. P. S. Pringle, and F. Brown, *J. Electrochem. Soc.*, **112**, p. 675 (1965).

[74] J. A. Davies and B. Domeij, *J. Electrochem. Soc.*, **110**, p. 849 (1963).

[75] W. D. Mackintosh and H. H. Plattner, *J. Electrochem. Soc.*, **124**, p. 396 (1977).

[76] W. D. Mackintosh and H. H. Plattner, *J. Electrochem. Soc.*, **123**, p. 523 (1976).

[77] J. L. Whitten, *J. Electrochem. Soc.*, **115**, p. 58 (1968).

[78] K. Shimizu, G. E. Thompson, G. C. Wood and Y. Xu, *Thin Solid Films*, **88**, p. 255 (1982).

[79] K. Shimizu and K. Kobayashi, *Phil. Mag. B.*, **64**, no. 3, p. 345 (1991).

[80] C. R. A. Catlow and R. James, *Phys. Rev. B*, **25**, p. 1006 (1982).

[81] M. H. Cohen and G. S. Grest, *Phys. Rev. B*, **20**, no. 3, p. 1077 (1979).

[82] F. Scordari, "Fundamentals of Crystallography," editor C. Giacovazzo, p. 420, Oxford University Press, Oxford (1992).

[83] A. J. Schrijner and A. Middelhoek, *J. Electrochem. Soc.*, **111**, p. 1167 (1964).

[84] R. W. Grimes and C. R. A. Catlow, *J. Am. Ceram. Soc.*, **73**, p. 3251 (1990).

[85] G. Arfken, "Mathematical Methods for Physicists," p. 656, Academic Press, Inc, San Diego, CA (1985).

[86] N. Cabrera and N. F. Mott, *Rep. Prog. Phys.*, **12**, p. 163 (1948-1949).

[87] D. Turnbull and M. B. Cohen, *J. Chem. Phys.*, **34**, no. 5, p. 120 (1961).

[88] R. Manaila, A, Dévényi and E. Candet, *Thin Solid Films*, **116**, p. 289 (1984).

[89] K. Binder and D. Stauffer, in "Application of Monte Carlo Method in Statistical Physics," editor K. Binder, p. 1, Springer-Verlag, Berlin New York (1984).

[90] D. Perry and S. Phillips, editors, "Handbook of Inorganic Compounds," p. 10, CRC Press, Inc., Boca Raton, FL (1995).

ACKNOWLEDGMENTS

I would like to thank Professor Kurt Hebert for giving me the opportunity to perform research under his guidance. During the years of my graduate study, his has helped me greatly through this work.

I am also very grateful to my committee members, Professor L. Doraiswamy, Professor Glenn Schrader, Professor Kai-Ming Ho, Professor Steve Martin and Professor Marc Porter for the time they spent reviewing this manuscript and for their suggestions.

The assistance from my research colleagues, Dr. Ching-Feng Lin, Dr. Yongsug Tak, and Isamu Obi for my experimental work will always be remembered.

Finally, many thanks are due to my parents, my husband, and my two brothers for their encouragement and support.

IMAGE EVALUATION
TEST TARGET (QA-3)

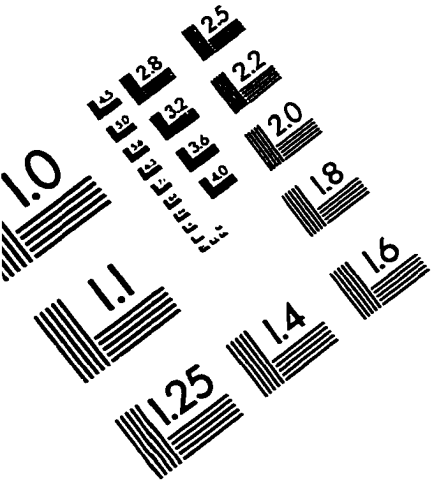

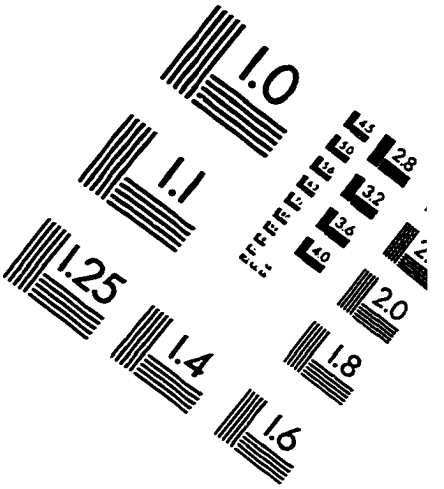

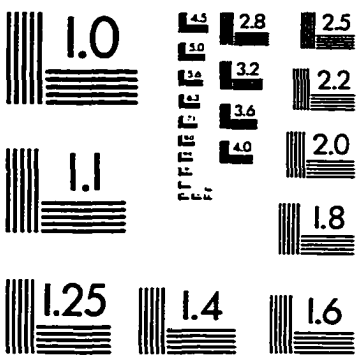

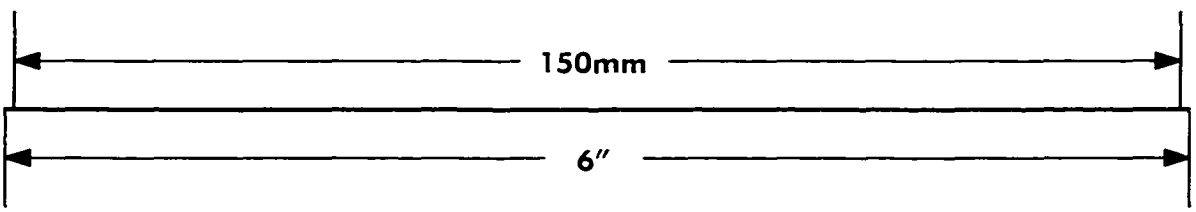

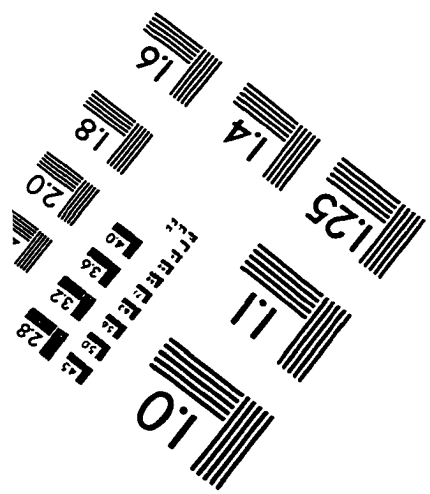

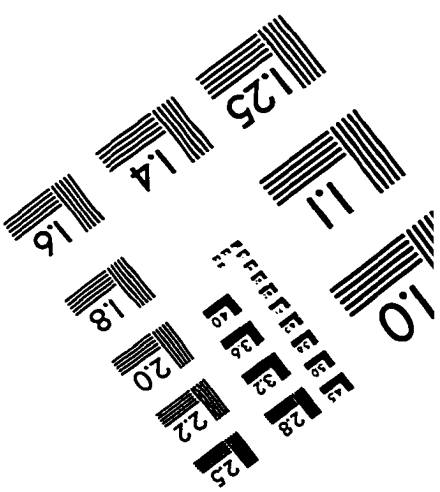

APPLIED IMAGE, Inc
1653 East Main Street
Rochester, NY 14609 USA
Phone: 716/482-0300
Fax: 716/288-5989